A DYNAMIC MODEL FOR ALA-PDT OF NORMAL HUMAN SKIN

"Jade must be chiseled before it can be considered a gem."

– Chinese proverb

INSIGHTS INTO PHOTODYNAMIC THERAPY AND ITS DOSIMETRY USING A DYNAMIC MODEL FOR ALA-PDT OF NORMAL HUMAN SKIN

BY

BAOCHANG LIU, M.Sc., B.Sc.

A THESIS

SUBMITTED TO THE DEPARTMENT OF

MEDICAL PHYSICS & APPLIED RADIATION SCIENCES

AND THE SCHOOL OF GRADUATE STUDIES

OF MCMASTER UNIVERSITY

IN PARTIAL FULFILMENT OF THE REQUIREMENTS

FOR THE DEGREE OF

DOCTOR OF PHILOSOPHY

DOCTOR OF PHILOSOPHY (2012) McMaster University

(Medical Physics & Applied Radiation Sciences) Hamilton, Ontario, Canada

TITLE: **INSIGHTS INTO PHOTODYNAMIC THERAPY AND ITS DOSIMETRY USING A DYNAMIC MODEL FOR ALA-PDT OF NORMAL HUMAN SKIN**

AUTHOR: Baochang Liu

M.Sc. (Physics), Brock University, Canada

B.Sc. (Honours, Physics), Dalian University of Technology, P. R. China

SUPERVISOR: Michael S. Patterson, Ph.D.

NUMBER OF PAGES: xiv, 142

Abstract

Photodynamic therapy (PDT) is a rapidly developing clinical treatment modality involving a light-activatable photosensitizer, tissue oxygen and light of an appropriate wavelength to generate cytotoxic reactive molecular species - primarily singlet oxygen ($^1O_2$). Singlet oxygen readily reacts with surrounding biomolecules leading to different biological effects and subsequent therapeutic outcomes. Over the last decades, many standard PDT treatments have been approved worldwide to treat different medical conditions ranging from a variety of cancer conditions to age-related macular degeneration (AMD). Meanwhile, many active clinical trials and pre-clinical studies are underway for other clinical indications. The therapeutic outcomes of PDT are difficult to predict reliably even with many years of research. The fundamental cause for this is the inherent complexity of PDT mechanisms. As PDT involves three main components, the outcomes of PDT are determined by the combination of all components. Each component varies temporally and spatially during PDT, and the variations are mutually dependent on each other. Moreover, components such as the photosensitizer can have great variations in their initial distribution among patients even before PDT treatment. Given this, no well accepted standard PDT dose metric method has been recognized in clinics, although different approaches including explicit, implicit and direct dosimetry have been studied. To tackle the inherently complicated PDT mechanism in order to provide insights into PDT and PDT dosimetry, a theoretical one-dimensional model for aminolevulinic acid (ALA) induced protoporphyrin IX (PpIX)-PDT of human skin was developed and is presented in this thesis. The model incorporates major photophysical and photochemical reactions in PDT, and calculated temporal and spatial distributions of PDT components as well as the detectable emission signals including both sensitizer fluorescence and singlet oxygen luminescence (SOL) using typical clinical conditions. Since singlet oxygen is considered to cause PDT outcomes, the correlations of different PDT dose metrics to average reacted $^1O_2$ 'dose' and 'dose' at different depths were examined and compared for a wide range of varied treatment conditions. The dose metrics included absolute fluorescence bleaching metric (AFBM), fractional fluorescence bleaching metric (FFBM) and cumulative singlet oxygen luminescence (CSOL), and the varied treatment conditions took into account different treatment irradiances and wavelengths, varied initial

sensitizer concentration and distribution, and a wide range of optical properties of tissue. These investigations and comparisons provide information about the complicated dynamic process of PDT such as the induction of tissue hypoxia, photosensitizer photobleaching and possible PDT-induced vascular responses. It was also found that the CSOL is the most robust and could serve as a "gold standard" for the testing of other techniques. In addition to these theoretical studies, recent progress on the assessment of a novel, more efficient superconducting nanowire single photon detector (SNSPD) for singlet oxygen luminescence detection will be introduced and the current photomultiplier tubes (PMT) system will be briefly described as well. The author participated in the experimental assessments of the SNSPD and analyzed the results shown in this thesis.

Acknowledgements

First and foremost, I would like to express my greatest gratitude to my supervisor, Dr. Michael Patterson, for all of his continued support, guidance and encouragement and exceptional mentorship throughout my entire Ph.D studies. His understanding of and insight into science have truly inspired me to continue my career in the biomedical field. His endless ideas and meticulous editing of all my publications and this thesis have made my studies successful, and most importantly, all of these have taught me how to conduct and evaluate scientific work as a scholar, which will benefit me for the rest of my life.

I would like to extend my thanks to my supervisory committee members Dr. Tom Farrell and Dr. Joe Hayward for their guidance and support. Dr. Farrell has been a tremendous resource for the theoretical development of the model.

I would like to express my heartfelt thanks to Dr. Brian Wilson for his generous support of my experimental work in his lab and at Heriot-Watt University as a visiting scholar. His scientific guidance has greatly extended my knowledge of experimental research. I also thank Dr. Mark Jarvi for many helpful discussions and suggestions. I thank Dr. Robert Hadfield and all his group members at Heriot-Watt University for the collaboration on the singlet oxygen luminescence experiments.

I am grateful to the technicians of the electronics and machine shops at the Juravinski Cancer Centre. It has been my pleasure to work with a group of intelligent people, Dr. Kevin Diamond, Dr. Julius Pekar, Mark Weston, Diana Glennie and all other members in our biomedical optics group. I thank them for sharing knowledge, helpful discussions and making my life memorable at the JCC. Andrew Davis should also be acknowledged for helping me with my studies and life in Canada.

I would like to acknowledge the administration staff, Pauline Hiltz, Fiona Ahlang and Wendy Malarek, for their supportive work.

I want to express my deepest thanks to my mother for her unconditional love and support during the past ten years of my studies in Canada. This achievement would not have been possible without her continued encouragement. Last but not least, I would like to thank my wife and lovely daughter for their support, inspiration and love.

for my parents

Contents

List of Figures

List of Tables

Symbols and Acronyms

C_{r}	adjoint scaling factor; 29
Δs	step size; 28
$\eta_{\mathrm{absorption}}$	absorption efficiency; 127
η_{coupling}	coupling efficiency; 127
η_{de}	detection efficiency; 127
η_{qe}	quantum efficiency; 125
$\eta_{\mathrm{registering}}$	registering probability; 127
η_{sde}	system detection efficiency; 126
μ_s'	reduced scattering coefficient; 28
μ_a	absorption coefficient; 28
S_0	ground-state sensitizer; 3, 6, 124
S_1	singlet excited-state sensitizer; 3, 124
$^1\mathrm{O}_2$	singlet oxygen; iii, 3–5, 7, 26, 124
$^3\mathrm{O}_2$	ground-state oxygen; 4, 27, 124
τ_{D}	singlet oxygen lifetime; 124
AFBM	absolute fluorescence bleaching metric; iii, 18, 74
AK	actinic keratoses; 26
ALA	aminolevulinic acid; iii, 5, 26
AMD	age-related macular degeneration; iii
BCC	basal cell carcinoma; 26
BSA	Bovine serum albumin; 8, 135, 140
CoA	succinyl coenzyme A; 5
CSOL	cumulative singlet oxygen luminescence; iii, 8, 18, 74
F	fluorescence; 4

FD	fluorescence diagnosis; 5
FFBM	fractional fluorescence bleaching metric; iii, 18, 74
GUI	graphical user interface; 10, 15, 27, 44
IC	internal conversion; 3
ISC	inter-system crossing; 4
MC	Monte Carlo; 10, 12, 25, 26, 28, 44
MLu	motexafin lutetium; 6
mTHPC	meta-tetra(hydroxyphenyl)chlorine; 7
NaN_3	sodium azide; 129, 131
NbN	niobium nitride; 125
NR	non-radiative deactivation; 4
P	phosphorescence; 4
PDT	photodynamic therapy; iii, 1, 26, 138
PMT	photomultiplier tubes; iv, 8, 123, 125, 139
PpIX	protoporphyrin IX; iii, 5, 26
PS	photosensitizer; 3
RB	Rose Bengal; 129, 131
sBCC	superficial basal cell carcinoma; 11
SC	stratum corneum; 10
SNR	signal to noise ratio; 8
SNSPD	superconducting nanowire single photon detector; iv, 9, 18, 123, 140
SOL	singlet oxygen luminescence; iii, 7, 8, 123
SOLD	singlet oxygen luminescence dosimetry; 7, 18, 26, 27, 123
T_1	triplet excited-state sensitizer; 4, 124

Chapter 1

Introduction

This thesis is based on a series of studies on photodynamic therapy (PDT) and PDT dosimetry using a one-dimensional dynamic model of ALA-PDT of human skin. The following sections in this chapter will briefly introduce some fundamental information about PDT and PDT dosimetry. Some basic knowledge about the model and the motivation and organization of the thesis are also included to help readers in understanding these studies and the entire thesis.

1.1 Photodynamic therapy

Photodynamic therapy (PDT) has emerged as a treatment modality for curative or palliative treatment of malignant and non-malignant diseases. Photodynamic action was observed over a century ago by Oscar Raab, who found the lethal damages of acridine to paramecia after exposure of light (Moan and Peng 2003). Several decades later, PDT was introduced into modern medicine by Thomas Dougherty and colleagues at Rosewell Park Cancer Center in the late 1970s (Dougherty *et al.* 1978, 1979). Since then, PDT has been under investigation in numerous clinical trials worldwide for various types of cancers and other diseases. To date, PDT has been approved to treat a number of conditions ranging from the treatment of cancer to non-oncological disease such as age related macular degeneration. Table 1.1 lists the currently approved standard PDT treatments worldwide.

Table 1.1: Approved photosensitizers and indications. (O'Connor *et al.* 2009; Dolmans *et al.* 2003; Brown *et al.* 2004)

Cancer			
Photosensitizer	**Absorption (nm)**	**Indication**	**Approval Countries**
Photofrin (HPD)	630	Cervical cancer	Japan
Photofrin (HPD)	630	Papillary bladder cancer	Canada, Japan, USA
Photofrin (HPD)	630	Gastric Cancer	Japan
Photofrin (HPD)	630	Microinvasive endobronchial lung cancer	EU, Japan, USA
Photofrin (HPD)	630	Obstructive lung cancer	Canada, Japan, USA
Photofrin (HPD)	630	Obstructive esophageal cancer	Canada, Japan, USA
Metvix (methyl ALA)	635	Basal cell carcinoma	EU
Foscan (mTHPC)	652	Head & Neck cancer	EU
Talaporfin sodium (NPe6)	664	Early lung cancer	Japan
Non-Cancer			
Photosensitizer	**Absorption (nm)**	**Indication**	**Approval Countries**
Levulan (5-ALA)	635	Actinic keratoses	Canada, EU, USA
Metvix(methyl ALA)	635	Actinic keratoses	Canada, EU, USA
Verteporfin (BPD-MA)	690	Age-related macular degeneration	Canada, EU, Japan, USA
Photofrin (HPD)	630	Cervical dysplasia	Japan
Photofrin (HPD)	630	Barrett's esophagus	EU, USA

HPD: hematoporphyrin derivative, ALA: aminolevulinic acid, mTHPC: meta-tetra(hydroxyphenyl)chlorine, NPe6: mono-L-aspartyl chlorin e6, BPD-MA: benzoporphyrin derivative monoacid. EU: European Union.

PDT involves three main components: a light-activated agent called a photosensitizer (PS), tissue oxygen, and an excitation light source of an appropriate wavelength with sufficient output power. In PDT, the photosensitizer is topically or systemically administered at first, and then preferentially accumulates in target tissue within a certain time. This time can be different for different photosensitizers. With absorption of excitation light, reactive oxygen, known as singlet oxygen ($^1O_2$), is generated via a series of photophysical and photochemical reactions. Singlet oxygen readily reacts with surrounding biomolecules, resulting in biological effects such as cell death and, consequently, therapeutic outcomes such as destruction of vasculature or tumor regression. The details of the basic PDT mechanism are illustrated by the Jablonski diagram in figure 1.1.

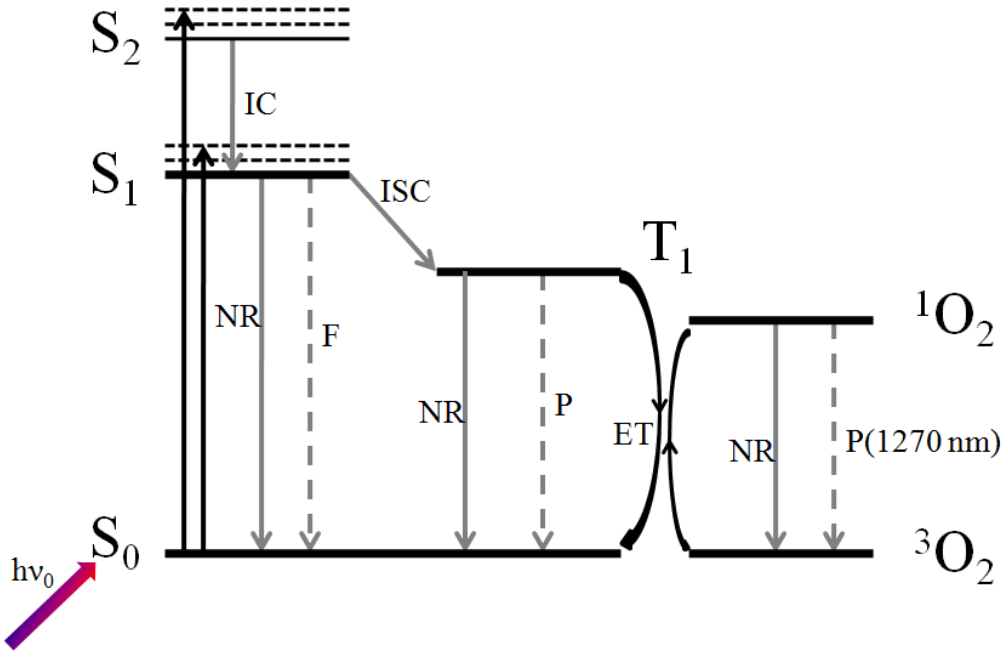

Figure 1.1: Jablonski diagram for photodynamic therapy. S_0: PS ground state, S_1: the first excited singlet state, S_2: the second excited state, T_1: PS triplet state, $^1O_2$: singlet state oxygen, $^3O_2$: ground-state oxygen, NR: non-radiative deactivation, ISC: inter-system crossing, IC: internal conversion, ET: energy transfer, F: fluorescence, P: phosphorescence. The dash horizontal lines are the vibrational states.

First, after absorbing incident photons of an appropriate energy, ground-state sensitizer (S_0) is excited and becomes singlet excited-state sensitizer (S_1) possibly via other higher energy or vibrational states. Molecules at those higher energy or vibrational states will quickly return to the first singlet state via internal conversion

(IC). The S_1 may decay back to the ground state via non-radiative deactivation (NR), or via emitting fluorescence (F) photons. For efficient PS, S_1 becomes triplet excited-state sensitizer (T_1) via an inter-system crossing (ISC) process during which the spin of the electron is rearranged so that it is aligned with the spin of the electron in the ground state. Given that, the decay of the molecule from T_1 is prevented, resulting in longer triplet-state lifetime. Some T_1 will still be able to become S_0 via phosphorescence (P) at low probability, but most T_1 will transfer its energy to ground-state oxygen ($^3O_2$), producing singlet oxygen ($^1O_2$). The $^1O_2$ can then rapidly react with surrounding biomolecular targets leading to biological effects. A small fraction of the $^1O_2$ will decay back to the ground state via emission of phosphorescence (P) at wavelength of 1270 nm. The major transitions and photochemical reactions described above are summarized in equations (1.1a) to (1.1f).

$$S_0 + h\nu_0 \rightarrow S_1 \tag{1.1a}$$

$$S_1 \xrightarrow{F} S_0 + h\nu_F \tag{1.1b}$$

$$S_1 \xrightarrow{ISC} T_1 \tag{1.1c}$$

$$T_1 \xrightarrow{P} S_0 + h\nu_P \tag{1.1d}$$

$$T_1 +^3 O_2 \xrightarrow{ET} S_0 +^1 O_2 \tag{1.1e}$$

$$^1O_2 \xrightarrow{P} {}^3O_2 + h\nu_{1270} \tag{1.1f}$$

Compared to other treatment modalities such as radiotherapy and chemotherapy, PDT has several advantages. First, PDT treatment can be non-invasively or minimally invasively localized in targets. This targeting objective can be achieved via the dual selectivity of PDT: the preferential localization of PS in the targeted volume and the delivery of incident light directly to the target. Second, PDT is considered to be minimally toxic to the surrounding normal tissue due to the dual selectivity and usually produces good healing responses in normal tissue, both of which permit retreatments. Third, an ideal photosensitizer itself is not toxic, and it can be reliably activated by an appropriate wavelength of light and metabolized within a reasonable length of time without creating any toxic products. On the other hand, PDT also has some disadvantages. Even though an array of photosensitizers is available to choose for different PDT treatment, most of them have optimal absorption of light in the visible wavelength range (400 – 700 nm), and some in the near-infrared range (700 – 850 nm). The light penetration in these ranges with current standard laser and low power LED technologies is limited, which restricts the treated depth or target volume. Additionally, the production of singlet oxygen during PDT depends on the availability of molecular tissue oxygen. Oxygen in the target can be consumed rapidly by PDT and permanently lost via the reaction of singlet oxygen with sensitizer. This leads to

the formation of hypoxia in that target, which consequently limits the production of singlet oxygen and PDT outcomes. Moreover, patients administered photosensitizer for PDT treatments, especially for dermatological treatments, often have increased skin photosensitivity, which may require them to avoid non-treatment light exposure such as sun light before and after PDT until most sensitizer has been metabolized.

Aminolevulinic acid (ALA) induced protoporphyrin IX (PpIX) PDT utilizes the pro-drug ALA to endogenously produce photosensitizer PpIX followed by the delivery of treatment excitation light. In the heme biosynthetic pathway, ALA is formed in the mitochondria from the amino acid glycine and succinyl coenzyme A (CoA). A series of intermediate enzyme steps outside the mitochondria produce coproporphyrinogen III from ALA, which then re-enters mitochondria and eventually yields PpIX. Under the action of ferrochelatase, the combination of PpIX and iron produces heme. When exogenous ALA is given to cells, PpIX can accumulate excessively due to the limited capacity of ferrochelatase and so it remains available as photosensitizer. Therefore, since the early work by Kennedy *et al.* (1990), the pure or derivative pro-drug ALA has been used to enhance the endogenous generation of PpIX, which is commonly used for fluorescence diagnosis (FD) and photodynamic therapy. In ALA-PDT, ALA is normally systemically or topically administered to treat pre-malignant and malignant conditions at various sites. The primary indications for topical ALA-PDT are dermatological due to easy access to light. For instance, Levulan® was approved for treatment of actinic keratoses and small basal cell carcinoma as listed in table 1.1.

1.2 Photodynamic therapy dosimetry

In the well developed ionizing radiation therapy, dose is defined as the energy absorbed per unit mass of tissue. The therapeutic biological response is well correlated with dose in clinical radiotherapy treatment. The correlation can be described using a sigmoidal function. In contrast, there is no well defined term describing PDT dose. Singlet oxygen ($^1O_2$) has been widely accepted as the main cytotoxic agent causing biological outcomes in PDT since it was identified by Weishaupt *et al* in 1976 (Weishaupt *et al.* 1976). Direct or indirect measure of $^1O_2$ concentration has been one goal of PDT dosimetry studies (Niedre *et al.* 2002). The PDT response can be classified as: direct cell kill, vascular response and immune response. The correlation of the response to the PDT 'dose' is not yet clear or well understood. Currently, the common dosimetry protocol in clinical PDT is to monitor the photosensitizer dose (mg kg^{-1}) administered to the patient and the treatment light exposure (J cm^{-2}). However, this may be inadequate as the standard PDT dose metric to predict PDT outcomes. The challenges are mainly due to the inherent complexity of the basic PDT mechanism as described in section 1.1, and also due to the temporal and spatial variations of the three PDT components during treatment.

The details of PDT dosimetry will be further discussed in Chapter 4. In general, PDT dosimetry can be classified into three approaches: explicit dosimetry, implicit dosimetry and direct dosimetry (Wilson and Patterson 2008). A brief introduction to each method is discussed below.

1.2.1 Explicit dosimetry

Explicit dosimetry aims to measure all three main components of PDT (light, photosensitizer and oxygen) and the measurements should ideally be performed throughout the entire treatment. Singlet oxygen concentration during treatment is then updated using the distributions of the components in real-time and knowledge of the photochemical reactions. However, individual components are not easy to measure continuously because they can vary dramatically during PDT. Finlay *et al.* (2006) used interstitial fluorescence spectroscopy to measure the sensitizer motexafin lutetium (MLu) concentration in the prostates of five patients, and found significantly heterogeneous concentration within and among these patients. The variation of the components also mutually depends on each other. For instance, Tyrrell *et al.* (2011) observe that the loss of sensitizer PpIX is positively correlated to the reduction in oxygen saturation during early dermatological MAL-PDT. Moreover, PDT therapeutic outcomes are caused by singlet oxygen determined by the combinations of all three components. Hence, prediction of PDT outcomes through monitoring individual or all parameters is not easy and may not be sufficient.

1.2.2 Implicit dosimetry

Implicit dosimetry involves measurement of a surrogate for singlet oxygen concentration. After $^1O_2$ is generated, it can react with ground-state sensitizer (S_0) resulting in both the loss of S_0 and production of photoproduct. The loss of photosensitizer via this reaction is called photobleaching, which may be monitored via the reduction of sensitizer fluorescence. With this hypothesis, the instantaneous $^1O_2$ concentration can be calculated via the loss of S_0 as shown in equation (1.2), and the total PDT 'dose' over time T will be the time integration of equation (1.2), as written by equation (1.3), where τ_D (s) is singlet oxygen lifetime, δ introduced by Dysart *et al.* (2005) accounts for the reaction of singlet oxygen with the photosensitizer molecule that generated it, and k_{os} ($M^{-1}s^{-1}$) is the bimolecular rate constant for reaction of

$^1O_2$ with S_0. The detail of the derivation can be found in Dysart *et al.* (2005).

$$\left[^1O_2\right] = -\frac{1}{k_{os}\left([S_0]+\delta\right)}\frac{d\,[S_0]}{dt}\,, \tag{1.2}$$

$$\begin{aligned}\text{Dose} &= \frac{1}{\tau_D}\int_0^T \left[^1O_2\right](t)dt \\ &= \frac{1}{\tau_D k_{os}}\ln\left(\frac{([S_0]_{t=0}+\delta)}{([S_0]_{t=T}+\delta)}\right)\,. \end{aligned} \tag{1.3}$$

This method is relatively simple and practical to be translated into clinics, and it has been extensively investigated in pre-clinical and clinical studies (Dysart *et al.* 2005; Dysart and Patterson 2006; Cottrell *et al.* 2008). However, the results are controversial. For example, Dysart *et al.* (2005) found that for the photosensitizer meta-tetra(hydroxyphenyl)chlorine (mTHPC), photobleaching is well correlated to treatment outcomes and can predict $^1O_2$ dose under certain restricted conditions. However, a study on ALA-induced PpIX PDT showed that this method cannot estimate $^1O_2$ dose due to other non-$^1O_2$ mediated PS photobleaching under hypoxic conditions (Dysart and Patterson 2006). Finlay *et al.* (2004) also found the loss of PS Photofrin can be via reaction with the sensitizer triplet state. Moreover, the loss of PS fluorescence signals may be explained by the rearrangement of the distribution of sensitizer during PDT (Robinson *et al.* 1998). In contrast to these results, other studies have shown that PpIX photobleaching observed in clinical studies could be explained by only $^1O_2$-mediated photobleaching (Cottrell *et al.* 2008; Wang *et al.* 2009). Therefore, PS fluorescence photobleaching approach needs to be fully characterized for a specific sensitizer before being implemented as a routine dose metric in clinical PDT.

The other method relies on the principle that the photoproduct in PDT is produced only by $^1O_2$-mediated bleaching, so that $^1O_2$ dose can be reliably estimated via the concentration of the photoproduct. The concentration may be indirectly obtained from measuring photoproduct fluorescence. Some success has been achieved in cell and animal studies (Dysart and Patterson 2006; Zeng *et al.* 2002).

1.2.3 Direct dosimetry

Given that $^1O_2$ is the ultimate product of the complicated PDT mechanism which causes biological effects and therapeutic outcomes, direct monitoring of its production during PDT may be expected to be ideal as a reliable dose metric. The monitoring can be attempted via the detection of the very weak near-infrared singlet oxygen luminescence (SOL) emission at 1270 nm. This is the basis for direct dosimetry also known as singlet oxygen luminescence dosimetry (SOLD).

In general, SOL detection has been challenging because: first, emission probability of SOL is very low (about 10^{-8} for one generated singlet oxygen molecule), which can be attributed to the short lifetime of $^1O_2$ - the typical value in the aqueous solution is about 3 μs, and even much shorter in biological environments (sub-microsecond); second, most photomultiplier tubes (PMT) photodetectors have very low quantum efficiency to detect this highly reactive oxygen species from biological environments and *in vivo* tissue. Although germanium detectors have higher quantum efficiency, the signal to noise ratio (SNR) is lower because these detectors are not suitable for single photon counting. To date, only one specific PMT detector has been reported for SOL detection under very strict measurement conditions, but use of this detector in clinics is still challenging due to its low quantum efficiency, high cost, and poor portability. Information on this PMT detector can be found below and in chapter 6.

The successful detection of singlet oxygen luminescence (SOL) in dye sensitization in solutions was first demonstrated using protoporphyrin in CCl_4 solvent and direct photomultiplier detection by Krasnovsky in 1976, and in 1979, Khan and Kasha detected it using methylene blue in aqueous solution and a thermoelectrically cooled lead sulfide detector (Krasnovskii 1976; Khan and Kasha 1979). Initial attempts made around the 1990s on $^1O_2$ luminescence detection in biological environments were mostly unsuccessful mainly due to the inadequate sensitivity of the systems or the low detectable SOL signal (Patterson *et al.* 1990). Although Parker (1987) reported the only positive results at that time from a single mouse tumor *in vivo* using a germanium detector, Patterson *et al.* (1990) failed to reproduce Parker's results under a number of biological conditions using the same detector system. From Patterson's experiments, the upper limit for the singlet oxygen lifetime was estimated at 0.5 μs in cell suspension or *in vivo* (Patterson *et al.* 1990). After Hamamatsu Corp. introduced a more sensitive photomultiplier tubes (PMT) with relatively high near-infrared quantum efficiency ($\sim$0.9%), the successful detection of SOL in biological systmes *in vitro* and *in vivo* was reported by two groups: Niedre *et al.* (2002) and Hirano and Nishiwaki (2002) in 2002. More detailed information on the SOL detection system used by Niedre will be discussed in Chapter 6. Niedre *et al.* (2002) demonstrated that SOL detection could be achieved in a series of samples ranging from simple sensitized aqueous solution, to solutions with Bovine serum albumin (BSA), to cell suspensions and eventually to *in vivo* rat liver and skin tissue.

The feasibility of SOL detection provides the fundamental base for direct dosimetry. Niedre *et al* investigated the relationship between the cumulative singlet oxygen luminescence (CSOL) and PDT-induced response of AML5 leukemia tumor cell suspensions sensitized with ALA-PpIX. The detected signals were found to be positively correlated to cell kill over widely varied treatment variables (Niedre *et al.* 2003). In a series of subsequent *in vivo* experiments on normal mouse skin with varied excitation light irradiance, Niedre *et al* found a good correlation of the cumulative SOL

signal to the skin response (Niedre *et al.* 2005). This study also found that the CSOL signal increased with decreased irradiance. These experimental results demonstrated the potential of direct dosimetry as a predictive tool for PDT-induced therapeutic responses.

The SOLD approach was investigated on normal human skin tissue using ALA-induced PpIX PDT (Laubach *et al.* 2008). However, the results were questionable because a lower SOL signal was sometimes detected from the sensitized area than from the control area. To date, no other studies have been performed on human subjects in order to evaluate the SOLD method.

Recently, a novel superconducting nanowire single photon detector (SNSPD) was used to successfully detect SOL from photosensitizer Rose Bengal in aqueous solution, and in solution with protein (BSA). This work was done via the collaboration among groups: Dr. Robert Hadfield from Heriot-Watt University, Dr. Brian Wilson from the University of Toronto and Dr. Mike Patterson from McMaster University. The author also participated in the initial experimental assessments of the SNSPD system. More details on this system can be found in Chapter 6 as well as a comparison with the current PMT detector system at the University of Toronto.

1.3 The motivation of the thesis

As briefly introduced in above sections, PDT is an inherently complex dynamic process. The distribution of each component can vary among patients before the treatment, and also changes during treatment. A continuous measure of single or all parameters in PDT is technically challenging and also inadequate to evaluate PDT effectiveness and to predict therapeutic outcomes.

Different PDT dosimetry approaches have been investigated in order to establish a widely accepted standard dose metric in clinical PDT. However, these approaches need to be theoretically and experimentally evaluated, ideally for specific photosensitizers under a wide range of treatment conditions, so their robustness can be tested and compared.

To date, it is difficult to examine all these approaches under a variety of treatment conditions in both pre-clinical and clinical studies, which implies that some comprehensive theoretical studies are desirable to understand PDT mechanism, to evaluate different PDT dosimetry approaches, and to guide future experimental studies. Although some PDT models have been developed to calculate PDT components, they all have some impractical assumptions such as uniform initial distribution of sensitizer (Nielsen *et al.* 2005; Wang *et al.* 2007, 2009). These remaining challenges initially motivated the present project.

The primary objectives of this project were: 1) to develop a dynamic one-dimensional model for ALA-PDT of normal human skin to simulate the dynamic progress of

ALA-PDT treatment, 2) to use the model to calculate time-resolved depth-dependent distributions of PDT components including light fluence, photosensitizer, ground-state oxygen, singlet-state oxygen and both PpIX fluorescence and singlet-oxygen luminescence emission signals escaped from skin surface, 3) to investigate the relationships between different PDT dose metrics and singlet-oxygen 'dose' averaged in a defined treated volume or at specific depth, and eventually to further examine the robustness of these correlations for various treatment conditions including varied initial concentration and distribution of sensitizer, different optical properties of tissue, different excitation light wavelength and irradiance.

Moreover, this project was designed as a theoretical guide to plan a pilot study of SOL detection during ALA-PDT on healthy human volunteers. The model can be used to interpret the experimental findings. For instance, the model can bridge the gap between the experimentally detected SOL signals and non-measurable singlet oxygen distributions in tissue. Eventually, given the observed PDT-induced skin responses and measured SOL signals, response can be correlated to volume-averaged singlet oxygen dose or singlet oxygen concentration at specific depths using the present model. Hence a chart of PDT-induced response versus singlet oxygen concentration can be obtained. The robustness of direct dosimetry can also be evaluated from this small human study and compared with the predicted results from the present model.

1.4 Fundamental information for the model of ALA-PDT for normal human skin

The model used a three-layer semi-infinite medium to represent normal human skin tissue. The Monte Carlo (MC) method was used to simulate both excitation and emission light propagating in tissue. The iterative calculations for updating PDT components during treatment were conducted in Matlab and were performed for each light exposure increment. The entire simulation process was managed by a graphical user interface (GUI) designed by the author as part of the project. The rest of this section will discuss some basic concepts for the model in general. More specific details about the model and assumptions in this model can be found in chapters 2 and 3.

1.4.1 Normal human skin

Skin is a complex heterogeneous organ in humans. Figure 1.2 illustrates human skin anatomy. It has three primary layers: epidermis (100 μm thick), dermis (1-4 mm thick) and hypodermis (or subcutaneous adipose layer) (Bashkatov *et al.* 2005). The epidermis has several sublayers including the outmost stratum corneum (SC) layer. The epidermis contains no blood vessels, oxygen can be supplied from diffusion from

the blood capillaries in the upper layers of the dermis and from the atmosphere above the skin. The very thin SC layer has a much lower water content than the underlying layers because it consists of dead cells. Due to its lower water content, oxygen diffusivity and solubility in the SC are much lower than in the other layers.

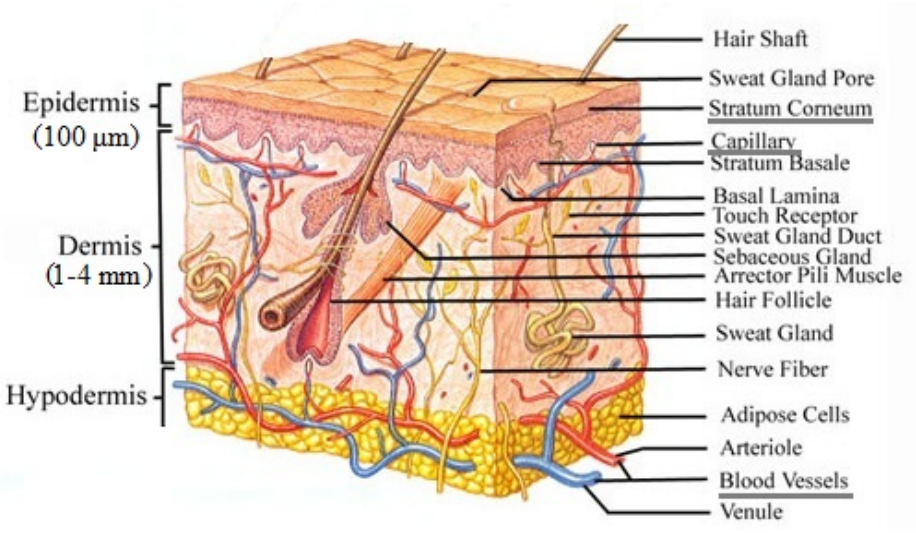

Figure 1.2: Human skin anatomy diagram. The original diagram was adopted from `http://www.freethought-forum.com/forum/showthread.php?t=11578&garpg=2` published by The Lone Ranger (2007). It has been slightly modified to fit the content.

The dermis contains mainly hair follicles, sweat glands, sebaceous glands and a rich vascular network. The blood vessel network mainly consists of the papillary loops and the horizontal superficial sub-papillary plexus. The oxygen perfusion from these vessels and oxygen diffusion provide nourishment to the cells. The hypodermis is actually not part of the skin, but it is a fatty tissue with vascular plexus below the dermis.

The optical properties of skin can be characterized mainly by the absorption and scattering coefficients. Various skin chromophores are responsible for the absorption of light in skin, and scattering of light is due to the refractive index variations on a microscopic level (Edwards and Duntley 1939; Young 1997; Schmitt and Kumar 1996). The main chromophores of human skin in the visible range are hemoglobin in the microvasculature of the dermis and melanin, mainly in the epidermis. Because of the great variation in the distributions of the vasculature and melanin in the skin, the optical properties of human skin, especially *in vivo*, are highly heterogeneous. This is even more pronounced for skin with disease conditions such as superficial basal cell carcinoma (sBCC) because the normal distributions of the blood vessel network can be

greatly varied in the disease area. Many studies have been conducted to investigate the optical properties of human skin (Edwards and Duntley 1939; Anderson and Parrish 1981; Graaff *et al.* 1993; Bashkatov *et al.* 2005; Salomatina *et al.* 2006). In the model introduced in this thesis, three-layer normal human skin with uniform optical properties within each layer but varied between layers was used to simplify the heterogeneity of optical properties. The absorption and scattering coefficients obtained from the study by Salomatina *et al.* (2006) were used for all the simulations. The same refractive index of 1.4 was used for all the layers in all simulations.

1.4.2 Monte Carlo method for light propagation in tissue

The Monte Carlo (MC) method is a well-established stochastic model that has been widely used for radiation transport studies. The rationale of the MC method for light-tissue interactions is to track the histories of individual photons while they are propagating in a tissue. In general, each individual absorption and scattering event in a photon history will be recorded until a history-ending event occurs under certain conditions. This recorded information can then be used to estimate the spatial distribution of light fluence rate in the tissue. With a sufficient number of simulated photon histories, the estimation can achieve enough accuracy to be used as a standard to verify analytical models such as the diffusion approximation. More detailed information on the MC method can be found elsewhere (Wang *et al.* 1995). A general introduction to the MC model for photon migration in a multilayer tissue with variable step size is discussed below. The specific method used in the present ALA-PDT model will be discussed in Chapter 3

Figure 1.3 shows a flow chart of a MC program. One photon with unit weight is initialized and launched from the origin ($x = 0, y = 0, z = 0$ in Cartesian coordinates). For a matched boundary multilayer tissue with different optical attenuation properties between layers, a step size Δs can be calculated via equation (1.4) using the maximum total attenuation from all the layers as $\mu_t^{\max}$ and a random number ξ between zero and one.

$$\Delta s = \frac{-\ln \xi}{\mu_t^{\max}} \,. \tag{1.4}$$

Then, the photon moves to a new position (x', y', z') calculated via equations (1.5) to (1.7), in which $\cos\theta_x$, $\cos\theta_y$ and $\cos\theta_z$ describe the photon propagation direction. This direction is specified by the cosine of the angle between the direction of travel and each axis, as denoted by the subscripts x, y and z.

$$x' = x + \cos\theta_x \Delta s \,, \tag{1.5}$$

$$y' = y + \cos\theta_y \Delta s \,, \tag{1.6}$$

$$z' = z + \cos\theta_z \Delta s \,. \tag{1.7}$$

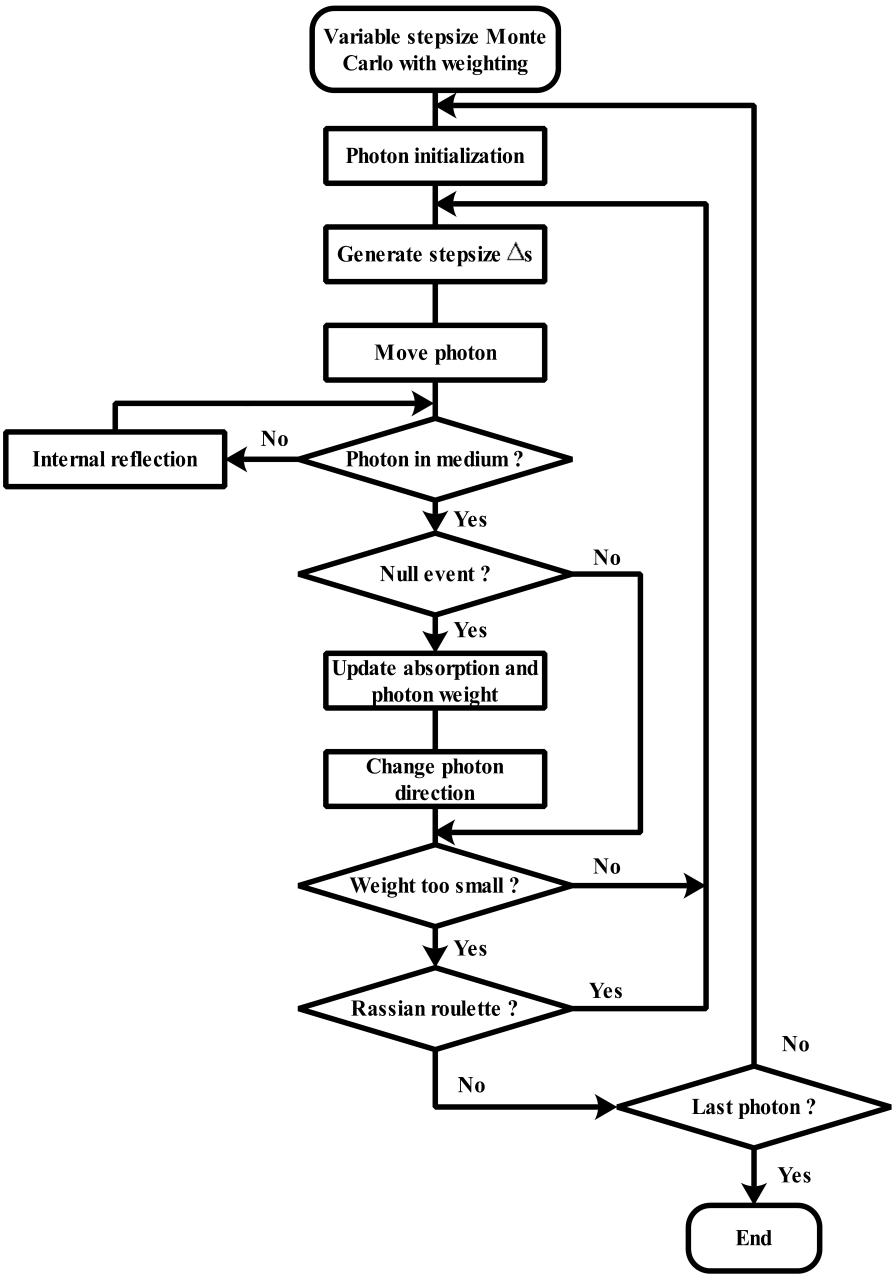

Figure 1.3: Flowchart for the variable stepsize Monte Carlo model for a multilayer medium.

Once the photon is located in its new position, an evaluation will be performed to verify whether or not it is still in the tissue. If not, a transmission and reflection event will be registered. The probability of the total internal reflection is determined by the Fresnel reflection coefficient $R(\theta_i)$ in equation (1.8), where $\theta_i = \cos^{-1}\cos\theta_z$ is the incident angle on the boundary and θ_t is the angle of transmission. Note that this step should be also performed whenever the photon crosses a mismatched boundary between two layers. If the photon is in the tissue, a null event should be tested to correct the underestimation of Δs before registering as a true event including absorption and scattering. The null event hypothesizes that no actual event occurs for underestimated Δs. During this test, a random number ξ will be compared to $\frac{\mu_t}{\mu_t^{\max}}$ where μ_t is the total attenuation coefficient at that position. For both internal reflection and true interaction events, the photon weight will be updated. The absorbed photon weight will be scored using the albedo ($\frac{\mu_s}{\mu_t}$) for observable quantity calculations later where μ_s is the scatter coefficient at that position.

$$R(\theta_i) = \frac{1}{2}\left[\frac{\sin^2(\theta_i-\theta_t)}{\sin^2(\theta_i+\theta_t)} + \frac{\tan^2(\theta_i-\theta_t)}{\tan^2(\theta_i-\theta_t)}\right] , \tag{1.8}$$

$$n_i \sin\theta_i = n_t \sin\theta_t . \tag{1.9}$$

After an interaction event, the direction of photon propagation will be updated using the standard Henyey-Greenstein phase function in equations (1.10) and (1.11), in which g is the mean cosine of the scattering angle (θ) also known as the scattering anisotropy parameter (ranging from zero to one). A larger value of g corresponds to more forward scattering of the photon. Typical values of g in biological tissues range from 0.9 - 0.98 (Cheong *et al.* 1990). The value of 0.9 was used in all present simulations.

$$\cos\theta = 2\xi - 1 , \tag{1.10}$$

$$\cos\theta = \frac{1}{2g}\left\{1+g^2-\left[\frac{1-g^2}{1-g+2g\xi}\right]^2\right\} . \tag{1.11}$$

After this, the photon termination procedure will be conducted to terminate photons with extremely small weight or having experienced so many scattering events that the weight of the photon is already very small but not small enough to be terminated from the other procedure. The whole procedure described above will then be iterated until all photons are simulated.

Detected emission photons, such as fluorescence escaping from a medium surface, are normally simulated in a temporally forward fashion using the above MC method. In this way, the fluorescence source distribution is derived at first from the simulated

excitation photon absorption distribution (i.e. excitation fluence rate distribution), and then the history of each fluorescence photon is recorded using the standard MC regardless if this tracked photon will contribute to the detected signal. This is inefficient especially for a model involving a great number of simulations and calculations. In contrast to this forward approach, the other approach, sometimes known as the adjoint method, is to backtrack only the detected emission photons to their origins. This adjoint method is described in more detail and experimentally validated by Crilly *et al.* (1997), and is applied in my model to calculate the detected emission signals. In the model, these calculations use fluence rate distributions simulated using optical properties at the excitation wavelength after each light exposure increment and at the emission wavelength before the entire simulation begins. An adjoint scaling factor similar to the importance function in Crilly *et al.* (1997) is defined and used for the calculations in the model. More details and the verification of the assumptions for using this reverse method can be found in Chapter 2.

1.4.3 Graphical user interface

A graphical user interface (GUI) was designed to make the management of the simulations user-friendly. The GUI was designed in the commercial software Matlab 2007 (The Mathwork Inc. Natick, MA). Figure 1.4 illustrates the current version of the GUI. The input components in the GUI are: basic parameters for MC simulation, optical properties of tissue, photobleaching mechanism options such as the first-order photobleaching and $^1O_2$-mediated second-order photobleaching, and treatment information including excitation wavelength and irradiance, treatment duration, initial drug concentration and distribution. The initial distribution of the sensitizer in the current GUI can be either exponential decay with tissue depth or a step-function distribution, but any non-uniform initial distribution could be easily added to the GUI. The MC simulation will be performed for each light exposure increment. In order to improve the time efficiency of the entire simulation, the GUI has a function that automatically determines the number of launched photon required for the MC once the relative standard error in the excitation light fluence at the specified depth is given.

Additionally, instead of the continuous simulation on real-time PDT, step-by-step simulation can also be manually controlled using the buttons on the right panel of the GUI. Plots of the calculated quantities versus time, depth or cumulative singlet oxygen can be quickly generated inside of the GUI.

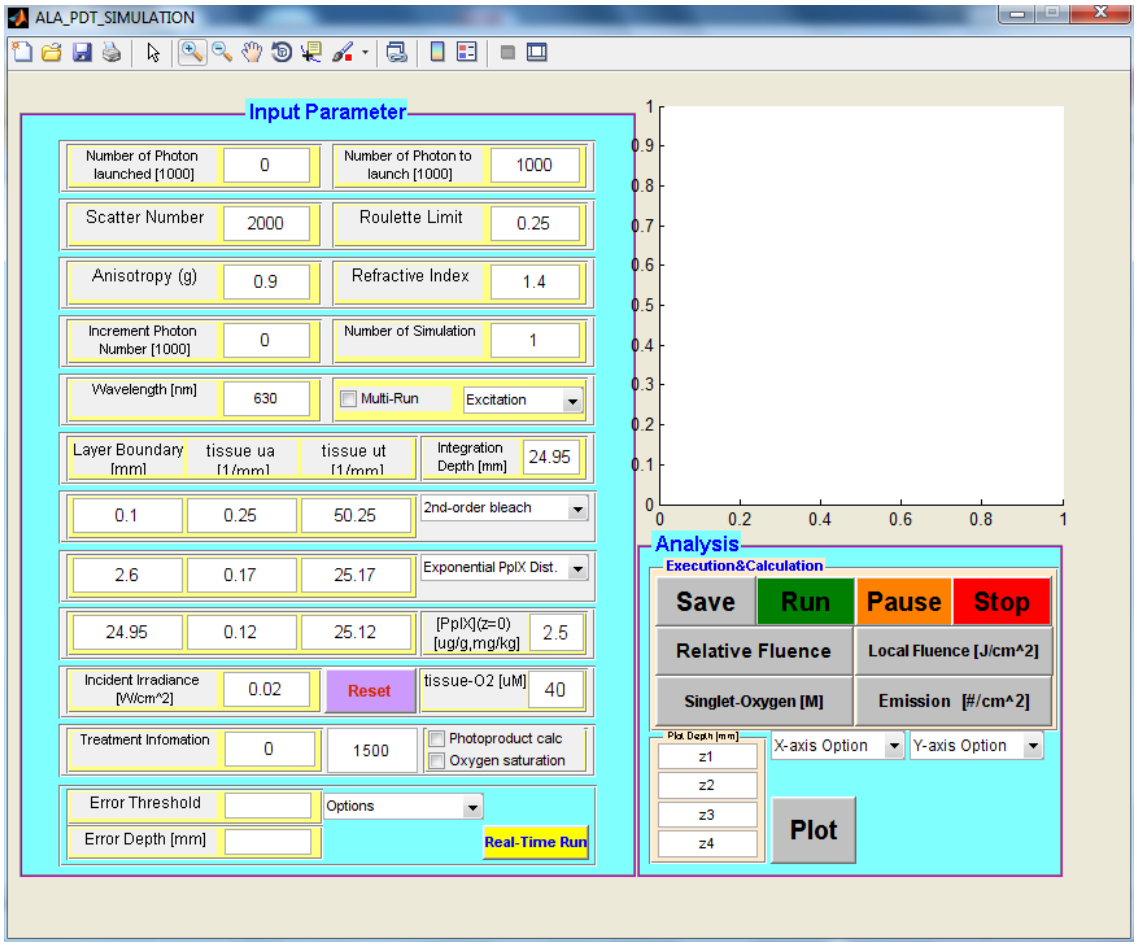

Figure 1.4: Graphical user interface.

1.5 The organization of the thesis

As aforementioned, the ultimate aim of this project is to develop a model to investigate the distributions of PDT factors and to evaluate different PDT dosimetry approaches for various treatment conditions. This goal is accomplished in several main steps which are described in the following chapters.

Chapter two is based on the author's published work below:

> **Baochang Liu**, Thomas J. Farrell, Michael S. Patterson, Mark T. Jarvi and Brian C. Wilson (2009) A Monte Carlo model of detected singlet oxygen luminescence and photosensitizer fluorescence during ALA-PDT of skin *Proc. SPIE* **7380**: 73806W1-11

This chapter mainly focuses on some fundamental hypotheses in the model and introduction of the preliminary stages of the model development. In order to calculate both sensitizer fluorescence and SOL emission using the simulated fluence distributions for the excitation light, the adjoint MC method was used and a scaling factor C_r was defined based on three assumptions. The first assumption is that the C_r is independent of optical properties of tissue for the same index of refraction. Second, the angular emission probability of emission photons on the surface should be independent of source depths. This allows use of normal incident light to calculate photon emission from various angles and all depths. The third assumption for using the adjoint method is that the absorption of the sensitizer should have negligible influence on the propagation of the emission photons. In this chapter, an empirical value of C_r is derived and used for all the simulations in this thesis, and the proof of the three hypotheses is also presented.

Chapter three is composed of my journal paper (Liu *et al.* 2010):

> **Baochang Liu**, Thomas J. Farrell and Michael S. Patterson (2010) A dynamic model for ALA-PDT of skin: simulation of temporal and spatial distributions of ground-state oxygen, photosensitizer and singlet oxygen *Phys. Med. Biol.* **55**: 5913-32

This chapter focuses on the detail of the dynamic model of ALA-PDT for normal human skin. In this chapter, the development of the model is described in much more detail as well as the choices of the simulation parameters. The performance of the model is evaluated by comparing the simulated PpIX fluorescence signals with clinical data from other investigators for normal human skin treated at six different irradiances. One hypothesis is proposed in this chapter, which is irradiance- and cumulative $^1O_2$-dependent vascular response. The time-resolved depth-dependent distributions of the main factors in PDT including ground-state and singlet-state

oxygen, sensitizer, and oxygen perfusion are calculated and introduced in this chapter. The calculated emission signals are also presented. The influence of oxygen diffusion on the quantity distributions, especially the singlet oxygen distribution, are discussed at the end of the chapter.

Chapter four consists of my third paper (Liu *et al.* 2012):

> **Baochang Liu**, Thomas J. Farrell and Michael S. Patterson (2012)
> Comparison of noninvasive photodynamic therapy dosimetry methods using a dynamic model of ALA-PDT of human skin *Phys. Med. Biol.* **57**: 825-41

In this chapter, noninvasive PDT dosimetry approaches are extensively examined for various treatment conditions. The scenarios include three treatment irradiances representing low, middle and high light exposure power, a wide range of optical properties of the dermis layer, and different initial sensitizer concentration and distribution. The three metrics are cumulative singlet oxygen luminescence (CSOL), absolute fluorescence bleaching metric (AFBM) and fractional fluorescence bleaching metric (FFBM). These metrics are correlated to the average reacted singlet oxygen dose in dermis and to the dose at specific depths. The robustness of these three metrics is compared for all different scenarios.

Chapter five introduces the manuscript recently accepted by *Journal of Biomedical optics*

> **Baochang Liu**, Thomas J. Farrell and Michael S. Patterson (2012)
> Comparison of photodynamic therapy with different excitation wavelengths using a dynamic model of ALA-PDT of human skin (submitted)

This chapter expands the results for single excitation wavelength (633 nm) discussed in chapter three and four to those for other two treatment wavelengths: green (523 nm) and blue (405 nm). Both the time evolution of depth-dependent distributions of the PDT components and comparison of different PDT dose metrics are discussed for all three wavelengths. The choice of these two light sources is based on the absorption peaks of sensitizer PpIX, and they have been either used clinically or studied for the optimal treatment wavelength for PDT. The specific study using 523 nm green light is also aimed to guide and interpret a future SOLD study on human volunteers using this laser source.

Chapter Six describes recent experimental work. Since singlet oxygen luminescence dosimetry (SOLD) has been our long-time goal for PDT dosimetry, recent work on SOL detection using a novel superconducting nanowire single photon detector (SNSPD) is introduced as well as some preliminary experimental results. Some descriptions about the currently used PMT detector are also included in this chapter.

Chapter seven will briefly summarize the thesis and propose possible future theoretical and experimental developments.

Bibliography

Anderson, R. R. and Parrish, J. A. (1981). The optics of human skin. *J. Invest. Dermatol.*, **77**, 13–19.

Bashkatov, A. N., Genina, E. A., Kochubey, V. I., and Tuchin, V. V. (2005). Optical properties of human skin, subcutaneous and mucous tissues in the wavelength range from 400 to 2000 nm. *J. Phys. D: Appl. Phys.*, **38**, 2543–55.

Brown, S. B., Brown, E. A., and Walker, I. (2004). The present and future role of photodynamic therapy in cancer treatment. *Lancet. Oncol.*, **5**, 497–508.

Cheong, W. F., Prahl, S. A., and Welch, A. J. (1990). A review of the optical properties of biological tissues. *IEEE J. Quantum Electron*, **26**, 2166–85.

Cottrell, W. J., Paquette, A. D., Keymel, K. R., Foster, T. H., and Oseroff, A. R. (2008). Irradiance-dependent photobleaching and pain in δ-aminolevulinic acid-photodynamic therapy of superficial basal cell carcinomas. *Clin. Cancer Res.*, **14**, 4475–4483.

Crilly, R. J., Cheong, W., Wilson, B., and Spears, J. R. (1997). Forward-adjoint fluorescence model: Monte Carlo integration and experimental validation. *Applied Optics*, **36**, 6513–19.

Dolmans, D. E., Fukumura, D., and Jain, R. K. (2003). Photodynamic therapy for cancer. *Nature Rev. Cancer*, **3**, 380–7.

Dougherty, T. J., Kaufman, J. E., Goldfarb, A., Weishaupt, K. R., Boyle, D., and Mittleman, A. (1978). Photoradiation therapy for the treatment of malignant tumors. *Cancer Res.*, **38**, 2628–35.

Dougherty, T. J., Lawrence, G., Kaufman, J. H., Boyle, D., Weishaupt, K. R., and Goldfarb, A. (1979). Photoradiation in the treatment of recurrent breast carcinoma. *J. Natl. Cancer Inst.*, **62**, 231–7.

Dysart, J. S. and Patterson, M. S. (2006). Photobleaching kinetics, photoproduct formation, and dose estimation during ALA induced PpIX PDT of MLL cells under well oxygenated and hypoxic conditions. *Photochem. Photobiol. Sci.*, **5**, 73–81.

Dysart, J. S., Singh, G., and Patterson, M. S. (2005). Calculation of singlet oxygen dose from photosensitizer fluorescence and photobleaching during mTHPC photodynamic therapy of MLL cells. *Photochem. Photobiol.*, **81**, 196–205.

Edwards, E. A. and Duntley, S. Q. (1939). The pigment and color of human skin. *Am. J. Anat.*, **65**, 1–33.

Finlay, J. C., Mitra, S., Patterson, M. S., and Foster, T. H. (2004). Photobleaching kinetics of Photofrin *in vivo* and in multicell tumor spheroids indicate two simultaneous bleaching mechanisms. *Phys. Med. Biol.*, **49**, 4837–60.

Finlay, J. C., Zhu, T. C., Dimofte, A., Stripp, D., Malkowicz, S. B., Busch, T. M., and Hahn, S. M. (2006). Interstitial fluorescence spectroscopy in the human prostate during Motexafin Lutetium-mediated photodynamic therapy. *Photochem. Photobiol.*, **82**, 1270–8.

Graaff, R., Dassel, A. C. M., Koelink, M. H., de Mul, F. F. M., Aarnoudse, J. G., and Zijlstra, W. G. (1993). Optical properties of human dermis *in vitro* and *in vivo*. *Appl. Opt.*, **32**, 435–47.

Hirano, T. K. E. and Nishiwaki, M. (2002). Detection of near infrared emission from singlet oxygen in PDT with an experimental tumor bearing mouse. *J. Japan. Soc. Laser Surg. Med*, **22**, 99–108.

Kennedy, J. C., Pottier, R. H., and Pross, D. C. (1990). Photodynamic therapy with endogenous protoporphyrin IX: basic principles and present clinical experience. *J. Photochem. Photobiol. B.*, **6**, 143–8.

Khan, A. U. and Kasha, M. (1979). Direct spectroscopic observation of singlet oxygen emission at 1268 nm excited by sensitizing dyes of biological interest in liquid solution. *Proc. Natl. Acad. Sci.*, **76**, 6047–49.

Krasnovskii, A. A. (1976). Photosensitized luminescence of singlet oxygen in solution. *Biofizika*, **21**, 748–9.

Laubach, H. J., Chang, S. K., Lee, S., Rizvi, I., Zurakowski, D., Davis, S. J., Taylor, C. R., and Hasana, T. (2008). *In-vivo* singlet oxygen dosimetry of clinical 5-aminolevulinic acid photodynamic therapy. *J. Biomed. Opt.*, **13**.

Liu, B., Farrell, T. J., and Patterson, M. S. (2010). A dynamic model for ALA-PDT of skin: simulation of temporal and spatial distributions of ground-state oxygen, photosensitizer and singlet oxygen. *Phys. Med. Biol.*, **55**, 5913–32.

Liu, B., Farrell, T. J., and Patterson, M. S. (2012). Comparison of noninvasive photodynamic therapy dosimetry methods using a dynamic model of ALA-PDT of human skin. *Phys. Med. Biol.*, **57**, 825–41.

Moan, J. and Peng, Q. (2003). An outline of the hundred-year history of PDT. *Anticancer Res.*, **23**, 3591–600.

Niedre, M., Patterson, M. S., and Wilson, B. C. (2002). Direct near-infrared luminescence detection of singlet oxygen generated by photodynamic therapyin cells *in vitro* and tissues *in vivo*. *Photochem. Photobiol*, **75**, 382–91.

Niedre, M. J., Secord, A. J., Patterson, M. S., and Wilson, B. C. (2003). *In vitro* tests of the validity of singlet oxygen luminescence measurements as a dose metric in photodynamic therapy. *Cancer Res.*, **63**, 7986–94.

Niedre, M. J., Yu, C. S., Patterson, M. S., and Wilson, B. C. (2005). Singlet oxygen luminescence as an *in vivo* photodynamic therapy dose metric: validation in normal mouse skin with topical amino-levulinic acid. *Br. J. Cancer*, **92**, 298–304.

Nielsen, K. P., Juzeniene, A., Juzenas, P., Stamnes, K., Stamnes, J. J., and Moan, J. (2005). Choice of optimal wavelength for PDT: the significance of oxygen depletion. *Photochem. Photobiol.*, **81**, 1190–4.

O'Connor, A. E., Gallagher, W. M., and Byrne, A. T. (2009). Porphyrin and nonporphyrin photosensitizers in oncology: preclinical and clinical advances in photodynamic therapy. *Photochem. Photobiol.*, **85**, 1053–74.

Parker, J. G. (1987). Optical monitoring of singlet oxygen during photodynamic treatment of tumors. *IEEE Circ. Devices Mag.*, **Jan**, 10–21.

Patterson, M. S., Madsen, S. J., and Wilson, B. C. (1990). Experimental tests of singlet oxygen luminescence monitoring *in vivo* during photodynamic therapy. *J. Photochem. Photobiol. B.*, **5**, 69–84.

Robinson, D. J., de Bruijn, H. S., van der Veen, N., Stringer, M. R., Brown, S. B., and Star, W. M. (1998). Fluorescence photobleaching of ALA-induced protoporphyrin IX during photodynamic therapy of normal hairless mouse skin: the effect of light dose and irradiance and the resulting biological effect. *Photochem. Photobiol.*, **67**, 140–9.

Salomatina, E., Jiang, B., Novak, J., and Yaroslavsky, A. N. (2006). Optical properties of normal and cancerous human skin in the visible and near-infrared spectral range. *J. Biomed. Opt.*, **11**.

Schmitt, J. M. and Kumar, G. (1996). Turbulent nature of refractive-index variations in biological tissue. *Opt. Lett.*, **21**, 1310–2.

Tyrrell, J., Thorn, C., Shore, A., Campbell, S., and Curnow, A. (2011). Oxygen saturation and perfusion changes during dermatological methylaminolaevulinate photodynamic therapy. *Br. J. Dermatol.*, **165**, 1323–31.

Wang, K. K., Mitra, S., and Foster, T. H. (2007). A comprehensive mathematical model of microscopic dose deposition in photodynamic therapy. *Med. Phys.*, **34**, 282–93.

Wang, K. K., Cottrell, W. J., Mitra, S., Oseroff, A., and Foster, T. H. (2009). Simulations of measured photobleaching kinetics in human basal cell carcinomas suggest blood flow reductions during ALA-PDT. *Lasers Surg. Med.*, **41**, 686–96.

Wang, L., Jacques, S. L., and Zheng, L. (1995). MCML - Monte Carlo modeling of light transport in multi-layered tissues. *Comput. Meth. Prog. Bio.*, **47**, 131–46.

Weishaupt, K. R., Gomer, C. J., and Dougherty, T. J. (1976). Identification of singlet oxygen as the cytotoxic agent in photo-inactivation of a murine tumor. *Cancer Res.*, **36**, 2326–29.

Wilson, B. C. and Patterson, M. S. (2008). The physics, biophysics and technology of photodynamic therapy. *Phys. Med. Biol.*, **53**, R61–R109.

Young, A. R. (1997). Chromophores in human skin. *Phys. Med. Biol.*, **42**, 789–802.

Zeng, H. S., Korbelik, M., Mclean, D. I., MacAulay, C., and Lui, H. (2002). Monitoring photoproduct formation and photobleaching by fluorescence spectroscopy has the potential to improve PDT dosimetry with a verteporfin-like photosensitizer. *Photochem. Photobiol.*, **75**, 398–405.

Chapter 2

Paper I - A Monte Carlo model of detected singlet oxygen luminescence and photosensitizer fluorescence during ALA-PDT of skin

Baochang Liu[a,b], **Thomas J. Farrell**[a,b], **Michael S. Patterson**[a,b], **Mark T. Jarvi**[c] **and Brian C. Wilson**[c]

a Department of Medical Physics and Applied Radiation Sciences, McMaster University, 1280 Main Street West, Hamilton, Ontario, Canada, L8S 4K1;
b Department of Medical Physics, Juravinski Cancer Centre, 699 Concession Street, Hamilton, Ontario, Canada, L8V 5C2;
c Department of Medical Biophysics, Ontario Cancer Institute and University of Toronto, 610 University Avenue, Toronto, Ontario, Canada, M5G 2M9.

Published in Proceedings of SPIE, 2009, **7380**, 73806W
Printed with permission
 [DOI: 10.1117/12.823032]

Introduction to paper I

In this Chapter, some fundamental hypotheses in the model will be proposed and discussed. In the model, sensitizer fluorescence and SOL emission signals were calculated using the simulated fluence distributions of the excitation light. To do this, the adjoint MC method was adapted with the introduction of a adjoint scaling factor C_{r}. The derivation of the empirical value of C_{r} and the proof of three hypothesized assumptions for using it are shown in this chapter. In addition, the first stage of development of the model and some preliminary simulation results are presented.

I modified the initial general Monte Carlo (MC) code from Dr. Farrell specifically for the use in my project. Dr. Farrell helped me with the development of this new MC algorithm. I performed all the simulations and analyzed the results with very helpful suggestions and discussions from Drs. Patterson, Farrell, Jarvi and Wilson. The manuscript was written by me and edited by Dr. Patterson who also supervised my entire work.

Contents of Paper I

Abstract

Singlet oxygen luminescence dosimetry (SOLD) and fluorescence photobleaching are being investigated as dosimetric tools for clinical PDT. Both have been applied during superficial ALA-PDT of normal skin and skin cancers. The interpretation of fluorescence and SOLD data is complicated by the non-uniform distribution and bleaching of PpIX and the absorption and scattering of light in the skin. The aim of the present work was to tackle these challenges using Monte Carlo (MC) simulations. Skin was modeled as a three-layer semi-infinite medium with uniform optical properties in each layer. The initial depth-dependent distribution of PpIX was an exponential decay and, after the delivery of each treatment fluence increment, standard photochemical reaction kinetics were used to update the distribution of sensitizer and reacted singlet oxygen. Oxygen depletion due to photochemical consumption or vascular shutdown was also incorporated in the model. The adjoint method was applied to calculate the PpIX fluorescence and 1270 nm singlet oxygen luminescence reaching the skin surface in each time increment. The time-resolved evolution of the fluorescence and cumulative SOLD signals during treatment were compared to the time-resolved volume-averaged distribution of reacted singlet oxygen in the dermis layer for typical clinical PDT conditions. Approximate linear relationships were observed over most of the treatment time.

2.1 Introduction

Photodynamic therapy (PDT) utilizes light to activate light sensitive drugs called photosensitizers to treat diseases such as cancer and age-related macular degeneration. ALA-PDT is the use of the prodrug aminolevulinic acid (ALA) to endogenously generate the photosensitizer Protoporphyrin IX (PpIX) via the heme biosynthetic pathway. One typical example of the application of ALA-PDT is for the treatment of human skin diseases such as actinic keratoses (AK) and basal cell carcinoma (BCC). The PDT dosimetry problem has been investigated for many years, and the three approaches incorporating the indirect or direct monitoring of the amount of singlet oxygen ($^1O_2$) produced during the PDT treatment are explicit dosimetry, implicit dosimetry and direct dosimetry (Wilson and Patterson 2008).

Implicit dosimetry is based on monitoring the photosensitizer photobleaching mechanism via detecting photosensitizer fluorescence signal. This dosimetry has been extensively investigated and has had some preclinical success. Direct dosimetry is directly monitoring the production of $^1O_2$ via detecting its characteristic 1270 nm

phosphorescence. This approach is also called singlet oxygen luminescence dosimetry (SOLD). Given that the excited singlet oxygen is considered to be the primary cytotoxic agent causing the biological damage, SOLD may be considered as the gold standard. The feasibility of detection of the weak 1270 nm luminescence signal has been demonstrated using animal models by Niedre *et al.* (2002) and Hirano and Nishiwaki (2002), and has been reported in humans by Laubach *et al.* (2008). Both fluorescence photobleaching and SOLD are being applied during superficial ALA-PDT of normal skin and skin cancer as dosimetric tools. However, because of the non-uniform distribution and photobleaching of drug, the absorption and scattering properties of skin, and oxygen depletion during PDT, the interpretation of fluorescence and SOL signals remains complicated. The correlation of the actual amount of singlet oxygen generated in skin with the detected emission signals is still not clear. These challenges motivated the present study.

The present work used the Monte Carlo (MC) method to simulate PDT in normal human skin. Skin was modeled as a three-layer semi-infinite medium with uniform optical properties within each layer. Two types of initial depth-dependent distribution of PpIX were investigated: a step-function distribution between epidermis and dermis, and an exponential decay with the skin depth. Following the delivery of each fluence increment, the updated depth-dependent distribution of PpIX was investigated using two photobleaching mechanisms. One was the first-order mechanism in which sensitizer was bleached exponentially with local fluence, and the other was the second-order mechanism in which standard photochemical reaction kinetics were used with ground-state oxygen ($^3O_2$) depletion and replenishment. The hypothesis introduced in the second-order mechanism was that blood flow at every depth was reduced as a function of cumulative singlet oxygen dose at that depth. The adjoint method was used to calculate both the PpIX fluorescence at 705 nm and the 1270 nm singlet oxygen luminescence reaching the skin surface. Furthermore, the depth distribution of reacted singlet oxygen was also calculated. The time-resolved emission signals and distribution of $^1O_2$ were obtained via the iteration of the MC simulation for delivery of each fluence increment. The original MC code was written in PASCAL, and the execution of the simulations and the calculations were managed by a graphical user interface (GUI) created using Matlab 7.5.0. The typical clinical ALA-PDT conditions of 100 mW/cm^2 irradiance at 633 nm wavelength were investigated. The detailed description of this model follows in section 2.2.

2.2 Theory and Method

2.2.1 The standard and adjoint Monte Carlo methods for light fluence and emission in multi-layered skin tissue

The simplified skin model for this study consists of three layers that are epidermis, dermis and subcutaneous fat with thicknesses of 100 μm, 2500 μm and infinite respectively. Absorption coefficient (μ_a) and reduced scattering coefficient (μ_s') of normal human skin at the wavelengths of interest were assumed to be uniform in each layer, and are listed in Table 2.2. All three layers were considered to have the same refractive index of 1.4.

Table 2.2: Optical properties of normal human skin. Data were extracted from Salomatina *et al.* (2006). The wavelengths of 523, 633, 705 and 1270 nm are the excitation, fluorescence and phosphorescence wavelengths respectively. μ_a : absorption coefficient; μ_s' : reduced scattering coefficient; unit: mm^{-1}.

		523 (nm)		633 (nm)		705 (nm)		1270 (nm)	
Tissue	Thickness (mm)	μ_a	μ_s'	μ_a	μ_s'	μ_a	μ_s'	μ_a	μ_s'
Epidermis	0.1	0.5	6	0.25	5	0.25	4	0.05	2.5
dermis	2.5	0.3	4	0.17	2.5	0.15	2.5	0.1	1.6
Sub-Q	infinite	0.45	3	0.12	2.5	0.12	2.3	0.1	1.5

The Monte Carlo (MC) algorithm for this study was almost the same as introduced in most text books. Because of the different attenuation coefficients in the different layers, the delta-scattering technique was used (Wang *et al.* 1997). The maximum total attenuation coefficient from the three tissue layers was used to sample the step size (Δs) everywhere. A null event was sampled for at each interaction location in order to correct the underestimation of Δs prior to both updating photon weight and scoring procedures. The internal reflection occurring at the mismatched boundary of the top skin surface was taken into account by the Fresnel reflection equation. Photons were tracked to a maximum depth of 24.95 mm. The backscattered photons at this boundary were also tracked and scored. Furthermore, in order to make the simulations more time efficient, the maximum relative variance in the fluence at a specified depth was entered via the GUI. Consequently, the program stops launching photons once the relative variance at the defined depth is satisfied for each fluence increment.

The simulation of emission photon propagation from interior to the surface can be performed in several different ways. The standard (forward) method is to track each photon from its origin to the detector or tissue surface. However, this method is

inefficient in two ways: photons that have been tracked may not eventually contribute to the detected emission signal and the emissions from all depths need to be simulated independently.

Therefore, the adjoint (reverse) approach Monte Carlo method was used for this study (Crilly *et al.* 1997). This method is to backtrack an emission photon from the tissue surface to its origin, which means the previous MC method for light fluence can also be used to simulate emission light with some adjoint scaling factor (C_{r}). The adjoint scaling factor (C_{r}) as expressed in equation (2.12) was defined as the ratio of the relative emission from an isotropic point source at the depth z to the relative fluence at the same depth from a broad beam source at the surface.

$$C_{\mathrm{r}}(z) = \frac{\text{Relative emission}(z)}{\text{Relative fluence}(z)} \ . \tag{2.12}$$

Several assumptions for using C_{r} were applied. First, C_{r} should be independent of the optical properties of tissue for the same index of refraction. Second, the angular emission probability distribution should be depth-independent such that a photon can be launched in the normal direction to the tissue surface in the reverse case instead of from various angles with different photon weight. The verifications of these two assumptions and the derivation of C_{r} will be described in section 2.3. Another assumption for this approach is that the photosensitizer absorption has no significant effect on emission photon propagation. This assumption could be adopted, first because PpIX has very low absorption coefficient at 705 nm and 1270 nm, and secondly because of the relatively small contribution to the absorption of tissue from such a low concentration of photosensitizer (2.5 μg/g used for all simulations).

2.2.2 Photobleaching mechanism approximations and the calculations of singlet oxygen concentration, detected singlet oxygen luminescence and photosensitizer fluorescence signals

This study examines two types of photobleaching: the first order photobleaching mechanism in which drug concentration was bleached exponentially by local light fluence and the second order mechanism using standard photochemical reaction kinetics. The first order approximation is expressed in equation (2.13),

$$\mathrm{S}_0(t) = \mathrm{S}_0(t=0) \times e^{-\frac{\text{local fluence}(t)}{\text{bleaching fluence}}} \ , \tag{2.13}$$

where bleaching fluence is the excitation wavelength dependent constant defined as the fluence required to reduce PpIX to 1/e of its initial concentration. The choices of

this constant for the 633 nm excitation wavelength were 50 J/cm^2 (Svaasand *et al.* 1996) and 5 J/cm^2 estimated from Cottrell *et al.* (2008). With the updated PpIX concentration, the depth-dependent $^1O_2$ production rate was proportional to fluence rate, PpIX absorption cross section and the averaged PpIX concentration before and after each fluence increment.

The first order approximation is appropriate for a well oxygenated tissue; while, for *in vivo* tissue with oxygen depletion during PDT, the photobleaching of drug can be dependent on the combination of instaneous oxygen and drug concentration and light fluence rate. The second order approximation considering simultaneous $^1O_2$- and sensitizer triplet- mediated bleaching was explained in detail in S. Mitra's Ph.D thesis (Mitra 2004). A brief introduction can be found in Appendix 2.5.1. Besides the ground-state oxygen ($^3O_2$) consumption due to PDT, the metabolic consumption of $^3O_2$ during PDT was taken into account using Michaelis-Menten kinetics (Hudson and Cater 1964) as expressed in equation (2.14), where $\Gamma_{\text{met}}^{\max}$ is the initial maximum metabolic consumption rate of human skin for the steady state, and k_{50} is the $^3O_2$ concentration at which Γ_{met} is half of $\Gamma_{\text{met}}^{\max}$. The total consumption of $^3O_2$ involves both the Γ_{met} and the Γ_{PDT} contributions. In addition, the ground-state oxygen supply at each depth in skin, as shown in equation (2.15), was modeled as perfusion with a rate of K across a barrier between a well-oxygenated blood vessel and its surrounding tissue. It is assumed that the oxygen perfused into tissue will quickly diffuse within the same layer but not to other layers. Another hypothesis introduced was that blood flow was reduced as a function of the cumulative $^1O_2$ dose, commensurate with damage to blood vessels. This is expressed in equation (2.16) where D_{50} is the $^1O_2$ dose required to reduce K to half of its initial value and α is the slope of the sigmoid function. The initial K_0 was determined such that the initial $^3O_2$ supply equals its metabolic consumption prior to the PDT irradiation.

$$\Gamma_{\text{met}} = \Gamma_{\text{met}}^{\max} \frac{[^3O_2]}{k_{50} + [^3O_2]} , \tag{2.14}$$

$$\left(\frac{\mathrm{d}[^3O_2]}{\mathrm{d}t}\right)_{\text{supply}} = K\left([^3O_2]_{\text{vessel}} - [^3O_2]\right) , \tag{2.15}$$

$$K(t) = K_0\left(1 - \frac{1}{1 + e^{-\alpha(\int_0^t [^1\dot{O}_2](t')\mathrm{d}t' - D_{50})}}\right) . \tag{2.16}$$

With the above hypotheses and the derivations of Γ_{PDT} from Appendix 2.5.1, coupled differential equations governing the concentrations of ground-state PpIX and oxygen were obtained and shown in equations (2.17) and (2.18). The variables and notations refer to Table 2.4. Most of the photophysical and physiological parameters have been investigated for the cell spheroid model. The parameters shown in Table 2.3 for *in vivo* human skin were estimated from the published values for the *in vitro*

model. However, due to the lack of knowledge of the ratio $\frac{k_{\mathrm{d}}}{k_{\mathrm{oa}}[\mathrm{A}]}$ in the literature and the initial non-uniform sensitizer distribution, β'_{PDT} was defined as equation (2.21).

$$\begin{aligned}\frac{\mathrm{d}\left[\mathrm{S}_0\right]}{\mathrm{d}t} &= -\phi_{\mathrm{t}} I_{\mathrm{a}} \frac{k_{\mathrm{ta}}\left[\mathrm{A}\right]/k_{\mathrm{ot}}}{k_{\mathrm{p}}/k_{\mathrm{ot}} + k_{\mathrm{ta}}\left[\mathrm{A}\right]/k_{\mathrm{ot}} + \left[^3\mathrm{O}_2\right]} \\ &\quad \times \left[1 + \frac{\frac{k_{\mathrm{os}}}{k_{\mathrm{oa}}[\mathrm{A}]}}{k_{\mathrm{ta}}\left[\mathrm{A}\right]/k_{\mathrm{ot}}} \frac{S_\Delta}{\frac{k_{\mathrm{d}}}{k_{\mathrm{oa}}[\mathrm{A}]} + 1} \left(\left[\mathrm{S}_0\right] + \delta\right)\left[^3\mathrm{O}_2\right]\right] , \end{aligned} \tag{2.17}$$

$$\frac{\mathrm{d}\left[^3\mathrm{O}_2\right]}{\mathrm{d}t} = -\Gamma_{\mathrm{PDT}} - \Gamma_{\mathrm{met}}^{\max} \frac{\left[^3\mathrm{O}_2\right]}{k_{50} + \left[^3\mathrm{O}_2\right]} + K(\left[^3\mathrm{O}_2\right]_{\mathrm{vessel}} - \left[^3\mathrm{O}_2\right]) , \tag{2.18}$$

where:

$$\Gamma_{\mathrm{PDT}} = -S_\Delta I_{\mathrm{a}} \phi_{\mathrm{t}} \frac{1}{\frac{k_{\mathrm{d}}}{k_{\mathrm{oa}}[\mathrm{A}]} + 1} \left[1 + \frac{k_{\mathrm{os}}}{k_{\mathrm{oa}}\left[\mathrm{A}\right]}(\left[\mathrm{S}_0\right] + \delta)\right] \times \frac{\left[^3\mathrm{O}_2\right]}{k_{\mathrm{p}}/k_{\mathrm{ot}} + \frac{k_{\mathrm{ta}}[\mathrm{A}]}{k_{\mathrm{ot}}} + \left[^3\mathrm{O}_2\right]} , \tag{2.19}$$

$$I_{\mathrm{a}} = \frac{\sigma_{\mathrm{S}_0} \dot{F}_{\mathrm{ex}}}{h\nu} \left[\mathrm{S}_0\right] , \tag{2.20}$$

$$\beta'_{\mathrm{PDT}} = S_\Delta \phi_{\mathrm{t}} \frac{\sigma_{\mathrm{S}_0}}{h\nu} \frac{1}{\frac{k_{\mathrm{d}}}{k_{\mathrm{oa}}[\mathrm{A}]} + 1} . \tag{2.21}$$

The coupled differential equations with the parameters in Table 2.3 were solved simultaneously after MC simulation for each fluence increment to update the depth dependent concentrations of $^3\mathrm{O}_2$ and PpIX. Then, the production of $^1\mathrm{O}_2$ and both simultaneous fluorescence at 705 nm and singlet oxygen luminescence (SOL) at 1270 nm could be computed via equations (2.22), (2.23) and (2.24). The cumulative quantities were obtained via time integration. Meanwhile, the oxygen supply rate K was also updated using equation (2.16). The iteration of MC simulation followed by these computations enabled the time-resolved calculation of $^1\mathrm{O}_2$ concentration at depth, photosensitizer fluorescence and SOL.

$$\left[^1\dot{\mathrm{O}}_2\right] = I_{\mathrm{a}} \Phi_{\mathrm{D}} \frac{\left[^3\mathrm{O}_2\right]}{k_{\mathrm{p}}/k_{\mathrm{ot}} + \frac{k_{\mathrm{ta}}[\mathrm{A}]}{k_{\mathrm{ot}}} + \left[^3\mathrm{O}_2\right]} , \tag{2.22}$$

$$\dot{\mathrm{E}}_{\mathrm{m705}} = \int_0^\infty \dot{F}_{\mathrm{ex}}(z) \mu_{a,\mathrm{d}}(z) \phi_{\mathrm{f}} F_{\mathrm{em}_{705}}(z) C_{\mathrm{r}} \mathrm{d}z , \tag{2.23}$$

$$\dot{\mathrm{E}}_{\mathrm{m1270}} = \int_0^\infty \left[^1\dot{\mathrm{O}}_2\right](z) \phi_{\mathrm{d}} F_{\mathrm{em}_{1270}}(z) C_{\mathrm{r}} \mathrm{d}z , \tag{2.24}$$

where $\dot{F}_{\mathrm{ex}}(z)$ and $F_{\mathrm{em}}(z)$ are the fluence rate and relative fluence at the excitation and

corresponding emission wavelengths respectively; $\mu_{a,\mathrm{d}}(z)$ is the absorption coefficient of photosensitizer; ϕ_{f}, ϕ_{d} are the fluorescence and phosphorescence quantum yield and C_{r} is the adjoint scaling factor defined in equation (2.12).

Table 2.3: Photophysical and Physiological Parameters.

Parameters	Values	Reference	Units
$k_{\mathrm{os}}/k_{\mathrm{oa}}\,[\mathrm{A}]$	85		M^{-1}
$\Gamma_{\mathrm{met}}^{\mathrm{max}}$	0.9		$\mu\mathrm{Ms}^{-1}$
$k_{\mathrm{ta}}\,[\mathrm{A}]\,/k_{\mathrm{ot}}$	1×10^{-5}		$\mu\mathrm{M}$
K_0	0.0222		s^{-1}
$k_{\mathrm{p}}/k_{\mathrm{ot}}$	4		$\mu\mathrm{M}$
δ	210		$\mu\mathrm{M}$
k_{50}	0.5	(Wang *et al.* 2007)	$\mu\mathrm{M}$
$[^3\mathrm{O}_2]_{\mathrm{vessel}}$	80		$\mu\mathrm{M}$
α	1		mM^{-1}
$[^3\mathrm{O}_2]_0$	40		$\mu\mathrm{M}$
ϵ_{PpIX}	3000		$\mathrm{M}^{-1}\mathrm{cm}^{-1}$
D_{50}	5		mM
β'_{PDT}	0.021		
ϕ_{f}	0.05		
Φ_{D}	0.57	(Keene *et al.* 1986)	

2.3 Results and Discussions

2.3.1 The derivation of the adjoint scaling factor

As introduced in section 2.2, an adjoint scaling factor (C_{r}) needs to be derived to use the adjoint approach. Therefore, emission signals as functions of the isotropic point source depth were calculated for the wavelengths of 523 nm, 633 nm and 1270 nm using the optical properties in Table 2.2. The source depths were 1, 2, 3, 4, 5, 6, 8, 10, 12, 14, 16, 18, 20, 22 and 24.95 mm. Also, the fluence from a broad beam perpendicularly incident into the tissue at these three wavelengths was simulated. The ratios of total emission to the fluence at the chosen depths were calculated and plotted in Figure 2.5 left panel. One can see the ratios for all three wavelengths were consistent up to the tissue thickness of 5 mm. The average of this consistent ratio was 0.114 $\pm$ 0.002. Beyond 5 mm the data are consistent with the 0.114 value for the ratio, but suffer from increased variance due to reduced photon counts at these depths. Furthermore, the ratios for some other optical properties with the lowest

limit of $\mu_a = 0.001$ and $\mu_s' = 0.5$ were tested for the same refractive index and gave the same value of C_r; and the ratios for the same optical properties with the refractive indexes of 1 and 1.33 were also investigated and the resultant ratios were 0.198 ± 0.002 and 0.1275 ± 0.0007 respectively. As expected, the C_{r} demonstrated the independence on the optical coefficients within the range of the tissue thickness, and it was determined by the refractive index only.

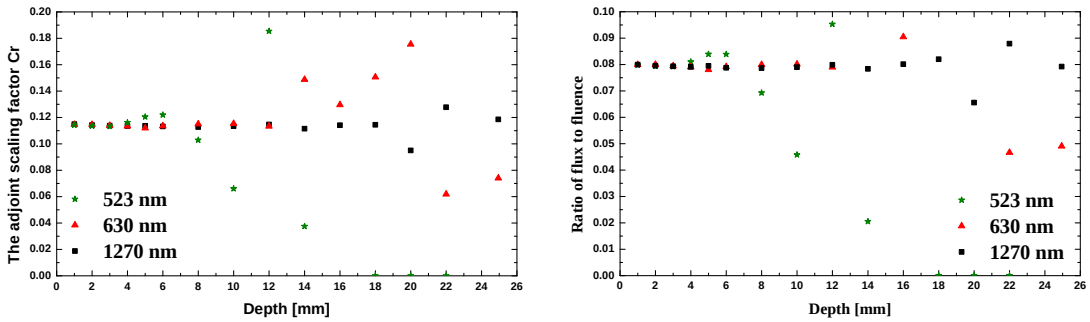

Figure 2.5: The calculated adjoint scaling factors (left) and the ratio of the flux to the fluence (right). The refractive index is 1.4. Unit: number of emitted photons at the surface per launched photon at a depth z per unit relative fluence.

In addition, the ratios of the light flux to the relative fluence were calculated using the same simulation results as those for the C_{r} calculation, and shown in Figure 2.5 right panel. According to Swartling *et al.* (2003), the relationship between the fluence at a depth z in the reverse case and the light flux emitted at the surface in the forward case can be expressed as equation (2.25),

$$F_{\mathrm{rev}}(z) = \frac{P_{\mathrm{rev}}}{P_{\mathrm{fwd}}} * \frac{4\pi}{\Delta\Omega} * \Phi_{\mathrm{fwd}}(z=0) \ , \tag{2.25}$$

where $\mathrm{F_{rev}(z)}$ is the fluence at a depth z in the reverse situation; $\Phi_{\mathrm{fwd}}(z{=}0)$ is the light flux in the forward case; $\mathrm{P_{rev}}$ and $\mathrm{P_{fwd}}$ are the point source powers in two cases; $\Delta\Omega$ is the solid angle corresponding to the total internal reflection critical angle. Note that the light source used in the reverse case for this study was a broad beam source instead of a point source, hence the point source should have twice the power as that of the broad beam to produce the same radiance. In addition, the refractive index of 1.4 was used to calculate $\Delta\Omega$. Therefore, equation (2.25) can be rewritten as equation (2.26) given that the power of the broad beam was the same as $\mathrm{P_{fwd}}$. Compared with the calculated value of 0.075, the simulated ratios at depths less than 5 mm are within

6.7%.

$$\frac{\Phi_{\text{fwd}}(z=0)}{F_{\text{rev}}(z)} = \frac{\Delta\Omega}{8\pi} = 0.075\ . \tag{2.26}$$

Furthermore, the angular distribution of emission probability at the tissue surface, defined as the ratio of escaped photons along one angle over the total escaped photons per one launched photon was also investigated for all fifteen source depths. As illustrated in Figure 2.6, the probabilities are independent of the source depths. Hence, in the adjoint approach, incident photons could be launched only in the normal direction to the surface.

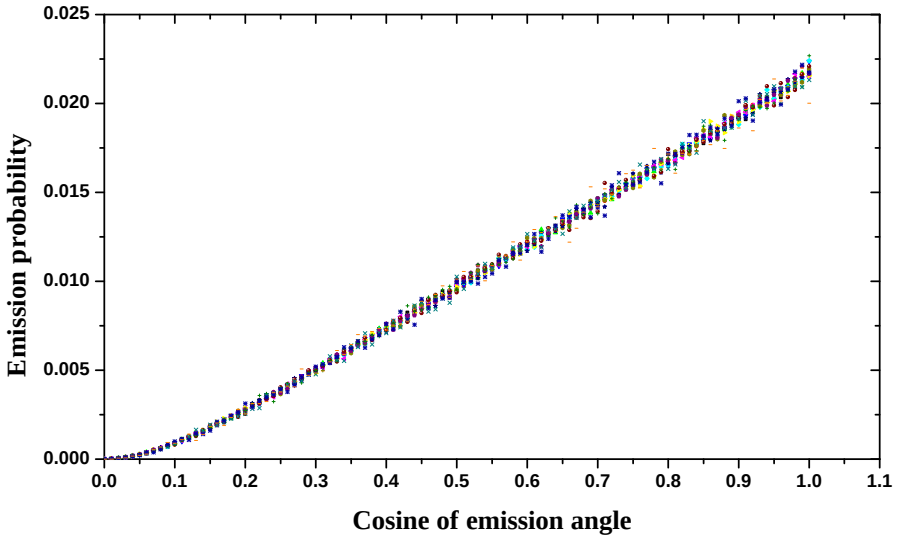

Figure 2.6: The angular distribution of emission probability density. The results of simulations for the fifteen source positions of 1, 2, 3, 4, 5, 6, 8, 10, 12, 14, 16, 18, 20, 22 and 24.95 mm are shown.

2.3.2 Simulation results for $^1O_2$ concentration, fluorescence and SOL emissions

The depth-dependent singlet oxygen concentration, the 705 nm PpIX fluorescence and 1270 nm $^1O_2$ luminescence were simulated using the typical clinical PDT conditions. Total light fluence of 100 J/cm^2 was delivered at irradiance 100 mW/cm^2 at the 633 nm wavelength. The optical properties of skin used in the simulations were shown in Table 2.2. Topical 20% ALA was studied with the incubation time of 4 hours. Hence, the initial concentration of photosensitizer PpIX at the skin surface was assumed as 2.5 μg/g (Star *et al.* 2002), and then had an exponential decay with tissue depth at the rate of 0.8 mm^{-1}. The initial ground state oxygen concentration in tissue was 40 μM. A total of 10,000 photon was simulated in each fluence increment. The second order mechanism was chosen for the simulations. The other parameters for the calculations were listed in Table 2.3. The $^1O_2$ concentrations at the top, middle and bottom of dermis were compared and the mean value of concentration in the dermis layer was also calculated. All the results are shown in Figure 2.7 left panel. From the plot, it can be seen that a rapid reduction of the production rate of $^1O_2$ occurs after about 10 J/cm^2. This may be attributed to the decreased oxygen concentration and the bleaching of PpIX. Below 10 J/cm^2, the curves have shown steeper slopes at shallower depths. This indicates $^1O_2$ production is more efficient at the superficial depth due to higher light fluence when the loss of ground oxygen is not significant. In addition, the volume-averaged $^1O_2$ concentration in the dermis is slightly greater than that at the middle of dermis. The cumulative $^1O_2$ characteristic 1270 nm emission is shown in Figure 2.7 right panel and it demonstrates similar features as the $^1O_2$ concentration curves.

Furthermore, the PpIX fluorescence and 1270 nm luminescence signals reaching the skin surface were obtained. Both were normalized by their initial values and the results are presented in Figure 2.8. The PpIX fluorescence is not a simple exponential decay. The decreasing slope of fluorescence signal indicates that oxygen depletion limits the bleaching in agreement with some clinical studies (Cottrell *et al.* 2008). This fluorescence study result shows that the signal was reduced by 90% after the delivery of 40 J/cm^2 light dose. The 1270 nm luminescence study result shows the rapid reduction of the $^1O_2$ production rate.

Eventually, the relationships of the cumulative $^1O_2$ dose in dermis during PDT with both the time-resolved evolution of fluorescence and cumulative SOL signals were studied and presented in Figure 2.9. The approximate linear relations were observed during most of the PDT treatment in both studies. The conclusion may be helpful in predicting the PDT $^1O_2$ dose in dermis via the detection of emissions.

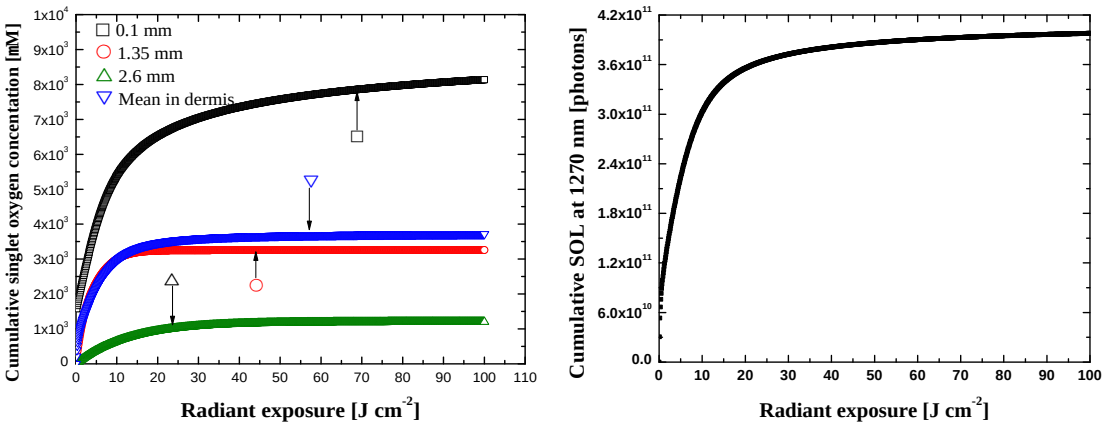

Figure 2.7: The time-resolved instantaneous $^1O_2$ concentrations at various depths (left) and the cumulative 1270 nm SOL (right). The curves in the left panel represent the calculated $^1O_2$ concentrations at the top, middle and bottom of dermis layer, and the volume-averaged concentration in the dermis.

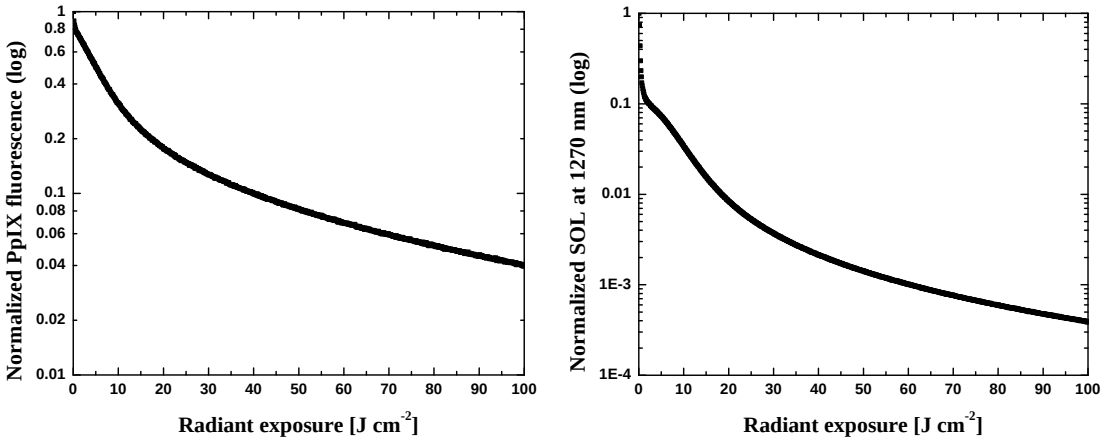

Figure 2.8: The normalized photobleaching fluorescence (left) and 1270 nm $^1O_2$ luminescence (right).

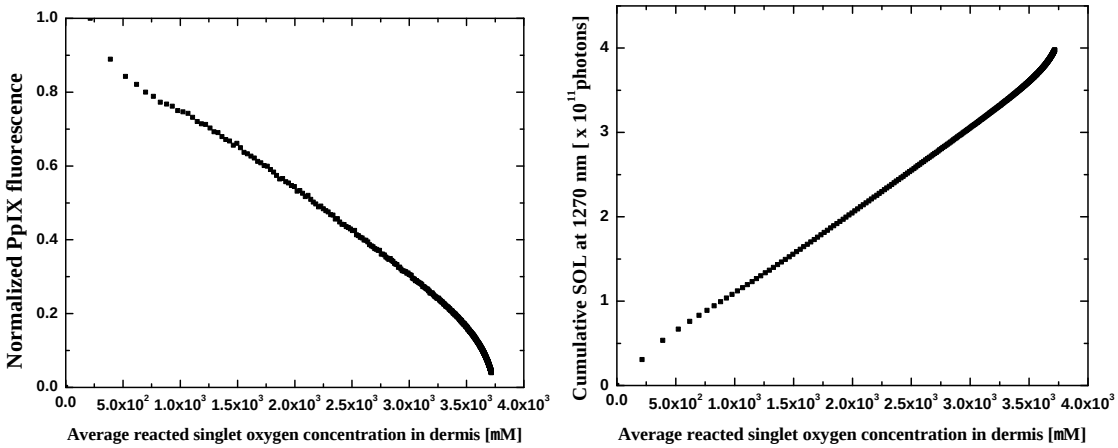

Figure 2.9: The time-resolved relationships of both fluorescence (left) and SOL (right) with $^1O_2$ in dermis.

2.4 Conclusion

A Monte Carlo model for ALA-PDT of human skin was developed. Preliminary results demonstrate the potential of the simulations of photon transport and computation of the time-resolved depth-dependent $^1O_2$ distribution, PpIX fluorescence and $^1O_2$ luminescence. Linear relationships between the $^1O_2$ dose in dermis and the detected emission signals were found, which could be useful tools to interpret the PDT dose deposition via monitoring luminescence emissions. In the near future, this model will be further tested and compared with clinical results. The estimation of simulation parameters will be optimized through the comparisons.

2.5 Appendix

2.5.1 The second order photobleaching mechanism

During the standard photochemical reaction kinetics in the $^1O_2$- and sensitizer triplet-mediated bleaching (SSTB) model (Mitra 2004), the differential equations for the concentrations of ground- and excited- states of the photosensitizer, ground-state oxygen and singlet oxygen are summarized in equations (2.27) to (2.31). Note that a low photosensitizer concentration correction factor δ introduced by Dysart *et al.* (2005) was adopted in this study. The variable notations were defined in Table 2.4.

$$\frac{\mathrm{d}[S_0]}{\mathrm{dt}} = -I_a + k_f[S_1] + k_p[T_1] + k_{ot}[T_1]\left[^3O_2\right] - k_{os}([S_0]+\delta)\left[^1O_2\right] \ , \quad (2.27)$$

$$\frac{\mathrm{d}[S_1]}{\mathrm{dt}} = I_a - k_f[S_1] - k_{isc}[S_1] - k_{sa}[A][S_1] \ , \quad (2.28)$$

$$\frac{\mathrm{d}[T_1]}{\mathrm{dt}} = k_{isc}[S_1] - k_p[T_1] - k_{ot}[T_1]\left[^3O_2\right] - k_{ta}[A][T_1] \ , \quad (2.29)$$

$$\frac{\mathrm{d}\left[^3O_2\right]}{\mathrm{dt}} = -S_\Delta k_{ot}[T_1]\left[^3O_2\right] + k_d\left[^1O_2\right] \ , \quad (2.30)$$

$$\frac{\mathrm{d}\left[^1O_2\right]}{\mathrm{dt}} = S_\Delta k_{ot}[T_1]\left[^3O_2\right] - k_d\left[^1O_2\right] - k_{oa}[A]\left[^1O_2\right] - k_{os}([S_0]+\delta)\left[^1O_2\right] \quad (2.31)$$

Because of the rapid inter-system crossing transition and unlikely reaction between the short lived S_1 and molecular substrate A, the instantaneous concentrations of S_1, T_1 and $^3O_2$ at the semi-equilibrium steady state are expressed by equations (2.32) to (2.34),

$$[S_1] = \frac{I_a}{k_f + k_{isc}} \ , \quad (2.32)$$

$$[T_1] = \frac{k_{isc}[S_1]}{k_p + k_{ot}\left[^3O_2\right] + k_{ta}[A]} \ , \quad (2.33)$$

$$\left[^1O_2\right] = \frac{S_\Delta k_{ot}[T_1]\left[^3O_2\right]}{k_d + k_{oa}[A] + k_{os}([S_0]+\delta)} \ . \quad (2.34)$$

By substitutions and rearrangements of equations (2.27), (2.30), (2.32), (2.33) and (2.34), the reduction rates of S_0 and $^3O_2$ due to PDT were given as equations (2.35)

Table 2.4: Definitions of the notations and variables in the SSTB kinetic model.

Symbol	Definition	Units
$[S_0]$	Ground-state sensitizer	M
$[S_1]$	Singlet excited-state sensitizer	M
$[T_1]$	Triplet excited-state sensitizer	M
$[^3O_2]$	Triplet excited-state oxygen	M
$[^1O_2]$	Singlet excited-state oxygen	M
$[A]$	Molecular substrate	M
k_f	$S_1 \rightarrow S_0$	s^{-1}
k_p	$T_1 \rightarrow S_0$	s^{-1}
k_{isc}	$S_1 \rightarrow T_1$	s^{-1}
k_d	$^1O_2 \rightarrow {}^3O_2$	s^{-1}
k_{ot}	Bimolecular rate constant for reaction of $^3O_2$ with T_1	$M^{-1}s^{-1}$
k_{os}	Bimolecular rate constant for reaction of $^1O_2$ with S_0	$M^{-1}s^{-1}$
k_{oa}	Bimolecular rate constant for reaction of $^1O_2$ with A	$M^{-1}s^{-1}$
k_{sa}	Bimolecular rate constant for reaction of S_1 with A	$M^{-1}s^{-1}$
k_{ta}	Bimolecular rate constant for reaction of T_1 with A	$M^{-1}s^{-1}$
I_a	Photon absorption rate	M s^{-1}
ϕ_t	Sensitizer triplet yield	
S_Δ	Fraction of T_1 and $^3O_2$ reactions that produce $^1O_2$	
σ_{S_0}	Absorption cross section of S_0	cm^2
Φ_D	$^1O_2$ quantum yield	

and (2.36), or in the more explicit forms as equations (2.37) and (2.38).

$$\frac{d[S_0]}{dt} = -k_{ta}[A][T_1] - k_{os}([S_0] + \delta)\left[^1O_2\right] , \tag{2.35}$$

$$\frac{d\left[^3O_2\right]}{dt} = -S_\Delta k_{ot}[T_1]\left[^3O_2\right] + k_d\left[^1O_2\right] , \tag{2.36}$$

$$\frac{\mathrm{d}\left[\mathrm{S}_0\right]}{\mathrm{dt}} = -\phi_{\mathrm{t}} I_{\mathrm{a}} \frac{k_{\mathrm{ta}}\left[\mathrm{A}\right]/k_{\mathrm{ot}}}{k_{\mathrm{p}}/k_{\mathrm{ot}} + k_{\mathrm{ta}}\left[\mathrm{A}\right]/k_{\mathrm{ot}} + \left[^3\mathrm{O}_2\right]} \times \left[1 + \frac{\frac{k_{\mathrm{os}}}{k_{\mathrm{oa}}[\mathrm{A}]}}{k_{\mathrm{ta}}\left[\mathrm{A}\right]/k_{\mathrm{ot}}} \frac{S_\Delta}{\frac{k_{\mathrm{d}}}{k_{\mathrm{oa}}[\mathrm{A}]} + 1} (\left[\mathrm{S}_0\right] + \delta) \left[^3\mathrm{O}_2\right]\right] , \tag{2.37}$$

$$\frac{\mathrm{d}\left[^3\mathrm{O}_2\right]}{\mathrm{dt}} = -S_\Delta I_{\mathrm{a}} \phi_{\mathrm{t}} \frac{1}{\frac{k_{\mathrm{d}}}{k_{\mathrm{oa}}[\mathrm{A}]} + 1} \left[1 + \frac{k_{\mathrm{os}}}{k_{\mathrm{oa}}\left[\mathrm{A}\right]} (\left[\mathrm{S}_0\right] + \delta)\right] \times \frac{\left[^3\mathrm{O}_2\right]}{k_{\mathrm{p}}/k_{\mathrm{ot}} + \frac{k_{\mathrm{ta}}[\mathrm{A}]}{k_{\mathrm{ot}}} + \left[^3\mathrm{O}_2\right]} , \tag{2.38}$$

$$\left[^1\dot{\mathrm{O}}_2\right] = S_\Delta I_{\mathrm{a}} \phi_{\mathrm{t}} \frac{\left[^3\mathrm{O}_2\right]}{k_{\mathrm{p}}/k_{\mathrm{ot}} + \frac{k_{\mathrm{ta}}[\mathrm{A}]}{k_{\mathrm{ot}}} + \left[^3\mathrm{O}_2\right]} , \tag{2.39}$$

where:

$$\phi_{\mathrm{t}} = \frac{k_{\mathrm{isc}}}{k_{\mathrm{f}} + k_{\mathrm{isc}}} , \tag{2.40}$$

$$I_{\mathrm{a}} = \frac{\sigma_{\mathrm{S0}} \dot{\mathrm{F}}_{\mathrm{ex}}}{h\nu} \left[\mathrm{S}_0\right] . \tag{2.41}$$

Acknowledgements

This research was supported by the National Cancer Institute of Canada.

Bibliography

Cottrell, W. J., Paquette, A. D., Keymel, K. R., Foster, T. H., and Oseroff, A. R. (2008). Irradiance-dependent photobleaching and pain in δ-aminolevulinic acid-photodynamic therapy of superficial basal cell carcinomas. *Clin. Cancer Res.*, **14**, 4475–4483.

Crilly, R. J., Cheong, W., Wilson, B., and Spears, J. R. (1997). Forward-adjoint fluorescence model: Monte Carlo integration and experimental validation. *Applied Optics*, **36**, 6513–19.

Dysart, J. S., Singh, G., and Patterson, M. S. (2005). Calculation of singlet oxygen dose from photosensitizer fluorescence and photobleaching during mTHPC photodynamic therapy of MLL cells. *Photochem. Photobiol.*, **81**, 196–205.

Hirano, T. K. E. and Nishiwaki, M. (2002). Detection of near infrared emission from singlet oxygen in PDT with an experimental tumor bearing mouse. *J. Japan. Soc. Laser Surg. Med*, **22**, 99–108.

Hudson, J. A. and Cater, D. B. (1964). An analysis of factors affecting tissue oxygen tension. In *Proc. R. Soc. London*, volume 161 of *B*, pages 247–74. The Royal Society.

Keene, J. P., Kessel, D., Land, E. J., Redmond, R. W., and Truscott, T. G. (1986). Direct detection of singlet oxygen sensitized by Haematoporphyrin and related compounds. *Photochem. and Photobiol.*, **43**, 117–20.

Laubach, H. J., Chang, S. K., Lee, S., Rizvi, I., Zurakowski, D., Davis, S. J., Taylor, C. R., and Hasana, T. (2008). *In-vivo* singlet oxygen dosimetry of clinical 5-aminolevulinic acid photodynamic therapy. *J. Biomed. Opt.*, **13**.

Mitra, S. (2004). *Photodynamic therapy: biophysical mechanisms and molecular responses*. Ph.D. thesis, University of Rochester, Rochester, NY.

Niedre, M., Patterson, M. S., and Wilson, B. C. (2002). Direct near-infrared luminescence detection of singlet oxygen generated by photodynamic therapyin cells *in vitro* and tissues *in vivo*. *Photochem. Photobiol*, **75**, 382–91.

Salomatina, E., Jiang, B., Novak, J., and Yaroslavsky, A. N. (2006). Optical properties of normal and cancerous human skin in the visible and near-infrared spectral range. *J. Biomed. Opt.*, **11**.

Star, W. M., Aalders, M. C. G., Sac, A., and Sterenborg, H. J. C. M. (2002). Quantitative model calculation of the time-dependent protoporphyrin IX concentration in normal human epidermis after delivery of ALA by passive topical application or iontophoresis. *Photochem. Photobiol.*, **75**, 424–32.

Svaasand, L. O., Wyss, P., Wyss, M. T., Tadir, Y., Tromberg, B. J., and Berns, M. W. (1996). Dosimetry model for photodynamic therapy with topically administered photosensitizers. *Laser Surg. Med.*, **18**, 139–49.

Swartling, J., Pifferi, A., Enejder, A. M. K., and Andersson-Engels, S. (2003). Accelerated Monte Carlo models to simulate fluorescence spectra from layered tissues. *J. Opt. Soc. Am. A*, **20**, 714–27.

Wang, K. K., Mitra, S., and Foster, T. H. (2007). A comprehensive mathematical model of microscopic dose deposition in photodynamic therapy. *Med. Phys.*, **34**, 282–93.

Wang, L. V., Nordquist, R. E., and Chen, W. R. (1997). Optimal beam size for light delivery to absorption-enhanced tumors buried in biological tissues and effect of multiple-beam delivery: a Monte Carlo study. *Appl. Optics*, **36**, 8286–91.

Wilson, B. C. and Patterson, M. S. (2008). The physics, biophysics and technology of photodynamic therapy. *Phys. Med. Biol.*, **53**, R61–R109.

Chapter 3

Paper II - A dynamic model for ALA-PDT of skin: simulation of temporal and spatial distributions of ground-state oxygen, photosensitizer and singlet oxygen

Baochang Liu, Thomas J. Farrell and Michael S. Patterson

Department of Medical Physics and Applied Radiation Sciences, McMaster University, 1280 Main Street West, Hamilton, Ontario, Canada, L8S 4K1
and
Department of Medical Physics, Juravinski Cancer Centre, 699 Concession Street, Hamilton, Ontario, Canada, L8V 5C2

Published in Physics in Medicine an Biology, 2010, **55**, 5913-32
Received 18 March 2010, in final form 15 August 2010
Published 16 September 2010
Online at stacks.iop.org/PMB/55/5913
Printed with permission
 [DOI: 10.1088/0031-9155/55/19/019]

Introduction to paper II

The focus of this chapter is on the detailed description of the completed dynamic model of ALA-PDT for normal human skin. With the chosen simulation parameters, the performance of the model was first evaluated by comparing the simulated PpIX fluorescence signals with clinical data from other researchers for normal human skin treated at six different irradiances. Then, the calculated time-resolved depth-dependent distributions of ground-state and singlet-state oxygen, sensitizer, oxygen perfusion are shown in this chapter. Moreover, the calculated emission signals and the influence of oxygen diffusion on the distributions, especially on the singlet oxygen distribution, will be discussed. This chapter also introduced one hypothesis in the model, which was irradiance- and cumulative $^1O_2$-dependent vascular response.

I developed the Monte Carlo (MC) algorithm, designed the graphical user interface (GUI) for the simulation management and performed all the simulations. Drs. Farrell and Patterson provided helpful suggestions and great ideas on the theoretical model development. I analyzed the simulation results, made all the graphical plots and wrote the manuscript. Dr. Patterson supervised my entire work, made great contribution to the results discussion and editing the manuscript.

Contents of Paper II

Abstract

Singlet oxygen ($^1O_2$) direct dosimetry and photosensitizer fluorescence photobleaching are being investigated and applied as dosimetric tools during 5-aminolevulinic acid (ALA) induced protophorphyrin IX (PpIX) photodynamic therapy (PDT) of normal skin and skin cancers. The correlations of photosensitizer fluorescence and singlet oxygen luminescence (SOL) emission signals to $^1O_2$ distribution and cumulative $^1O_2$ dose are difficult to interpret because of the temporal and spatial variations of three essential components (light fluence rate, photosensitizer concentration and oxygen concentration) in PDT. A one dimensional model is proposed in this paper to simulate the dynamic process of ALA-PDT of normal human skin in order to investigate the time-resolved evolution of PpIX, ground-state oxygen ($^3O_2$) and $^1O_2$ distributions. The model incorporates: a simplified three-layer semi-infinite skin tissue, Monte Carlo simulations of excitation light fluence and both PpIX fluorescence and SOL emission signals reaching the skin surface, $^1O_2$-mediated photobleaching mechanism for updating PpIX, $^3O_2$ and $^1O_2$ distributions after the delivery of each light dose increment, ground-state oxygen supply by diffusion from the atmosphere and perfusion from blood vessels, a cumulative $^1O_2$-dependent threshold vascular response, and the initial non-uniform distribution of PpIX. The PpIX fluorescence simulated using this model is compared with clinical data reported by Cottrell *et al.* (2008) for a range of irradiances ($10-150$ mW cm^{-2}). Except for the vascular response, one set of parameters is used to fit data at all irradiances. The time-resolved depth-dependent distributions of PpIX, $^3O_2$ and $^1O_2$ at representative irradiances are presented and discussed in this paper, as well as the PDT-induced vascular response at different depths. Tissue hypoxia and shutdown of oxygen supply occur in the upper dermis, where PpIX is also preserved at the end of treatment.
Keywords: Photodynamic therapy, ALA, PpIX, singlet oxygen, diffusion, perfusion, photobleaching, fluorescence, phosphorescence, luminescence

3.1 Introduction

Photodynamic therapy (PDT) is an emerging treatment modality for a range of malignant and non-malignant conditions. PDT involves the administration of light activatable drugs called photosensitizers followed by exposure to light at a certain wavelength. Ground state molecular oxygen ($^3O_2$) in tissue will then be excited to a singlet state (singlet oxygen, $^1O_2$). Singlet oxygen is considered to be the primary agent causing biological damage in PDT. ALA-PDT is the use of the topically or systemically

administered prodrug 5-aminolevulinic acid (ALA) to generate the photosensitizer protoporphyrin IX (PpIX) endogenously via the heme biosynthetic pathway. Topical ALA-PDT has increasingly been adopted worldwide for the treatment of human skin diseases such as actinic keratoses (AK) and superficial basal cell carcinoma (sBCC).

Unlike the well established dosimetry protocols for therapeutic ionizing radiation, dosimetry for PDT is still under investigation. The current three main approaches are explicit dosimetry, implicit dosimetry and direct dosimetry (Wilson and Patterson 2008). Implicit dosimetry involves measurement of a surrogate for the production of singlet oxygen during PDT. Usually, the photobleaching of the sensitizer is monitored via its fluorescence, and then the $^1O_2$ dose is calculated using the photochemical reaction equations. This approach has been extensively investigated and some preclinical success has been achieved (Dysart *et al.* 2005; Boere *et al.* 2006). Direct dosimetry involves the detection of weak $^1O_2$ phosphorescence at 1270 nm in order to monitor its production. Both approaches are being applied as dosimetric tools during ALA-PDT of normal skin and skin cancer (Cottrell *et al.* 2008; Laubach *et al.* 2008).

However, the relation of both fluorescence and phosphorescence emission signals to singlet oxygen distribution and to cumulative singlet oxygen dose are still not well understood because of the non-uniform distribution and photobleaching of sensitizer, the absorption and scattering properties of skin, and oxygen depletion during PDT. The goal of this project was to develop a model to explore and to understand these relationships. To simulate the dynamic process of ALA-PDT, the model should incorporate accurate light fluence distribution in skin, non-uniform distribution and photobleaching of PpIX, tissue oxygen replenishment and consumption, sensitizer fluorescence and $^1O_2$ 1270 nm phosphorescence emission probabilities, and other possible events such as vascular shutdown.

Several mathematical models of ALA-PDT were recently described. Nielsen *et al.* (2005) developed a model to investigate the effects of oxygen depletion and subsequent hemoglobin deoxygenation on the efficiency of ALA-PDT at different depths. In Nielsen's model, the PDT efficiency was defined as the product of the accurately calculated relative fluence rate in skin and the measured excitation spectrum of PpIX. Another model developed by Wang *et al.* (2007, 2009) incorporated most of the dynamic processes during PDT. The PpIX fluorescence calculated with this model for a range of irradiances could be fitted to clinical photobleaching data by varying one free parameter and by decreasing the blood flow velocity at discrete times during PDT. However, this model does not incorporate any depth dependence of PpIX concentration and light fluence or oxygen diffusion from the skin surface. A recent study by Kruijt *et al.* (2008) on PpIX photobleaching kinetics suggested that the observed changes in the bleaching rate may be caused by the heterogeneous distribution of PpIX.

The one-dimensional model in this paper includes the main photochemical and

physiological reaction mechanisms, but it also takes into account the depth variation of essential quantities. Human skin was simplified as a three-layer semi-infinite tissue. The epidermis, dermis and subcutaneous tissue had independent optical properties with no lateral variation. Any initial depth distribution of PpIX could be specified. Oxygen was supplied by diffusion from the skin surface and perfusion from blood vessels in the dermis and was consumed by PDT and cell metabolism. Oxygen was also allowed to diffuse vertically in the model in response to concentration gradients. PpIX, $^3O_2$ and $^1O_2$ concentrations in each 50 μm thick layer were updated after the delivery of each radiant exposure increment. Finally, both the PpIX fluorescence at 705 nm and the 1270 nm singlet oxygen luminescence reaching the skin surface were calculated at each time step using the adjoint method developed by other researchers (Crilly *et al.* 1997).

Blood flow reduction in human tumors during ALA-PDT has been reported by Herman *et al.* (1999). Wang *et al.* (2009) also found it necessary to include PDT-induced blood flow reduction in order to fit simulated PpIX fluorescence to clinical data. This feature was adopted in the present model, and specifically expressed by the reduction of oxygen supply in each tissue layer. In contrast to the discrete reduction of blood flow velocity at a chosen fluence in Wang's model, the cumulative $^1O_2$-dependent reduction in perfusion rate in this model was a continuous threshold function at every depth, commensurate with a sigmoidal dose response of blood vessels.

Using the present model, PpIX fluorescence during ALA-PDT of normal human skin at irradiances of 10, 20, 40, 50, 60 and 150 mW cm^{-2} was simulated and compared to clinical data to show that the model generates reasonable signals using parameters reported in the literature. Normal human skin, instead of sBCC, was chosen because the anatomy and optical properties are better characterized. The time-resolved evolution of PpIX fluorescence and $^1O_2$ luminescence, and the correlation of these emission signals with $^1O_2$ dose will be reported in a future paper.

3.2 Theory and Method

3.2.1 Normal human skin anatomy and optical properties

Normal human skin consists of several distinct layers. The simplified skin model in this study, illustrated in figure 3.10, consists of three layers: epidermis (100 μm), dermis (2500 μm) and subcutaneous tissue (25000 μm). Absorption and reduced scattering coefficients at the wavelengths of interest were assumed uniform in each layer and are listed in table 3.5. The same refractive index of 1.4 was assumed for all three layers.

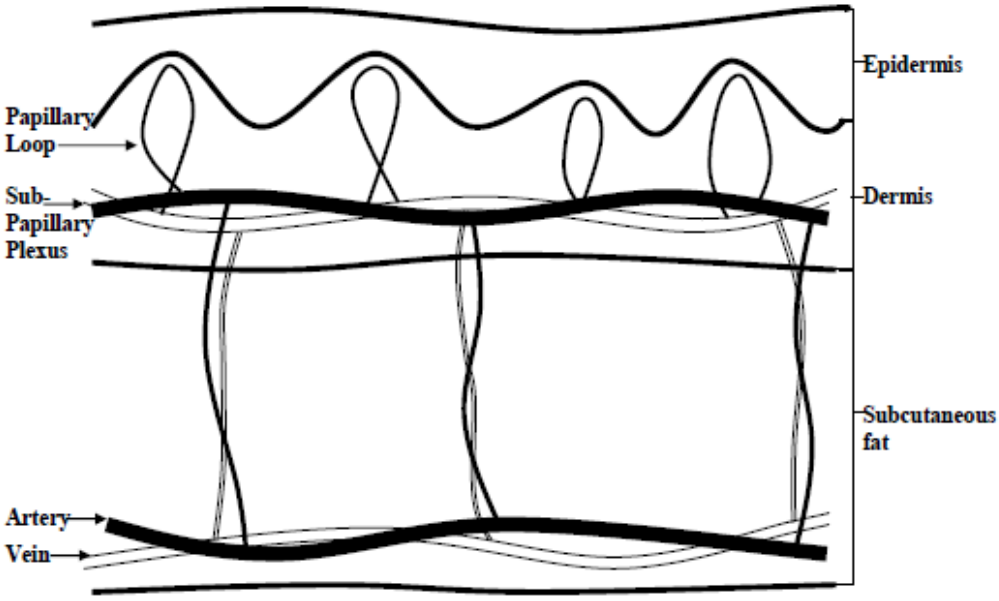

Figure 3.10: Schematics of the anatomical structure of the simplified three-layer normal human skin model with blood vessel distribution.

3.2.2 Monte Carlo simulation of excitation light fluence rate

The Monte Carlo (MC) method is the "gold standard" for modelling light transport in tissue. Detailed information on the MC method can be found in the literature (Wang *et al.* 1995). In this ALA-PDT model, a photon with unit weight was first launched perpendicularly into tissue to simulate a broad beam excitation light source. Because of the different attenuation coefficients in the different skin layers, the delta-scattering technique (Wang *et al.* 1997) was used for this study. Hence, the maximum total attenuation coefficient from the three layers was used to sample the step size (Δs) everywhere. After the photon was moved to its new location, a test was performed to judge whether it was still in the tissue. If the photon escaped from the top surface, the Fresnel reflection equation was used to calculate the internal reflection occurring at the top mismatched boundary, and the reflected photon weight was updated. Prior to scoring and updating the photon weight, a null event, which evaluated the probability of the occurrence of an actual interaction event, had to be sampled for at each interaction location in order to correct the underestimation of Δs introduced by the delta-scattering technique. Photon absorption was scored for depths up to 25 mm. Photons backscattered from beyond this maximum depth were also tracked and scored. A russian roulette procedure was performed to terminate photons with weight less than 10^{-6}.

Table 3.5: Optical properties of normal human skin. Data were extracted from Salomatina *et al.* (2006). The wavelengths of 633, 705 and 1270 nm are the excitation, fluorescence and phosphorescence wavelengths respectively. μ_a : absorption coefficient; μ_s' : reduced scattering coefficient; unit: mm^{-1}.

		633 (nm)		705 (nm)		1270 (nm)	
Tissue	Thickness (mm)	μ_a	μ_s'	μ_a	μ_s'	μ_a	μ_s'
Epidermis	0.1	0.25	5.0	0.25	4.0	0.05	2.5
Dermis	2.5	0.17	2.5	0.15	2.5	0.1	1.6
Sub-Q	25	0.12	2.5	0.12	2.3	0.1	1.5

3.2.3 Oxygen diffusion, consumption and supply in normal human skin

In normal human skin, ground-state oxygen ($^3O_2$) is supplied by two sources: diffusion from the atmosphere and from blood vessels in the dermis (Stücker *et al.* 2002). Both sources were included in this model.

In a one-dimensional molecular diffusion model, the change in the concentration of molecular oxygen at some depth z ($[^3O_2]_z$) with time can be expressed by Fick's second law as shown in equation (3.42), where D is the tissue oxygen diffusion coefficient. This equation can also be rewritten as equation (3.43) to express $[^3O_2]$ at some depth z after a small time interval Δt, where Δz is the depth grid size.

$$\left(\frac{\mathrm{d}\left[^3O_2\right]_z}{\mathrm{d}t}\right) = D\left(\frac{\mathrm{d}^2\left[^3O_2\right]_z}{\mathrm{d}z^2}\right), \tag{3.42}$$

$$\left[^3O_2\right]_{(z,t+\Delta t)} = \left[^3O_2\right]_{(z,t)} + \Delta t \times D \times \frac{\left(\left[^3O_2\right]_{(z-\Delta z,t)} - 2\left[^3O_2\right]_{(z,t)} + \left[^3O_2\right]_{(z+\Delta z,t)}\right)}{(\Delta z)^2}. \tag{3.43}$$

Using Henry's law as expressed in equation (3.44), equation (3.43) can be rewritten as (3.45), where α is the oxygen solubility coefficient and P is the oxygen partial pressure (pO_2).

$$\left[^3O_2\right] = \alpha \times \mathrm{P}, \tag{3.44}$$

$$\alpha \mathrm{P}_{(z,t+\Delta t)} = \alpha \mathrm{P}_{(z,t)} + \Delta t \times D\alpha \frac{\left(\mathrm{P}_{(z-\Delta z,t)} - 2\mathrm{P}_{(z,t)} + \mathrm{P}_{(z+\Delta z,t)}\right)}{(\Delta z)^2}. \tag{3.45}$$

When diffusivity and solubility change with depth, the continuity in pO_2 and the oxygen flux continuity boundary conditions at depth z can be written as equations (3.46) and (3.47), in which the subscripts 'z^-' and 'z^+' denote pO_2 just above and below depth z, D_- and D_+ are the $^3O_2$ diffusion constants above and below z respectively, and α_- and α_+ are the $^3O_2$ solubilities above and below z respectively.

$$P_{z^-} = P_{z^+} , \tag{3.46}$$

$$D_-\alpha_- \left(\frac{dP_{z^-}}{dz}\right) = D_+\alpha_+ \left(\frac{dP_{z^+}}{dz}\right) . \tag{3.47}$$

Rewriting equation (3.45) with the boundary conditions (3.46) and (3.47) leads to equation (3.48), where the depth grid size Δz was 50 μm.

$$\left(\alpha_z \frac{dP_z}{dt}\right)_{\text{diffusion}} = \frac{D_-\alpha_- \left(P_{(z-\Delta z,t)} - P_{(z,t)}\right) - D_+\alpha_+ \left(P_{(z,t)} - P_{(z+\Delta z,t)}\right)}{(\Delta z)^2} . \tag{3.48}$$

The blood supply to the dermis consists mainly of the papillary loops, the horizontal superficial sub-papillary plexus and the deeper cutaneous plexus, as illustrated in figure 3.10. In the simplified perfusion model in this study, oxygen diffuses from a well-oxygenated blood vessel into its surrounding tissue, and the oxygen supply rate at depth z is described by equation (3.49), where K_z is cumulative $^1O_2$ dose-dependent (to be discussed in 3.2.5), and the subscript 'v' denotes the oxygen concentration in the blood vessels.

$$\left(\frac{d\left[^3O_2\right]_z}{dt}\right)_{\text{perfusion}} = K_z \times \left(\left[^3O_2\right]_v - \left[^3O_2\right]_z\right) . \tag{3.49}$$

Note that the difference term in equation (3.49) allows for an increased oxygen supply as $\left[^3O_2\right]_z$ decreases, and approximates the sigmoidal oxygen-hemoglobin dissociation curve (Hill 1910).

Oxygen consumption comprises both metabolic consumption (Γ_{met}) and PDT consumption (Γ_{PDT}). The Michaelis-Menten relationship (Hudson and Cater 1964) expressed in equation (3.50) was used to describe the metabolic consumption. In equation (3.50), $\Gamma_{\text{met}}^{\max}$ is the initial maximum metabolic consumption rate of human skin in the steady state, and k_{50} is the $^3O_2$ concentration at which Γ_{met} is half of $\Gamma_{\text{met}}^{\max}$. The PDT consumption Γ_{PDT} will be described in 3.2.4.

$$\Gamma_{\text{met}} = \Gamma_{\text{met}}^{\max} \frac{[^3O_2]}{k_{50} + [^3O_2]} . \tag{3.50}$$

The rate of change of oxygen concentration at an arbitrary depth z is the sum

of supply, diffusion, metabolic consumption and photochemical PDT consumption at that depth. The initial rate K in equation (3.49) was assumed to be the same at all depths, except zero in the epidermis where there are no blood vessels. Studies have shown that the oxygen demand in the epidermis can be satisfied by atmospheric oxygen (Baumgärtl *et al.* 1987; Stücker *et al.* 2002). The oxygen diffusion constant in the top 50 μm layer representing the stratum corneum was chosen to be approximately an order of magnitude smaller than that in other layers because of lower water content (Vaupel 1976). For simplicity, the oxygen solubility is assumed to be the same in all tissue layers - this assumption is discussed in more detail in section 3.3.

3.2.4 PDT Photobleaching

The differential equations for the concentrations of ground and excited states of the photosensitizer, ground state oxygen and singlet oxygen during PDT are summarized in equations (3.51) to (3.55). The variable notations are defined in table 3.6.

$$\frac{\mathrm{d}\left[\mathrm{S}_0\right]}{\mathrm{d}t} = -I_\mathrm{a} + k_\mathrm{f}\left[\mathrm{S}_1\right] + k_\mathrm{p}\left[\mathrm{T}_1\right] + k_\mathrm{ot}\left[\mathrm{T}_1\right]\left[{}^3\mathrm{O}_2\right] - k_\mathrm{os}\left(\left[\mathrm{S}_0\right] + \delta\right)\left[{}^1\mathrm{O}_2\right] \quad , \tag{3.51}$$

$$\frac{\mathrm{d}\left[\mathrm{S}_1\right]}{\mathrm{d}t} = I_\mathrm{a} - k_\mathrm{f}\left[\mathrm{S}_1\right] - k_\mathrm{isc}\left[\mathrm{S}_1\right] - k_\mathrm{sa}\left[\mathrm{A}\right]\left[\mathrm{S}_1\right] \quad , \tag{3.52}$$

$$\frac{\mathrm{d}\left[\mathrm{T}_1\right]}{\mathrm{d}t} = k_\mathrm{isc}\left[\mathrm{S}_1\right] - k_\mathrm{p}\left[\mathrm{T}_1\right] - k_\mathrm{ot}\left[\mathrm{T}_1\right]\left[{}^3\mathrm{O}_2\right] - k_\mathrm{ta}\left[\mathrm{A}\right]\left[\mathrm{T}_1\right] \quad , \tag{3.53}$$

$$\frac{\mathrm{d}\left[{}^3\mathrm{O}_2\right]}{\mathrm{d}t} = -S_\Delta k_\mathrm{ot}\left[\mathrm{T}_1\right]\left[{}^3\mathrm{O}_2\right] + k_\mathrm{d}\left[{}^1\mathrm{O}_2\right] \quad , \tag{3.54}$$

$$\frac{\mathrm{d}\left[{}^1\mathrm{O}_2\right]}{\mathrm{d}t} = S_\Delta k_\mathrm{ot}\left[\mathrm{T}_1\right]\left[{}^3\mathrm{O}_2\right] - k_\mathrm{d}\left[{}^1\mathrm{O}_2\right] - k_\mathrm{oa}\left[\mathrm{A}\right]\left[{}^1\mathrm{O}_2\right] - k_\mathrm{os}\left(\left[\mathrm{S}_0\right] + \delta\right)\left[{}^1\mathrm{O}_2\right] \quad , \tag{3.55}$$

where :

$$I_\mathrm{a} = \frac{\sigma \dot{F}_\mathrm{ex}}{h\nu}\left[\mathrm{S}_0\right] \quad , \tag{3.56}$$

$\dot{F}_\mathrm{ex}$: energy fluence rate at the excitation wavelength .

The last term in equation (3.51) represents reaction of the ground-state sensitizer with singlet oxygen. The parameter δ accounts for reaction of singlet oxygen with the sensitizer molecule from which energy was transfered to ground state oxygen (Dysart *et al.* 2005). Note that the rate of this photobleaching depends on the oxygen concentration. The last term of equation (3.53) is triplet-mediated photobleaching

Table 3.6: Definitions of the notations and variables in the photobleaching reaction equations.

Symbol	Definition	Units
$[S_0]$	Ground-state sensitizer	M
$[S_1]$	Singlet excited-state sensitizer	M
$[T_1]$	Triplet excited-state sensitizer	M
$[^3O_2]$	Triplet ground-state oxygen	M
$[^1O_2]$	Singlet excited-state oxygen	M
$[A]$	Molecular substrate	M
k_f	$S_1 \rightarrow S_0$	s^{-1}
k_p	$T_1 \rightarrow S_0$	s^{-1}
k_{isc}	$S_1 \rightarrow T_1$	s^{-1}
k_d	$^1O_2 \rightarrow {}^3O_2$	s^{-1}
k_{ot}	Bimolecular rate constant for reaction of $^3O_2$ with T_1	$M^{-1}s^{-1}$
k_{os}	Bimolecular rate constant for reaction of $^1O_2$ with S_0	$M^{-1}s^{-1}$
k_{oa}	Bimolecular rate constant for reaction of $^1O_2$ with A	$M^{-1}s^{-1}$
k_{sa}	Bimolecular rate constant for reaction of S_1 with A	$M^{-1}s^{-1}$
k_{ta}	Bimolecular rate constant for reaction of T_1 with A	$M^{-1}s^{-1}$
I_a	Photon absorption rate	$M\ s^{-1}$
ϕ_t	Sensitizer triplet yield	
S_Δ	Fraction of T_1 and $^3O_2$ reactions that produce $^1O_2$	
σ	Absorption cross section of S_0	cm^2
Φ_D	$^1O_2$ quantum yield	

independent of singlet oxygen. This second mechanism was observed for Photofrin by Finlay *et al.* (2004), and has been included here for generality. Bleaching of PpIX under hypoxia was observed *in vitro* by Dysart and Patterson (2006), but the mechanism has not been identified. As will be shown below, the clinical photobleaching data can be explained without including this second mechanism.

With the above differential equations, the rates of change of $[S_0]$ and $[^3O_2]$ due to PDT can be derived in the quasi-steady state as equations (3.57) and (3.58). In the quasi-steady state, the short lifetimes of S_1, T_1 and $^1O_2$ compared to the time for bulk variations of sensitizer and oxygen concentrations allow their instantaneous concentrations to be in dynamic equilibrium. These instantaneous concentrations can be found by setting their time derivatives in equations (3.52), (3.53) and (3.55) to zero (Finlay *et al.* 2004). Given that, equations (3.57) and (3.58) can be derived and then rewritten in the more explicit forms as equations (3.59) and (3.60). The details of derivation can be found elsewhere (Liu *et al.* 2009).

$$\frac{\mathrm{d}\left[\mathrm{S_0}\right]}{\mathrm{d}t} = -k_{\mathrm{ta}}\left[\mathrm{A}\right]\left[\mathrm{T_1}\right] - k_{\mathrm{os}}\left(\left[\mathrm{S_0}\right]+\delta\right)\left[^1\mathrm{O_2}\right] \ , \tag{3.57}$$

$$\frac{\mathrm{d}\left[^3\mathrm{O_2}\right]}{\mathrm{d}t} = -S_\Delta k_{\mathrm{ot}}\left[\mathrm{T_1}\right]\left[^3\mathrm{O_2}\right] + k_{\mathrm{d}}\left[^1\mathrm{O_2}\right] \ . \tag{3.58}$$

$$\begin{aligned}\frac{\mathrm{d}\left[\mathrm{S_0}\right]}{\mathrm{d}t} &= -\phi_{\mathrm{t}} I_{\mathrm{a}} \frac{k_{\mathrm{ta}}\left[\mathrm{A}\right]/k_{\mathrm{ot}}}{k_{\mathrm{p}}/k_{\mathrm{ot}} + k_{\mathrm{ta}}\left[\mathrm{A}\right]/k_{\mathrm{ot}} + \left[^3\mathrm{O_2}\right]} \\ &\quad \times \left[1 + \frac{\frac{k_{\mathrm{os}}}{k_{\mathrm{oa}}[\mathrm{A}]}}{k_{\mathrm{ta}}\left[\mathrm{A}\right]/k_{\mathrm{ot}}} \frac{S_\Delta}{\frac{k_{\mathrm{d}}}{k_{\mathrm{oa}}[\mathrm{A}]}+1}\left(\left[\mathrm{S_0}\right]+\delta\right)\left[^3\mathrm{O_2}\right]\right] \ , \end{aligned} \tag{3.59}$$

$$\begin{aligned}\frac{\mathrm{d}\left[^3\mathrm{O_2}\right]}{\mathrm{d}t} &= -S_\Delta I_{\mathrm{a}} \phi_{\mathrm{t}} \frac{1}{\frac{k_{\mathrm{d}}}{k_{\mathrm{oa}}[\mathrm{A}]}+1}\left[1 + \frac{k_{\mathrm{os}}}{k_{\mathrm{oa}}\left[\mathrm{A}\right]}\left(\left[\mathrm{S_0}\right]+\delta\right)\right] \\ &\quad \times \frac{\left[^3\mathrm{O_2}\right]}{k_{\mathrm{p}}/k_{\mathrm{ot}} + \frac{k_{\mathrm{ta}}[\mathrm{A}]}{k_{\mathrm{ot}}} + \left[^3\mathrm{O_2}\right]} \ , \end{aligned} \tag{3.60}$$

where :

$$\phi_{\mathrm{t}} = \frac{k_{\mathrm{isc}}}{k_{\mathrm{f}} + k_{\mathrm{isc}}} \ . \tag{3.61}$$

Due to the lack of explicit values for the ratio $k_{\mathrm{d}}/\left(k_{\mathrm{oa}}\left[A\right]\right)$ in the literature, β'_{PDT} is defined as equation (3.62). For a given sensitizer concentration, the product $\beta'_{\mathrm{PDT}}\left[\mathrm{S_0}\right]$ is equal to the ratio of initial maximal PDT oxygen consumption rate to excitation fluence rate, and it can be measured *in vitro*.

$$\beta'_{\mathrm{PDT}} = S_\Delta \phi_{\mathrm{t}} \frac{\sigma}{h\nu} \frac{1}{\frac{k_{\mathrm{d}}}{k_{\mathrm{oa}}[\mathrm{A}]}+1} \ . \tag{3.62}$$

The final differential equation for updating ground state oxygen ($^3\mathrm{O_2}$) concentration at each depth should include the diffusion term in equation (3.48), the oxygen supply in equation (3.49), the metabolic consumption (Γ_{met}) in equation (3.50), and the PDT consumption (Γ_{PDT}) in equation (3.60). Oxygen concentration can also be expressed in terms of the oxygen partial pressure P using Henry's law shown in equation (3.44). The two coupled differential equations shown in (3.63) and (3.64) were used to update the concentrations of ground-state PpIX and oxygen partial pressure at each depth after each time step Δt during PDT. Once oxygen pressure is updated,

oxygen concentration can be calculated using Henry's law.

$$\begin{aligned}\frac{\mathrm{d}\left[\mathrm{S}_0\right]_z}{\mathrm{d}t} &= -\dot{F}_{\mathrm{ex}}\left[\mathrm{S}_0\right]_z \frac{k_{\mathrm{ta}}\left[\mathrm{A}\right]/k_{\mathrm{ot}}}{k_{\mathrm{p}}/k_{\mathrm{ot}} + k_{\mathrm{ta}}\left[\mathrm{A}\right]/k_{\mathrm{ot}} + \alpha_z \mathrm{P}_z} \\ &\quad \times \left[\phi_{\mathrm{t}}\frac{\sigma}{h\nu} + \frac{\frac{k_{\mathrm{os}}}{k_{\mathrm{oa}}\left[\mathrm{A}\right]}}{k_{\mathrm{ta}}\left[\mathrm{A}\right]/k_{\mathrm{ot}}}\beta'_{\mathrm{PDT}}\left(\left[\mathrm{S}_0\right]_z + \delta\right)\alpha_z \mathrm{P}_z\right] , \qquad (3.63)\\ \alpha_z\frac{\mathrm{dP}_z}{\mathrm{d}t} &= -\dot{F}_{\mathrm{ex}}\left[\mathrm{S}_0\right]_z \beta'_{\mathrm{PDT}}\left[1 + \frac{k_{\mathrm{os}}}{k_{\mathrm{oa}}\left[\mathrm{A}\right]}\left(\left[\mathrm{S}_0\right]_z + \delta\right)\right]\frac{\alpha_z \mathrm{P}_z}{k_{\mathrm{p}}/k_{\mathrm{ot}} + \frac{k_{\mathrm{ta}}[\mathrm{A}]}{k_{\mathrm{ot}}} + \alpha_z \mathrm{P}_z} \\ &\quad -\Gamma^{\max}_{\mathrm{met}}\frac{\alpha_z \mathrm{P}_z}{k_{50} + \alpha_z \mathrm{P}_z} + K_z\left(\left[{}^3\mathrm{O}_2\right]_{\mathrm{v}} - \alpha_z \mathrm{P}_z\right) \\ &\quad + \frac{D_-\alpha_-\left(\mathrm{P}_{z-\Delta z} - \mathrm{P}_z\right) - D_+\alpha_+\left(\mathrm{P}_z - \mathrm{P}_{z+\Delta z}\right)}{\left(\Delta z\right)^2} . \qquad (3.64)\end{aligned}$$

By solving differential equations (3.51) to (3.55) in the quasi-steady state (Liu *et al.* 2009), the instantaneous production rate of $^1\mathrm{O}_2$ at each depth can be obtained and is shown in equation (3.65). The cumulative singlet oxygen "dose" can be obtained via time integration of equation (3.65).

$$\left[{}^1\dot{\mathrm{O}}_2\right] = I_{\mathrm{a}}\Phi_{\mathrm{D}}\frac{\left[{}^3\mathrm{O}_2\right]}{k_{\mathrm{p}}/k_{\mathrm{ot}} + \frac{k_{\mathrm{ta}}[\mathrm{A}]}{k_{\mathrm{ot}}} + \left[{}^3\mathrm{O}_2\right]} . \qquad (3.65)$$

3.2.5 Response of vasculature to singlet oxygen dose

The physiological response of blood flow reduction during ALA-PDT has been controversial, but it was observed in human tumor using a laser Doppler method (Herman *et al.* 1999) and employed in a theoretical model of human skin (Wang *et al.* 2009) to explain clinical photobleaching data. This response is included in this model by decreasing the oxygen supply parameter K in equation (3.49), commensurate with damage to blood vessels. As singlet oxygen is considered the primary vehicle for biological damage during PDT, the perfusion rate reduction should be correlated to the cumulative $^1\mathrm{O}_2$ dose. Adopting the idea of a threshold sigmoid-shape dose response curve from radiation therapy, a curve such as that demonstrated in figure 3.11, was hypothesized for the oxygen perfusion response.

The relation is expressed in equation (3.66), where D_{50} is the $^1\mathrm{O}_2$ dose required to reduce K to half of its initial value and a is the slope of the sigmoid function. The initial K_0 values were calculated so that the initial oxygen supply rate was equal to the metabolic consumption rate at 40 μM tissue oxygen concentration. The perfusion rate at each depth was updated for the delivery of each radiant exposure increment via equation (3.66).

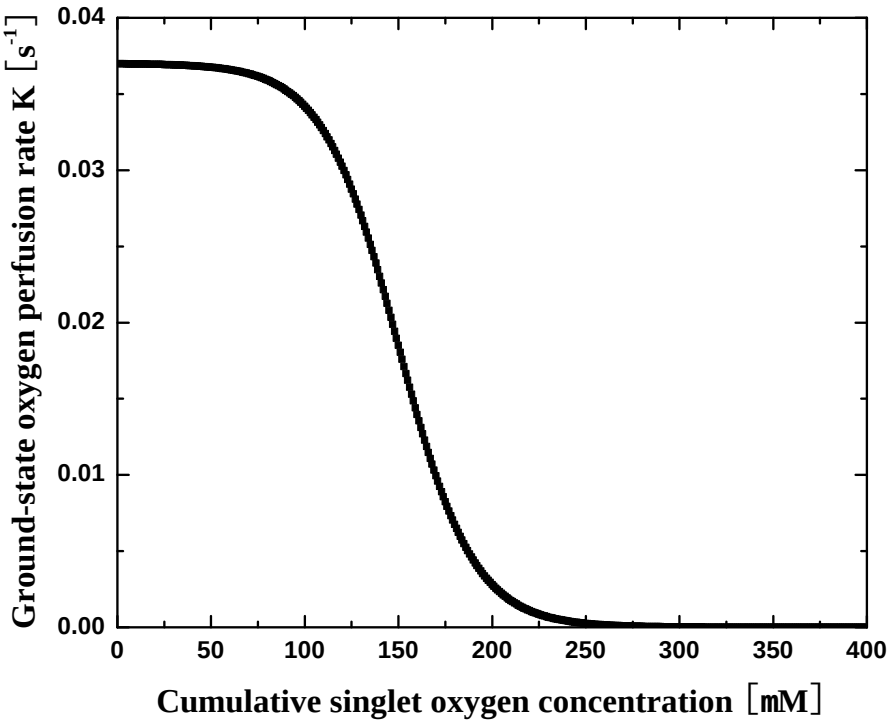

Figure 3.11: Example of the singlet oxygen-dependent vascular response curve used in the model.

$$K_z(t) = K_0 \left(1 - \frac{1}{1 + \mathrm{e}^{-a\left(\int_0^t [^1\dot{\mathrm{O}}_2]_z(t')\mathrm{d}t' - D_{50}\right)}}\right) . \tag{3.66}$$

Note that the vascular oxygen supply to each layer depends only upon the singlet oxygen dose to that layer. This assumes that each layer has its own "independent" blood supply. Clearly this is an simplification as capillary loops transport blood vertically in the dermis. However, these deeper layers will, generally, receive lower singlet oxygen doses, so it is not unreasonable to assume that flow reductions will occur first in layers with the highest singlet oxygen doses.

3.2.6 Calculation of the emission signals

Fluorescence and $^1O_2$ phosphorescence reaching the surface were calculated using the adjoint (reverse) (Crilly *et al.* 1997) Monte Carlo method because of its efficiency compared to the standard (forward) method. This reverse method is to backtrack an emission photon from the tissue surface to its origin. Thus, the previous MC code

for light fluence can also be applied to simulate emission light using an appropriate scaling factor (C_r). The adjoint scaling factor C_r was defined as the ratio of the relative emission (i.e. emittance divided by source power) from an isotropic point source at depth z to the relative fluence (i.e. fluence divided by radiant exposure) at the same depth from a broad beam source at the surface. Several assumptions for using C_r were tested and applied. These assumptions included its independence of the optical properties of tissue for the same index of refraction, depth-independent angular emission probability distribution, and no significant effect of photosensitizer absorption on emission photon propagation. The verification of these assumptions and the derivation of C_r were described in more detail elsewhere (Liu *et al.* 2009).

Using C_r, both the sensitizer fluorescence at 705 nm and the singlet oxygen luminescence at 1270 nm can be computed via equations (3.67) and (3.68).

$$\dot{\mathrm{E}}_{\mathrm{m705}} = \int_0^\infty \dot{F}_{\mathrm{ex}}(z)\mu_{a,\mathrm{d}}(z)\phi_\mathrm{f}F_{\mathrm{em}_{705}}(z)C_\mathrm{r}\mathrm{d}z\ , \tag{3.67}$$

$$\dot{\mathrm{E}}_{\mathrm{m1270}} = \int_0^\infty [^1\dot{\mathrm{O}}_2](z)\phi_\mathrm{d}F_{\mathrm{em}_{1270}}(z)C_\mathrm{r}\mathrm{d}z\ , \tag{3.68}$$

where $\dot{F}_{\mathrm{ex}}(z)$ and $F_{\mathrm{em}}(z)$ are the fluence rate and relative fluence at the excitation and corresponding emission wavelengths respectively; $\mu_{a,\mathrm{d}}(z)$ is the absorption coefficient of photosensitizer; ϕ_f, ϕ_d are the fluorescence and phosphorescence quantum yields. The cumulative quantities were obtained via time integration.

3.2.7 Determination of simulation parameters and execution of simulations

Typical clinical conditions for ALA-PDT of human skin as described by Cottrell *et al.* (2008) were considered in this study. ALA (concentration 20%) was topically administered for a 4-h incubation period. The skin was then exposed to irradiation at 633 nm at irradiances 10, 20, 40, 50, 60 and 150 mW/cm^2 and a total light dose (i.e. radiant exposure) of 200 J/cm^2 was delivered. For treatments with irradiances other than 150 mW/cm^2, the irradiance was increased to 150 mW/cm^2 after 90% of the initial PpIX was bleached (Cottrell *et al.* 2008). An initial exponential distribution of PpIX with depth was assumed, and the PpIX concentration on the skin surface was 4.4 μM (Star *et al.* 2002). An exponential decay constant of 0.8 mm^{-1} was chosen so that the ratio of PpIX concentration at 0.2 mm to that on the surface was about 85%, consistent with other results (Star *et al.* 2002). An empirical value of 0.114 for the adjoint scaling factor C_r was derived and reported earlier (Liu *et al.* 2009), and was used for all the simulations in this study. In steady state prior to PDT in normal skin tissue, the oxygen demand by metabolic consumption should be satisfied

by the oxygen supply at all depths. Simulation of this equilibrium process (running the model without PDT oxygen consumption) produced the initial $^3O_2$ and oxygen partial pressure distributions for the ALA-PDT simulations. Ground-state oxygen concentration inside blood vessels was assumed constant (80 μM) during PDT. The oxygen partial pressure in air is 160 mmHg and the oxygen solubility (α) in all tissue layers was assumed equal to that in water at 37 °C, i.e. 1.25 μM mmHg^{-1}.

Most of the photophysical and physiological parameters listed in table 3.7 have been investigated for the sensitizers mTHPC and Photofrin, and these studies were mostly performed on a multi-cell spheroid model. (Mitra and Foster 2005) Some parameters were also investigated for ALA in cells, however few of them have been measured for ALA-PDT of human skin. Using literature values for ALA or other sensitizers in the spheroid model as an initial guide, some parameters were manually modified within literature ranges to fit the simulated PpIX fluorescence results to the clinical data of Cottrell *et al.* (2008). The modified parameters are indicated by asterisks in table 3.7. As noted above, the triplet bleaching coefficient ($k_{ta}[A]/k_{ot}$) was set to zero as the clinical data were found to be consistent with singlet oxygen mediated PpIX photobleaching. The reduced chi-squared (χ^2_v) of the fit using final choices of parameters was calculated for each irradiance.

To execute simulations, the relative fluence at the emission wavelengths (F_{em}) was simulated using 10^6 launched photons before the main program began. It was assumed that the results were not affected by the changing $^3O_2$ concentration and hemoglobin oxygenation during PDT, so they could be used to calculate the emission signals in equations (3.67) and (3.68). The main program began with MC fluence rate simulation at the clinical excitation wavelength 633 nm. The optical properties of skin in table 3.5 along with PpIX absorption at 633 nm were used for all MC simulations. The coupled differential equations (3.63) and (3.64) with the parameters in table 3.7 were computed simultaneously after MC simulation for each radiant exposure increment (equal to the product of the irradiance and time increment, 1 second). The concentrations of $^3O_2$ and PpIX at each depth were then updated, and the $^1O_2$ production and emission signals at both 705 nm and 1270 nm wavelengths were computed via equations (3.65), (3.67) and (3.68). Meanwhile, the oxygen perfusion supply rate K was also updated using equation (3.66) once the updated $^1O_2$ concentration was obtained.

This iterative computation enabled calculation of the time-resolved evolution of depth-dependent distributions of PpIX, $^1O_2$ and $^3O_2$, and both PpIX fluorescence and $^1O_2$ luminescence reaching the skin surface. The execution of the simulations and the calculations were managed by a Graphical User Interface (GUI) created using Matlab 7.5.0.

In addition, the GUI automatically determines the number of photons to be launched to achieve a specified relative standard error in fluence rate at a given

Table 3.7: Photophysical and physiological parameters. D_{50} values correspond to 10, 20, 40, 50, 60 and 150 mW cm^{-2}. The same D_{50} values were found for both 20 and 40 mW cm^{-2}, and for both 50 and 60 mW cm^{-2}. D=0.2×10^{-5} cm^{2}s^{-1} was used only in the top 50 μm stratum corneum layer, and D=1.25 ×10^{-5} cm^{2}s^{-1} was used for other layers.

Parameters	Values (Published data)	Reference	Units
$(k_{os}/k_{oa}\,[A])$	90	Georgakoudi and Foster (1998)	M^{-1}
$(k_p/k_{ot})^*$	4±2 (5.8-11.6: mTHPC)	Mitra and Foster (2005)	μM
$(k_{ta}\,[A]\,/k_{ot})$	0		μM
$(\Gamma_{met}^{max})^*$	1.5±0.3 (1-1.56)	Stücker *et al.* (2002)	μM s^{-1}
δ^*	128±20 (33-330: mTHPC)	Dysart *et al.* (2005)	μM
k_{50}	0.5	Wang *et al.* (2007)	μM
K_0	0.0370		s^{-1}
$[^3O_2]_v$	80		μM
a	0.08		μM^{-1}
D_{50}	126/191/155/108		μM
D^*	0.2/1.25±0.05(1-1.5)×10^{-5}	Wang (2005)	cm^{2}s^{-1}
α	1.25×10^{-6}		M mmHg^{-1}
ϵ_{PpIX}	3000		M^{-1}cm^{-1}
β'_{PDT}	0.021		mJ^{-1}cm^2
ϕ_f	0.05		
ϕ_d	10^{-8}		
ϕ_t	0.83	Josefsen and Boyle (2008)	
Φ_D	0.57	Keene *et al.* (1986)	

* The parameters were based on the published values, but then modified to achieve the best fits to the clinical data in figure 3.12. The uncertainties are estimated from the quality of the fits.

depth. This is beneficial for simulating the entire PDT treatment course because the MC code is run for every radiant exposure increment. In this work, the maximum allowable relative error was chosen as 1% at the bottom of dermis (2600 μm). The number of photons launched at the excitation wavelength was in the range of 100,000 to 200,000 to satisfy this condition for every exposure increment. Typical execution time for a simulated treatment was about one day on a personal computer with 2.0 GHz CPU.

3.3 Results and Discussion

In this section, the calculated PpIX fluorescence photobleaching is compared with an extensive clinical data set published by Cottrell *et al.* (2008). Then, the depth-resolved distributions of PpIX, $^3O_2$, and cumulative $^1O_2$ as PDT treatment progresses, as well as the changes in vascular oxygen supply that are necessary to fit the clinical data, are examined in detail.

Figure 3.12 shows the relative PpIX fluorescence reaching the skin surface versus radiant exposure for six different irradiances. The hollow squares and standard deviations are taken directly from figures 2, 5 and 6 of Wang *et al.* (2009), the bottom curves in each panel are the best fits of our model to the early time points with no change in vascular oxygen supply, and the top curves are the fits to all the data using the same parameters but also incorporating a singlet oxygen-dependent vascular response as described in the section 3.2.3. To avoid confusion the abscissa has been labelled "radiant exposure" which is the product of irradiance and time. Cottrell *et al* used the label "fluence", but the actual fluence in tissue would be greater than the radiant exposure at the surface and would decrease with depth.

Considering first the calculations represented by the bottom curves in each panel, the reduced chi-squared (χ_v^2) for all the data from 0 to about 2 J cm^{-2} (22 points in total) is 3.39. This exceeds Bevington's (Bevington and Robinson 1992) criterion that χ_v^2 should be less than about 1.5 for a reasonable fit. However, examination of figure 3.12 shows that the data for 60 mW cm^{-2} contribute most to χ_v^2. Eliminating just the first two points at this irradiance reduces χ_v^2 to 1.54. Only the parameters marked by asterisks in table 3.7 have been adjusted to achieve the fit and, except for k_p/k_{ot} these are still within the range of results published by other researchers. Although there are four free parameters, the range that gives an acceptable fit (see table 3.7) is relatively small. The simulations take so long that it is not practical to perform an exhaustive search of the χ_v^2 space for a global minimum.

No combination of parameters provided a reasonable fit at higher radiant exposure unless the vascular oxygen supply was reduced. The hypothesis that a universal singlet oxygen dose response of the blood vessels would explain the observations was tested, but significantly better fits were obtained by allowing D_{50} to depend on the irradiance as shown in figure 3.13(a). This parameter ranged from 108 to 191 μM but did not change monotonically with irradiance. The reduced chi-squared for the fits to the data for 10, 20, 40, 50, 60, 150 mW cm^{-2} were 0.31, 0.94, 1.05, 0.23, 3.64 and 0.76 respectively. As above, the early time points for 60 mW cm^{-2} appear to be outliers. If the first two are eliminated, $\chi_v^2 = 1.15$ for this data set. The clinical data were also analyzed by Wang *et al.* (2009) using their PDT model, which does not include depth dependence of any quantity. They obtained good fits to the early time points although the values they used for β_{PDT} (the ratio of initial oxygen consumption

rate to fluence rate) were an order of magnitude higher than expected from published photophysical data for PpIX. They also allowed β_{PDT} to vary with irradiance although it should be independent of this parameter. Wang *et al* fit the higher radiant exposure data by reducing the vascular oxygen supply at discrete time points. The data for each irradiance were treated separately. On figure 3.12 the vertical lines indicate the radiant exposure at which Wang *et al* introduced the first reduction. In general, these are comparable to the values at which the top and bottom curves in the present model diverge.

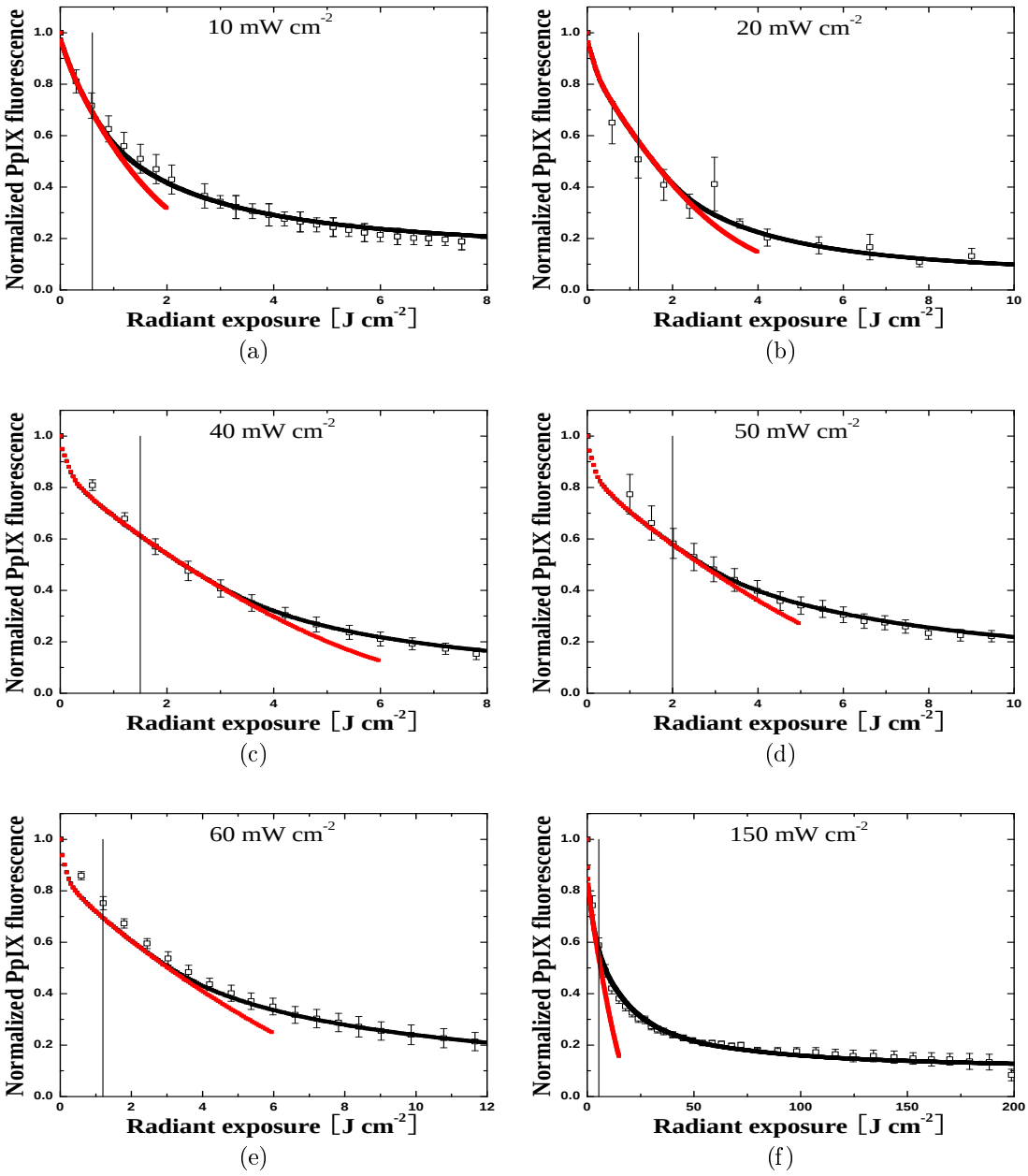

Figure 3.12: The simulated normalized PpIX fluorescence fitted to the clinical data for normal human skin reported by Cottrell *et al.* (2008). Clinical data are denoted as hollow squares. The straight lines indicate the radiant exposure (product of irradiance and time) for the first reduction of blood flow velocity in Wang's model (Wang *et al.* 2009). The bottom curves in each panel are the fits using the same parameters as the top curves but without the oxygen supply reduction.

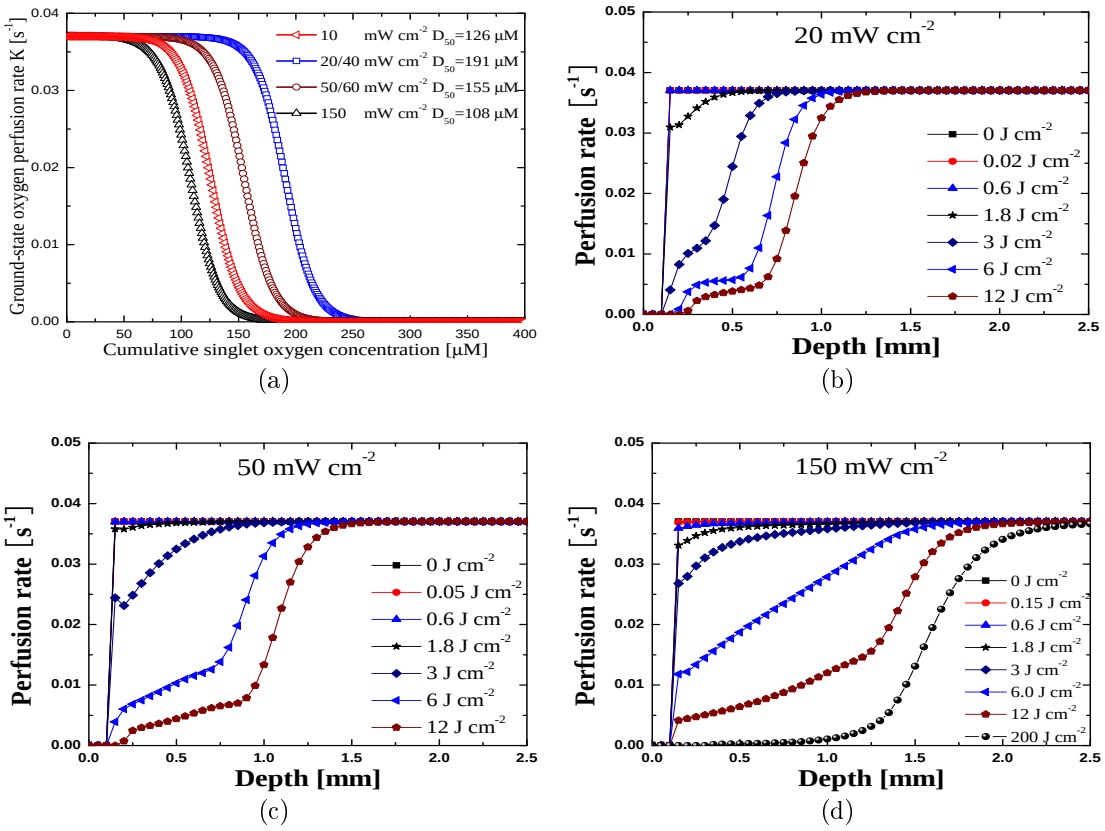

Figure 3.13: The cumulative singlet oxygen-dependent vascular response curve and depth-resolved distribution of oxygen perfusion supply.

Before discussing the depth distributions of PpIX, $^3O_2$, and cumulative $^1O_2$ it should be noted that the details of these, as well as the vascular response in figure 3.13(a), are dependent on the optical properties of the skin and the PpIX concentration and distribution that are used in the model. However, these quantities have been varied over realistic ranges (data not shown) and the general features of the distributions discussed below are robust.

Figure 3.13(a) shows the vascular response (i.e. K versus cumulative $^1O_2$) discussed above and figures 3.13(b), 3.13(c) and 3.13(d) show K versus depth as delivered radiant exposure increases at representative irradiances of 20, 50, and 150 mW cm^{-2} respectively. A singlet oxygen response where K decreases linearly with dose to zero was also investigated but this response did not give good fits to the clinical fluorescence data. Figure 3.13 shows that the vascular oxygen supply to the upper dermis is reduced to less than 10 percent of the initial value within the first three

minutes of treatment. This region of reduced supply slowly extends to greater depths, spreading to about 1.5 mm at the end of the 200 J cm^{-2} treatment. Of course, the data analyzed here do not give any indication whether this reduction is reversible after irradiation.

Figures 3.14(a), 3.14(c), 3.14(e) show the evolution of the $^3O_2$ distribution during PDT at the same irradiances as figure 3.13, and figures 3.14(b), 3.14(d), 3.14(f) are the corresponding distributions of PpIX. The initial oxygen concentration is 40 μM in the deep dermis and is achieved by a balance between metabolic consumption and vascular supply. The concentration in the epidermis and upper dermis is higher because of the diffusion of oxygen from the skin surface. Within a few seconds of the start of PDT the oxygen concentration is reduced to close to zero in the upper dermis. Slightly higher values are maintained in the epidermis by diffusion. This hypoxic region spreads deeper into the dermis as treatment progresses as a result of PDT consumption and reduction in blood perfusion. The oxygen concentration near the surface actually starts to increase as PpIX is bleached and diffusion from the surface exceeds the PDT consumption. Because PpIX photobleaching is assumed to be mediated by singlet oxygen, the oxygen distribution has a profound effect on the PpIX concentration. As seen in figure 3.14, PpIX near the surface is rapidly bleached regardless of the irradiance. In the deep dermis, bleaching also takes place as the vessels are still able to deliver the necessary oxygen to maintain PDT. At intermediate depths where hypoxia develops, there is a "reservoir" of PpIX that contributes most of the observed fluorescence and is responsible for the very slow bleaching later in the treatment seen in, for example, figure 3.12(f).

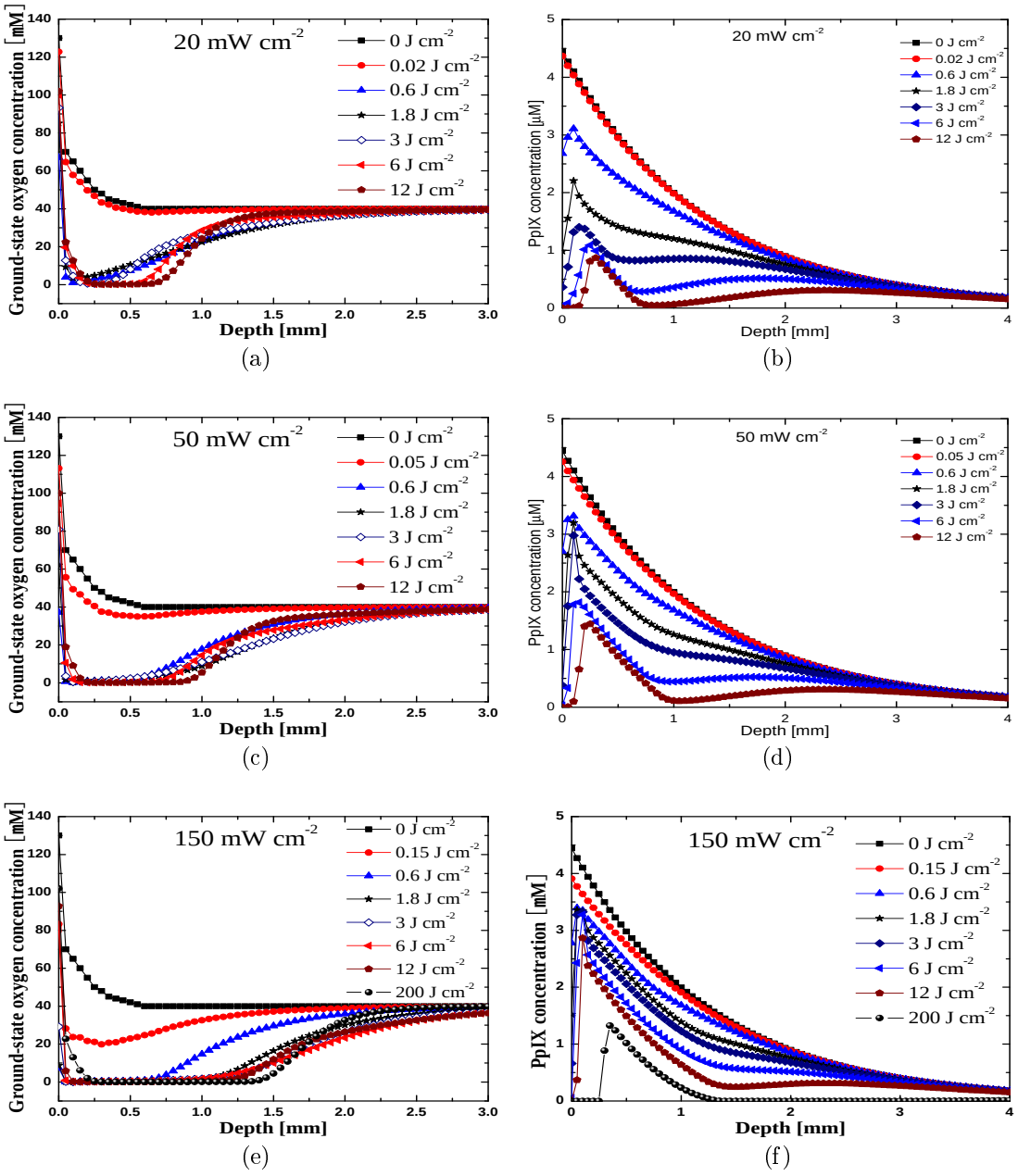

Figure 3.14: Depth-resolved distributions of ground state oxygen and PpIX.

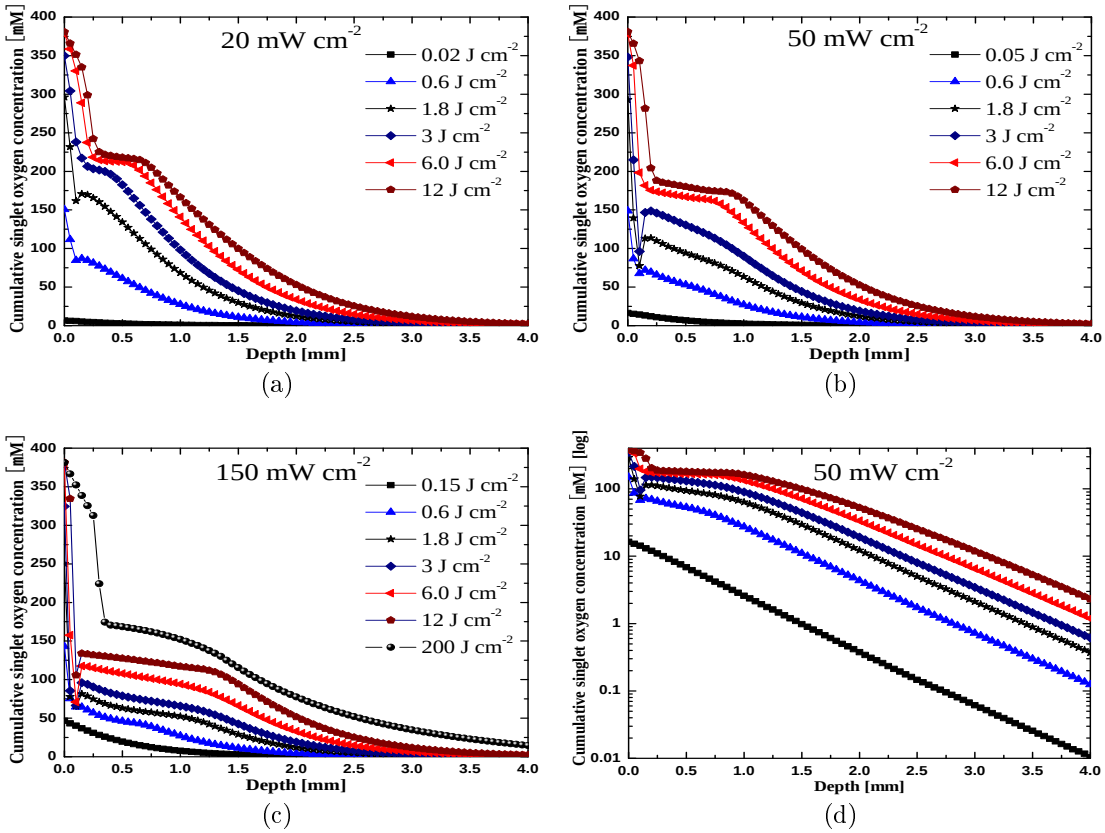

Figure 3.15: Depth-resolved distribution of cumulative singlet oxygen. (d) shows the same data as (b) on a logarithmic scale to better illustrate the behavior at depths beyond 1 mm.

In figure 3.15 the total amount of singlet oxygen produced during the PDT treatment is plotted as a function of depth for the three representative irradiances. The maximum "dose" is delivered to the skin surface as initial PpIX concentration is the highest there and, as shown in figure 3.14, the PDT process is never oxygen-limited. As all of the PpIX at the surface is eventually photobleached, the $^1O_2$ dose is determined solely by the initial photosensitizer concentration and is independent of irradiance. The value, 380 μM, is probably an underestimate as the current model has not included potential contributions to the singlet oxygen dose from photoproducts of PpIX which are known to be photosensitizers as well (Dysart and Patterson 2006). Not much is known about the singlet oxygen dose required for specific biological effects *in vivo*, although it has been estimated that doses of a few mM are enough to cause tissue necrosis (Farrell *et al.* 1998). A recent report by Wang *et al.* (2010) suggests this value may be less than 1 mM.

The singlet oxygen dose below the surface is a complex function of the history of the local fluence rate, PpIX and $^3O_2$ concentrations, as well as the response of the tissue vasculature. Once all of the PpIX has been bleached at a specific depth or the oxygen supply has been eliminated, the dose cannot increase at this depth regardless of the light administered. Hence, in figure 3.15, two regions can be identified: one where the singlet oxygen dose approaches a "plateau" (e.g. 0.2 to 1.0 mm in figure 3.15(b)) and a deeper region where the dose will continue to increase as more light is delivered.

In the present model the fluence distribution is recalculated after the delivery of each treatment light increment but the only change in optical properties that is considered is the small reduction in absorption due to PpIX photobleaching. Nielsen *et al.* (2005) have pointed out that PDT-induced hypoxia and subsequent hemoglobin deoxygenation could have a significant effect on the fluence distribution. This effect could easily be included in the calculations but it has not been done in this paper for two reasons. First, the average concentration of hemoglobin in the dermis and its contribution to the total absorption coefficient is not well characterized and probably varies from subject to subject. Second, the deoxygenation of hemoglobin and subsequent increase in μ_a at 633 nm could be offset by a decrease in the total concentration of hemoglobin due to vasoconstriction. Cottrell *et al.* (2008) reported no significant changes in the reflectance spectrum measured at PDT treatment sites in their clinical study - a finding that suggests that the PDT-induced changes in optical properties are not large. As shown in figure 3.14, the hypoxic region where these changes could occur can be less than 1 mm thick. In further development of the model the calculation of diffuse reflectance will be incorporated to explore this question.

Another feature of this model that could be considered overly simplistic is the assumption that each 50 micron layer of skin has its own independent microvasculature. In reality blood is transported vertically in the dermis (see figure 3.10) so that a reduction in flow at a given depth could affect the oxygen supply in more superficial layers. It has been demonstrated that good agreement with the clinical photobleaching data can be achieved without including this feature. Presumably this is because the singlet oxygen dose is always higher for more superficial vessels and they are affected before the underlying vasculature. It would be possible to include a more realistic representation of the blood supply in the skin, such as that described by Wang (2005), but this would require a much more complex 3D model of perfusion that may not be necessary under these circumstances.

The role of vertical oxygen diffusion both from the atmosphere and within tissue was investigated at the representative irradiance of 50 mW cm^{-2} for three scenarios: first, no vertical oxygen diffusion was taken into account; second, no oxygen diffusion from the air but vertical diffusion within the tissue; third, the top 50 μm layer having the same diffusion coefficient as other layers representing the lack of an intact stratum

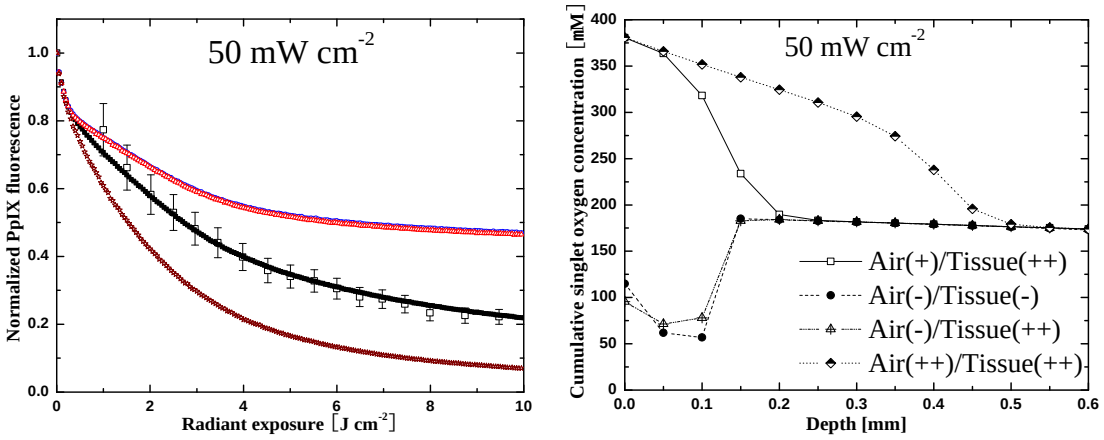

Figure 3.16: The influence of oxygen diffusion on fluorescence photobleaching and singlet oxygen dose distribution at 50 mW cm^{-2} irradiance. (a), normalized PpIX fluorescence: top two overlapped curves are for the cases: (1) no oxygen diffusion from the skin surface or within tissue and (2) no diffusion from the skin surface; the second curve is about 1% lower; the middle (dark) curve is the original fit to clinical data with diffusion from both sources; the curve at the bottom is for the case when the stratum corneum layer has the same oxygen diffusion coefficient as the rest of the tissue. (b), singlet oxygen distributions at 9.6 J cm^{-2} for the same four cases as (a); the sign '+' and '−' represent the presence and the lack of oxygen diffusion, and the '++' symbol indicates the greater diffusion coefficient (1.25×10^{-5} cm^{2}s^{-1}) compared to '+' (0.2×10^{-5} cm^{2}s^{-1}) for the stratum corneum.

corneum (SC) layer. The simulated PpIX fluorescence and singlet oxygen dose for these three cases are compared with those previously obtained in figure 3.16.

Figure 3.16(a) shows that PpIX bleaching is significantly slower in the first two cases, but not much difference is observed between these two cases. This indicates that oxygen diffusion from the skin surface plays a more important role in the observed photobleaching than diffusion within tissue. This is consistent with the faster bleaching curve in the third case when no diffusion barrier layer (SC) exists. The singlet oxygen distributions at 9.6 J cm^{-2} radiant exposure in the three cases (figure 3.16(b)) are also influenced by oxygen diffusion, but these effects are limited to the superficial layers (up to 500 μm depth). Singlet oxygen dose in the epidermis (top 100 μm) is much lower than the original results if the oxygen supply from the skin surface is absent. Without the intact stratum corneum layer (the third case), oxygen from the atmosphere can diffuse more easily into the deeper tissue, which permits

more $^1O_2$ production. This is clearly demonstrated in figure 3.16(b), and could be important in treating skin disease where the stratum corneum is disrupted.

In this model the stratum corneum was a 50 μm layer with a lower oxygen diffusion coefficient than the underlying tissue but the same oxygen solubility. In reality the stratum corneum is thinner and probably has lower oxygen solubility. However, for such a thin barrier, the effect on deeper skin layers is determined by the product of the diffusion coefficient, the solubility, and the thickness. Tests with the model have shown that any combination of these three parameters with the same product will lead to the same simulation results. The exception is the oxygen concentration in the stratum corneum itself, (which will be proportional to the solubility) but this is of little significance as long as it is high enough to maintain PpIX photobleaching.

3.4 Conclusion

A one-dimensional model was developed to simulate ALA-PDT of normal human skin. The model incorporates the essential photochemical reaction kinetics and spatial variations of fundamental elements including light fluence rate and photosensitizer (PpIX) concentration. The model also takes into account oxygen diffusion and perfusion from blood vessels, as well as the cumulative $^1O_2$-dependent vascular response. With this $^1O_2$-induced vascular response, the simulated PpIX fluorescence matches published clinical data for a wide range of irradiances, showing that the model generates reasonable results when input parameters from the literature are used. The simulation of the dynamic ALA-PDT process provides insight into distributions of sensitizer, ground-state oxygen and singlet oxygen during treatment. The quantitative calculations of these distributions can be potentially improved once more information regarding the physiological and photophysical parameters of *in-vivo* ALA-PDT is obtained from future experimental and clinical work. Future measurements using laser Doppler imaging or Doppler optical coherence tomography are also necessary to support the hypothesis of PDT-induced reduction of oxygen supply.

Oxygen diffusion results from the non-uniform distribution of oxygen caused mainly by PDT consumption. In this model, it was found that vertical oxygen diffusion from the skin surface plays a more important role than diffusion within the skin for ALA-PDT.

The current model is also capable of calculating photosensitizer fluorescence and singlet oxygen luminescence, which enables investigation of the correlation of both emission signals to singlet oxygen distribution and to cumulative singlet oxygen dose.

Acknowledgements

This research has been supported by the Canadian Cancer Society Research Institute. The authors appreciate helpful discussions with Mark Jarvi and Brian Wilson of the Department of Medical Biophysics, University of Toronto.

Bibliography

Baumgärtl, H., Ehrly, A. M., Saeger-Lorenz, K., and LübbersW, D. W. (1987). Initial results of intracutaneous measurements of pO_2 profiles. In H. J. Ehrly A M and H. R, editors, *Clinical Oxygen Pressure Measurement*, pages 121–28. Springer, Berlin.

Boere, I. A., Robinson, D. J., de Bruijn, H. S., Kluin, J., Tilanus, H. W., Sterenborg, H. J. C. M., and de Bruin, R. W. F. (2006). Protoporphyrin IX fluorescence photobleaching and the response of rat Barrett's esophagus following 5-aminolevulinic acid photodynamic therapy. *Photochem. Photobiol.*, **82**, 1638–44.

Cottrell, W. J., Paquette, A. D., Keymel, K. R., Foster, T. H., and Oseroff, A. R. (2008). Irradiance-dependent photobleaching and pain in δ-aminolevulinic acid-photodynamic therapy of superficial basal cell carcinomas. *Clin. Cancer Res.*, **14**, 4475–4483.

Crilly, R. J., Cheong, W., Wilson, B., and Spears, J. R. (1997). Forward-adjoint fluorescence model: Monte Carlo integration and experimental validation. *Applied Optics*, **36**, 6513–19.

Dysart, J. S. and Patterson, M. S. (2006). Photobleaching kinetics, photoproduct formation, and dose estimation during ALA induced PpIX PDT of MLL cells under well oxygenated and hypoxic conditions. *Photochem. Photobiol. Sci.*, **5**, 73–81.

Dysart, J. S., Singh, G., and Patterson, M. S. (2005). Calculation of singlet oxygen dose from photosensitizer fluorescence and photobleaching during mTHPC photodynamic therapy of MLL cells. *Photochem. Photobiol.*, **81**, 196–205.

Farrell, T. J., Wilson, B. C., Patterson, M. S., and Olivo, M. C. (1998). Comparison of the *in vivo* photodynamic threshold dose for Photofrin, Mono- and Tetrasulfonated Aluminum Phthalocyanine using a rat liver model. *Photochem. Photobiol.*, **68**, 394–399.

Finlay, J. C., Mitra, S., Patterson, M. S., and Foster, T. H. (2004). Photobleaching kinetics of Photofrin *in vivo* and in multicell tumor spheroids indicate two simultaneous bleaching mechanisms. *Phys. Med. Biol.*, **49**, 4837–60.

Georgakoudi, I. and Foster, H. T. (1998). Singlet oxygen- versus nonsinglet oxygen-mediated mechanisms of sensitizer photobleaching and their effects on photodynamic dosimetry. *Photochem. Photobiol.*, **67**, 612–625.

Herman, M. A., Fromm, D., and Kessel, D. (1999). Tumor blood-flow ges following protoporphyrin IX-based photodynamic therapy in mice and humans. *J. Photochem. Photobiol. B: Biol.*, **52**, 99–104.

Hill, A. V. (1910). The possible effects of the aggregation of molecules of hemoglobin on its dissociation curve. *J. Physiol.*, **40**, 4–7.

Hudson, J. A. and Cater, D. B. (1964). An analysis of factors affecting tissue oxygen tension. In *Proc. R. Soc. London*, volume 161 of *B*, pages 247–74. The Royal Society.

Josefsen, L. B. and Boyle, R. W. (2008). Photodynamic therapy and the development of metal-based photosensitisers. *Met Based Drugs.*, **v.2008**.

Keene, J. P., Kessel, D., Land, E. J., Redmond, R. W., and Truscott, T. G. (1986). Direct detection of singlet oxygen sensitized by Haematoporphyrin and related compounds. *Photochem. and Photobiol.*, **43**, 117–20.

Kruijt, B., de Bruijn, H. S., van der Ploeg-van den Heuvel, A., de Bruin, R. W. F., Sterenborg, H. J. C. M., Amelink, A., and Robinson, D. J. (2008). Monitoring ALA-induced PpIX photodynamic therapy in the rat esophagus using fluorescence and reflectance spectroscopy. *Photochem. Photobiol.*, **84**, 1515–27.

Laubach, H. J., Chang, S. K., Lee, S., Rizvi, I., Zurakowski, D., Davis, S. J., Taylor, C. R., and Hasana, T. (2008). *In-vivo* singlet oxygen dosimetry of clinical 5-aminolevulinic acid photodynamic therapy. *J. Biomed. Opt.*, **13**.

Liu, B., Farrell, T. J., Patterson, M. S., Jarvi, M. T., and Wilson, B. C. (2009). A Monte Carlo model of detected singlet oxygen luminescence and photosensitizer fluorescence during ALA-PDT of skin. In *Proc. of SPIE*, volume 7380, pages 73806W 1–11.

Mitra, S. and Foster, F. H. (2005). Photophysical parameters, photosensitizer retention and tissue optical properties completely account for the higher photodynamic efficacy of meso-tetra-hydroxyphenyl-chlorin vs Photofrin. *Photochem. Photobiol.*, **81**, 849–59.

Nielsen, K. P., Juzeniene, A., Juzenas, P., Stamnes, K., Stamnes, J. J., and Moan, J. (2005). Choice of optimal wavelength for PDT: the significance of oxygen depletion. *Photochem. Photobiol.*, **81**, 1190–4.

Salomatina, E., Jiang, B., Novak, J., and Yaroslavsky, A. N. (2006). Optical properties of normal and cancerous human skin in the visible and near-infrared spectral range. *J. Biomed. Opt.*, **11**.

Star, W. M., Aalders, M. C. G., Sac, A., and Sterenborg, H. J. C. M. (2002). Quantitative model calculation of the time-dependent protoporphyrin IX concentration in normal human epidermis after delivery of ALA by passive topical application or iontophoresis. *Photochem. Photobiol.*, **75**, 424–32.

Stücker, M., Struk, A., Altmeyer, P., Herde, M., Baumgartl, H., and Lubbers, D. W. (2002). The cutaneous uptake of atmospheric oxygen contributes significantly to the oxygen supply of human dermis and epidermis. *J. Physiol.*, **538**, 985–94.

Vaupel, P. (1976). Effect of percentual water content in tissues and liquids on the diffusion coefficients of $^3O_2$, CO_2, N_2 and H_2. *Pflügers Arch*, **361**, 201–4.

Wang, K. K., Mitra, S., and Foster, T. H. (2007). A comprehensive mathematical model of microscopic dose deposition in photodynamic therapy. *Med. Phys.*, **34**, 282–93.

Wang, K. K., Cottrell, W. J., Mitra, S., Oseroff, A., and Foster, T. H. (2009). Simulations of measured photobleaching kinetics in human basal cell carcinomas suggest blood flow reductions during ALA-PDT. *Lasers Surg. Med.*, **41**, 686–96.

Wang, K. K., Finlay, J. C., Busch, T. M., Hahn, S. M., and Zhu, T. C. (2010). Explicit dosimetry for photodynamic therapy macroscopic singlet oxygen modeling. *J. Biophoton.*, **3**, 304–318.

Wang, L., Jacques, S. L., and Zheng, L. (1995). MCML - Monte Carlo modeling of light transport in multi-layered tissues. *Comput. Meth. Prog. Bio.*, **47**, 131–46.

Wang, L. V., Nordquist, R. E., and Chen, W. R. (1997). Optimal beam size for light delivery to absorption-enhanced tumors buried in biological tissues and effect of multiple-beam delivery: a Monte Carlo study. *Appl. Optics*, **36**, 8286–91.

Wang, W. (2005). Oxygen partial pressure in outer layers of skin: simulation using three-dimensional multilayered models. *Microcirculation*, **12**, 195–207.

Wilson, B. C. and Patterson, M. S. (2008). The physics, biophysics and technology of photodynamic therapy. *Phys. Med. Biol.*, **53**, R61–R109.

Chapter 4

Paper III - Comparison of noninvasive photodynamic therapy dosimetry methods using a dynamic model of ALA-PDT of human skin

Baochang Liu, Thomas J. Farrell and Michael S. Patterson

Department of Medical Physics and Applied Radiation Sciences, McMaster University, 1280 Main Street West, Hamilton, Ontario L8S 4K1, Canada
and
Department of Medical Physics, Juravinski Cancer Centre, 699 Concession Street, Hamilton, Ontario L8V 5C2, Canada

Published in Physics in Medicine an Biology, 2012, **57**, 825-41
Received 12 August 2011, in final form 4 November 2011
Published 18 January 2012
Online at stacks.iop.org/PMB/57/825
Printed with permission
 [DOI: 10.1088/0031-9155/57/3/825]

Introduction to paper III

This chapter will focus on PDT dosimetry. Three noninvasive PDT dosimetry approaches including cumulative singlet oxygen luminescence (CSOL), absolute fluorescence bleaching metric (AFBM) and fractional fluorescence bleaching metric (FFBM) were extensively examined for various treatment conditions. These scenarios include three different treatment irradiances representing low, middle and high portions of the reported clinical range, a wide range of optical properties of the dermis, and different initial sensitizer concentration and distribution. The metrics were correlated to the average reacted singlet oxygen dose in dermis and to the dose at five specific depths. The robustness of these three metrics was compared for all scenarios, and it was found the CSOL is the most robust metric and has good potential to be a 'gold' standard as a metric tool in clinical PDT.

I carried out all the simulations, data analyses, and wrote this manuscript under the supervision of Dr. Patterson, who also provided very useful suggestions on the result analyses and edited my manuscript. In addition, Dr. Farrell helped me with the modification of the theoretical model.

Contents of Paper III

Abstract

A numerical model of ALA photodynamic therapy of human skin was used to calculate photosensitizer fluorescence and singlet oxygen luminescence (SOL) observable at the skin surface during treatment. From the emissions, three practical dose metrics were calculated: the fractional fluorescence bleaching metric (FFBM) given by $\ln \frac{F_0}{F}$, where F is photosensitizer protoporphyrin IX (PpIX) fluorescence and F_0 is its initial value, the absolute fluorescence bleaching metric (AFBM) given by $F_0 - F$, and the cumulative SOL (CSOL). These three metrics can be measured during clinical PDT treatment, but their relation to actual singlet-oxygen distribution in the skin is complex and may depend on treatment parameters such as irradiance. Using the model, the three metrics were compared to the average singlet-oxygen dose in the dermis. Despite the complex dependence of $^1O_2$ concentration on depth, a roughly linear correlation was found for all three dose metrics. The correlation for the FFBM was not robust when treatment parameters were varied and this metric was especially sensitive to the initial PpIX concentration and its depth dependence. The AFBM was less sensitive to treatment conditions but CSOL demonstrated the best overall performance.
Keywords: Photodynamic therapy, ALA, dosimetry, fluorescence, photobleaching, singlet oxygen luminescence

4.1 Introduction

Photodynamic therapy (PDT) combines a light source, a light activatable drug called a photosensitizer and molecular oxygen in tissue to treat various malignant and non-malignant diseases. Normally, the systemically or topically administered photosensitizer is preferentially retained by the target tissue which is subsequently exposed to light at a wavelength efficiently absorbed by the sensitizer. Energy is transferred from the excited sensitizer to molecular oxygen resulting in the production of singlet-state oxygen (singlet oxygen, $^1O_2$). This highly reactive species is the main vehicle for the therapeutic effect of PDT.

ALA-PDT uses the prodrug 5-aminolevulinic acid (ALA) to synthesize the photosensitizer protoporphyrin IX (PpIX) in the target cell via the endogenous heme biosynthetic pathway. Topical ALA-PDT has been applied to treat a variety of superficial skin diseases such as superficial basal cell carcinoma (sBCC), Bowens disease and actinic keratoses (AK) (Tschen *et al.* 2006). As topical ALA-PDT can be performed at short wavelengths for superficial disease, there has been some off-label use

of this modality in cosmetic treatments such as skin rejuvenation or for acne (Wilson and Patterson 2008). ALA-PDT has also been tested clinically as a treatment option for fungal infections (Chabrier-Rosello *et al.* 2005). However, the therapeutic outcomes of ALA-PDT for thicker target volumes have not been as good (Wolf *et al.* 1993). This may be due to the limited penetration of both prodrug ALA and excitation light, the availability of ground-state molecular oxygen, and the synthesis of PpIX by cells in different environments inside the thick tissue.

The production of singlet oxygen involves excitation light, photosensitizer and tissue oxygen, and each of these components usually has temporal and spatial variations in its distribution prior to and during light exposure. Moreover, they may also influence each other during treatment. This complexity makes PDT dosimetry a challenging problem and many possible solutions have been pursued. These have been classified by Wilson and Patterson (2008) as explicit, implicit, or direct dosimetry.

Explicit dosimetry aims to monitor all three PDT components, i.e. light fluence rate, tissue oxygen and photosensitizer, and to calculate the local singlet-oxygen concentration or a quantity proportional to it. Continuous real-time measurements are difficult for both technical and practical reasons. Even though the real-time sensitizer distribution may be monitored via fluorescence, detailed distributions of light fluence rate and tissue oxygen are not easily obtained.

Implicit dosimetry, the focus of much recent attention, attempts to measure the production of singlet oxygen indirectly. The most common method is to monitor the loss of photosensitizer fluorescence, or photobleaching, on the basis that this is caused by reaction of the ground state sensitizer with singlet oxygen. Two common measures of sensitizer photobleaching are the absolute sensitizer concentration loss and the fraction of sensitizer lost. Although some preclinical success (Dysart *et al.* 2005; Boere *et al.* 2006) has been achieved with this approach, it may not be applicable to all photosensitizers because bleaching can be caused by other reactions that do not involve singlet oxygen (Finlay *et al.* 2004). The loss of photosensitizer fluorescence may also be the result of relocalization of photosensitizer rather than a reduction in concentration (Robinson *et al.* 1998).

The third approach is direct dosimetry. As singlet oxygen is the main vehicle for biological damage, a direct *in vivo* monitor of its production is ideal as a dosimetric tool. Singlet-oxygen luminescence (SOL) at 1270 nm has been detected during PDT, but it is a weak signal due to the sub-microsecond lifetime in tissue and the resultant low instantaneous concentration. The detection of SOL in human subjects was recently reported by Laubach *et al.* (2008).

Both implicit and direct dosimetry approaches are being applied during ALA-PDT of normal human skin and skin cancer (Cottrell *et al.* 2008; Laubach *et al.* 2008). However, the correlation of these signals with the actual singlet-oxygen spatial distribution and with the average $^1O_2$ 'dose' in a defined tissue volume has not

been thoroughly investigated. Even though the singlet-oxygen dose required to cause biological response has been studied (Farrell *et al.* 1998; Wang *et al.* 2010), it is difficult to predict PDT outcomes from the detected signals without understanding their relationships to the singlet-oxygen distribution.

To tackle these questions, a dynamic model for ALA-PDT of skin was recently introduced by our group. The detailed description of this model and the calculated temporal and spatial distributions of photosensitizer, ground-state oxygen and singlet oxygen were reported by Liu *et al.* (2010). Subsequently, Valentine *et al.* (2011) also used Monte Carlo (MC) simulations to calculate the PpIX fluorescence and singlet-oxygen production during PDT of superficial basal call carcinomas. However, their model did not incorporate depth-dependent photosensitizer concentration or oxygen depletion and its effects on singlet-oxygen yield and photosensitizer bleaching. This paper will focus on the fluorescence and SOL signals and their relationship to singlet-oxygen dose. The dependence of these relationships on tissue optical properties, photosensitizer concentration and distribution, and treatment irradiance will also be investigated so the robustness of the implicit and direct approaches can be compared.

4.2 Theory and Method

4.2.1 Description of the model

The details of the dynamic one-dimensional ALA-PDT of skin model have been described in Liu *et al.* (2010), and only a brief summary is provided in this section. The model used a simplified three-layer (epidermis, dermis and subcutaneous fat) representation of normal human skin. Table 4.8 shows the layer thickness and the baseline absorption and reduced scattering coefficients at the wavelengths of interest.

The model used the MC method (Wang *et al.* 1995) to simulate photon transport in tissue and to obtain the excitation light fluence rate distribution. The delta-scattering technique (Wang *et al.* 1997) combined with the null event test was adopted to handle the different attenuation coefficients in the three layers.

The model accounted for vertical ground-state oxygen ($^3O_2$) diffusion including transfer from the atmosphere across the stratum corneum. This was based on Fick's second law given in equation (4.69), where D is the tissue oxygen diffusion coefficient, and then rewritten in terms of oxygen partial pressure (pO_2) using Henry's law in equation (4.70), where α is the oxygen solubility coefficient and P is the oxygen partial pressure.

$$\left(\frac{\mathrm{d}\left[^3O_2\right]_z}{\mathrm{d}t}\right) = D\left(\frac{\mathrm{d}^2\left[^3O_2\right]_z}{\mathrm{d}z^2}\right), \tag{4.69}$$

$$\left[^3O_2\right] = \alpha \times \mathrm{P}\,. \tag{4.70}$$

Table 4.8: Optical properties of normal human skin. Data were extracted from Salomatina *et al.* (2006). The excitation wavelength is 633 nm, and the photosensitizer fluorescence and singlet-oxygen phosphorescence wavelengths are 705 and 1270 nm, respectively. μ_a is the absorption coefficient, μ_s' is the reduced scattering coefficient and unit is mm^{-1}. The refractive index is 1.4 for all three layers.

		633 (nm)		705 (nm)		1270 (nm)	
Tissue	Thickness (mm)	μ_a	μ_s'	μ_a	μ_s'	μ_a	μ_s'
Epidermis	0.1	0.25	5.0	0.25	4.0	0.05	2.5
Dermis	2.5	0.17	2.5	0.15	2.5	0.1	1.6
Sub-Q	25	0.12	2.5	0.12	2.3	0.1	1.5

Using the continuity in pO_2 and in the oxygen flux as the boundary conditions at depth z, as expressed in equations (4.71) and (4.72), the final expression for pO_2 at the depth z can be derived as shown in equation (4.73), where Δz was the depth grid increment (50 μm in this study), and the subscripts '$-$' and '$+$' represent the depths above and below z, respectively.

$$P_{z^-} = P_{z^+} , \tag{4.71}$$

$$D_-\alpha_-\left(\frac{dP_{z^-}}{dz}\right) = D_+\alpha_+\left(\frac{dP_{z^+}}{dz}\right) . \tag{4.72}$$

$$\left(\alpha_z\frac{dP_z}{dt}\right)_{\text{diffusion}} = \frac{D_-\alpha_-\left(P_{(z-\Delta z,t)} - P_{(z,t)}\right) - D_+\alpha_+\left(P_{(z,t)} - P_{(z+\Delta z,t)}\right)}{(\Delta z)^2} . \tag{4.73}$$

In addition to oxygen supplied by diffusion, a perfusion term was also included. The perfusion oxygen supply rate at depth z is expressed by equation (4.74), where K_z is a reacted $^1O_2$ dose-dependent function, and $[^3O_2]_v$ is the oxygen concentration in the blood vessels:

$$\left(\frac{d\left[^3O_2\right]_z}{dt}\right)_{\text{perfusion}} = K_z \times \left(\left[^3O_2\right]_v - \left[^3O_2\right]_z\right) . \tag{4.74}$$

As discussed in more detail in Liu *et al.* (2010), the perfusion term was reduced commensurate with PDT-induced vascular damage. This is described in equation (4.75), representing a sigmoidal $^1O_2$ dose response curve, where D_{50} is the $^1O_2$ dose that halves the initial K value and a is the slope. This response curve was also found

to be irradiance dependent (Liu *et al.* 2010).

$$K_z(t) = K_0 \left(1 - \frac{1}{1 + \mathrm{e}^{-a\left(\int_0^t [^1\dot{\mathrm{O}}_2]_z(t')\mathrm{d}t' - D_{50}\right)}}\right) . \tag{4.75}$$

The metabolic consumption (Γ_{met}) of oxygen was expressed using the Michaelis-Menten relationship (Hudson and Cater 1964) in equation (4.76), where $\Gamma_{\mathrm{met}}^{\mathrm{max}}$ is the initial maximum metabolic consumption rate of human skin in the steady state, and k_{50} is the $^3O_2$ concentration at which Γ_{met} is half of $\Gamma_{\mathrm{met}}^{\mathrm{max}}$.

$$\Gamma_{\mathrm{met}} = \Gamma_{\mathrm{met}}^{\mathrm{max}} \frac{[^3\mathrm{O}_2]}{k_{50} + [^3\mathrm{O}_2]} . \tag{4.76}$$

The PDT oxygen consumption Γ_{PDT} can be derived from a set of differential equations describing the possible photochemical reaction pathways during PDT. In the quasi-steady state, the rates of change of the ground-state sensitizer $[\mathrm{S}_0]$ and oxygen $[^3\mathrm{O}_2]$ concentrations due to PDT are shown in the following equations:

$$\begin{aligned} \frac{\mathrm{d}\,[\mathrm{S}_0]}{\mathrm{d}t} &= -\phi_{\mathrm{t}} I_{\mathrm{a}} \frac{k_{\mathrm{ta}}\,[\mathrm{A}]\,/k_{\mathrm{ot}}}{k_{\mathrm{p}}/k_{\mathrm{ot}} + k_{\mathrm{ta}}\,[\mathrm{A}]\,/k_{\mathrm{ot}} + [^3\mathrm{O}_2]} \\ &\quad \times \left[1 + \frac{\frac{k_{\mathrm{os}}}{k_{\mathrm{oa}}[\mathrm{A}]}}{k_{\mathrm{ta}}\,[\mathrm{A}]\,/k_{\mathrm{ot}}} \frac{S_\Delta}{\frac{k_{\mathrm{d}}}{k_{\mathrm{oa}}[\mathrm{A}]} + 1} \left([\mathrm{S}_0] + \delta\right) [^3\mathrm{O}_2]\right] , \end{aligned} \tag{4.77}$$

$$\frac{\mathrm{d}\,[^3\mathrm{O}_2]}{\mathrm{d}t} = -S_\Delta I_{\mathrm{a}} \phi_{\mathrm{t}} \frac{1}{\frac{k_{\mathrm{d}}}{k_{\mathrm{oa}}[\mathrm{A}]} + 1} \left[1 + \frac{k_{\mathrm{os}}}{k_{\mathrm{oa}}\,[\mathrm{A}]} \left([\mathrm{S}_0] + \delta\right)\right] \frac{[^3\mathrm{O}_2]}{k_{\mathrm{p}}/k_{\mathrm{ot}} + \frac{k_{\mathrm{ta}}[\mathrm{A}]}{k_{\mathrm{ot}}} + [^3\mathrm{O}_2]} , \tag{4.78}$$

where:

$$\phi_{\mathrm{t}} = \frac{k_{\mathrm{isc}}}{k_{\mathrm{f}} + k_{\mathrm{isc}}} . \tag{4.79}$$

The details of this derivation can be found elsewhere (Liu *et al.* 2009, 2010). Table 4.9 provides the definitions of the variables.

Considering all the mechanisms briefly described above, the final two differential equations used to calculate the concentration of ground-state PpIX and oxygen partial

Table 4.9: Definitions of the notations and variables in the photobleaching reaction equations.

Symbol	Definition	Units
$[S_0]$	Ground-state sensitizer	M
$[S_1]$	Singlet excited-state sensitizer	M
$[T_1]$	Triplet excited-state sensitizer	M
$[^3O_2]$	Triplet ground-state oxygen	M
$[^1O_2]$	Singlet excited-state oxygen	M
$[A]$	Molecular substrate	M
k_f	$S_1 \rightarrow S_0$	s^{-1}
k_p	$T_1 \rightarrow S_0$	s^{-1}
k_{isc}	$S_1 \rightarrow T_1$	s^{-1}
k_d	$^1O_2 \rightarrow {}^3O_2$	s^{-1}
k_{ot}	Bimolecular rate constant for reaction of $^3O_2$ with T_1	$M^{-1}s^{-1}$
k_{os}	Bimolecular rate constant for reaction of $^1O_2$ with S_0	$M^{-1}s^{-1}$
k_{oa}	Bimolecular rate constant for reaction of $^1O_2$ with A	$M^{-1}s^{-1}$
k_{sa}	Bimolecular rate constant for reaction of S_1 with A	$M^{-1}s^{-1}$
k_{ta}	Bimolecular rate constant for reaction of T_1 with A	$M^{-1}s^{-1}$
I_a	Photon absorption rate	$M\ s^{-1}$
ϕ_t	Sensitizer triplet yield	
S_Δ	Fraction of T_1 and $^3O_2$ reactions that produce $^1O_2$	
σ	Absorption cross section of S_0	cm^2
Φ_D	$^1O_2$ quantum yield	

pressure at each depth during PDT are shown as follows:

$$\begin{aligned}\frac{\mathrm{d}\left[S_0\right]_z}{\mathrm{d}t} &= -\dot{F}_{ex}\left[S_0\right]_z \frac{k_{ta}\left[A\right]/k_{ot}}{k_p/k_{ot} + k_{ta}\left[A\right]/k_{ot} + \alpha_z P_z} \\ &\quad \times \left[\phi_t \frac{\sigma}{h\nu} + \frac{\frac{k_{os}}{k_{oa}[A]}}{k_{ta}\left[A\right]/k_{ot}} \beta'_{PDT}\left(\left[S_0\right]_z + \delta\right)\alpha_z P_z\right] , \qquad (4.80)\end{aligned}$$

$$\begin{aligned}\alpha_z \frac{\mathrm{d}P_z}{\mathrm{d}t} &= -\dot{F}_{ex}\left[S_0\right]_z \beta'_{PDT}\left[1 + \frac{k_{os}}{k_{oa}\left[A\right]}\left(\left[S_0\right]_z + \delta\right)\right] \frac{\alpha_z P_z}{k_p/k_{ot} + \frac{k_{ta}[A]}{k_{ot}} + \alpha_z P_z} \\ &\quad -\Gamma^{max}_{met} \frac{\alpha_z P_z}{k_{50} + \alpha_z P_z} + K_z\left(\left[{}^3O_2\right]_v - \alpha_z P_z\right) \\ &\quad + \frac{D_-\alpha_-\left(P_{z-\Delta z} - P_z\right) - D_+\alpha_+\left(P_z - P_{z+\Delta z}\right)}{\left(\Delta z\right)^2} , \qquad (4.81)\end{aligned}$$

where :

$$\beta'_{\mathrm{PDT}} = S_{\Delta}\phi_{\mathrm{t}}\frac{\sigma}{h\nu}\frac{1}{\frac{k_{\mathrm{d}}}{k_{\mathrm{oa}}[\mathrm{A}]}+1} . \tag{4.82}$$

By manipulating the photochemical reaction differential equations, the instantaneous production rate of $^1O_2$ at each depth can be derived as follows:

$$[\dot{^1\mathrm{O}_2}] = I_{\mathrm{a}}\Phi_{\mathrm{D}}\frac{[^3\mathrm{O}_2]}{k_{\mathrm{p}}/k_{\mathrm{ot}}+\frac{k_{\mathrm{ta}}[\mathrm{A}]}{k_{\mathrm{ot}}}+[^3\mathrm{O}_2]} . \tag{4.83}$$

Finally, the model used the adjoint MC method to calculate the emission signals (both PpIX fluorescence and $^1O_2$ 1270 nm luminescence) escaping from the surface (Crilly *et al.* 1997). PpIX fluorescence and SOL signals at the skin surface are shown in the following equations:

$$\dot{\mathrm{E}}_{\mathrm{m705}} = \int_0^{\infty} \dot{F}_{\mathrm{ex}}(z)\mu_{a,\mathrm{d}}(z)\phi_{\mathrm{f}}F_{\mathrm{em}_{705}}(z)C_{\mathrm{r}}\mathrm{d}z , \tag{4.84}$$

$$\dot{\mathrm{E}}_{\mathrm{m1270}} = \int_0^{\infty} [\dot{^1\mathrm{O}_2}](z)\phi_{\mathrm{d}}F_{\mathrm{em}_{1270}}(z)C_{\mathrm{r}}\mathrm{d}z , \tag{4.85}$$

where $\dot{F}_{\mathrm{ex}}(z)$ and $F_{\mathrm{em}}(z)$ are the fluence rate and relative fluence at the excitation and corresponding emission wavelengths, respectively; $\mu_{a,\mathrm{d}}(z)$ is the absorption coefficient of PpIX; ϕ_{f} and ϕ_{d} are the PpIX fluorescence and $^1O_2$ luminescence quantum yields, and C_{r} is an empirical scaling factor derived from the adjoint MC simulations. This 1D model corresponds to the detection geometry employed by Cottrell *et al.* (2008). If a contact fiber optic probe were used to measure emitted light, the calculations would have to be modified to account for the probe geometry.

4.2.2 Treatment simulations

The goal of this study is to examine the relationship between potential noninvasive dose metrics and actual singlet-oxygen dose. This assumes that singlet-oxygen dose is correlated to clinically relevant PDT outcomes, such as erythema in the case of normal skin or tumor response in the case of skin cancer. Eventually, clinical trials must be performed to validate the application of noninvasive dosimetry but simulations, such as those reported here, are extremely useful in designing such trials and in interpreting their outcome. The model calculates the singlet-oxygen dose as a function of depth but it is not clear whether there is a 'critical' depth that would be most important in predicting response. For that reason we have chosen to report the average singlet-oxygen dose over the entire dermis as the primary 'endpoint' although some depth-resolved results are also presented.

Three noninvasive dose metrics are compared in this study. The first is the total cumulative SOL (CSOL) emitted from the skin surface during the treatment. In a simple, homogeneous medium it is evident that this quantity will be directly correlated to the singlet-oxygen dose, but during PDT of the skin, the PpIX and oxygen concentrations have a complex and dynamic depth dependence and the validity of this correlation is no longer obvious. The second dose metric is the fractional fluorescence bleaching metric (FFBM), defined simply as the ratio of the observed PpIX fluorescence signal F to its value at the start of treatment F_0. Several clinical studies have reported data for this parameter, while Dysart *et al.* (2005) showed that when the photosensitizer concentration is high, the singlet-oxygen dose is proportional to $\ln \frac{F_0}{F}$. These authors also pointed out that at the low concentrations typical of *in vivo* PDT, a better measure should be the absolute change in the magnitude of the fluorescence signal, i.e. initial PpIX fluorescence signal minus final PpIX fluorescence signal. We refer to this metric as the absolute fluorescence bleaching metric (AFBM). All three metrics CSOL, FFBM, and AFBM were calculated at various time points throughout the simulated treatment and compared to the singlet-oxygen dose.

Even if a good correlation is observed between the dose metric and the singlet-oxygen dose as treatment progresses, it is also necessary to examine the robustness of this correlation when treatment parameters, such as irradiance, are changed. A benchmark treatment simulation was performed with the optical properties given in table 4.8 and a treatment irradiance of 50 mW cm^{-2}. As described by Liu *et al.* (2010), the PpIX concentration was 4.4 μM on the skin surface and decreased exponentially with a 1/e depth of 1.25 mm. The other parameters used in the simulations are listed in table 4.10. In the first test of robustness, the irradiance was changed to 20 mW cm^{-2} and 150 mW cm^{-2} and the performance of the three dose metrics was compared to that in the benchmark study. This was followed by a second test in which the absorption and scattering coefficients of the dermis at the treatment excitation wavelength were increased and decreased by a factor of 2 compared to the benchmark. Finally, in a third test, the PpIX concentration at all depths was increased and decreased by a factor of 2, and then, the depth dependence of the PpIX concentration was drastically altered to a step function so that it was 4.4 μM in the epidermis and 1.76 μM in the dermis.

Table 4.10: Photophysical and physiological parameters. D_{50} values correspond to 20, 50 and 150 mW cm^{-2}. D=0.2×10^{-5} cm^{2}s^{-1} was used only in the top 50 μm stratum corneum layer, and D=1.25 ×10^{-5} cm^{2}s^{-1} was used for other layers.

Parameters	Values (Published data)	Reference	Units
$(k_{os}/k_{oa}\,[A])$	90	Georgakoudi and Foster (1998)	M^{-1}
$(k_p/k_{ot})^*$	4±2 (5.8-11.6: mTHPC)	Mitra and Foster (2005)	μM
$(k_{ta}\,[A]\,/k_{ot})$	0		μM
$(\Gamma_{met}^{max})^*$	1.5±0.3 (1-1.56)	Stücker *et al.* (2002)	μM s^{-1}
δ^*	128±20 (33-330: mTHPC)	Dysart *et al.* (2005)	μM
k_{50}	0.5	Wang *et al.* (2007)	μM
K_0	0.0370		s^{-1}
$\left[^3O_2\right]_v$	80		μM
a	0.08		μM^{-1}
D_{50}	191/155/108	Liu *et al.* (2010)	μM
D^*	0.2/1.25±0.05(1-1.5)×10^{-5}	Wang (2005)	cm^{2}s^{-1}
α	1.25×10^{-6}		M mmHg^{-1}
ϵ_{PpIX}	3000 (633 nm)		M^{-1}cm^{-1}
β'_{PDT}	0.021 (633 nm)		mJ^{-1}cm^2
ϕ_f	0.05		
ϕ_d	10^{-8}		
ϕ_t	0.83	Josefsen and Boyle (2008)	
Φ_D	0.57	Keene *et al.* (1986)	

* The parameters with the uncertainties were estimated by Liu *et al.* (2010). The published values are also included to show the ranges in the literature.

4.3 Results and Discussion

4.3.1 Calculated emission signals

In this section representative fluorescence and SOL simulation results are presented. The origin of the observed signal is investigated by tracking the signal at five depths during the course of treatment.

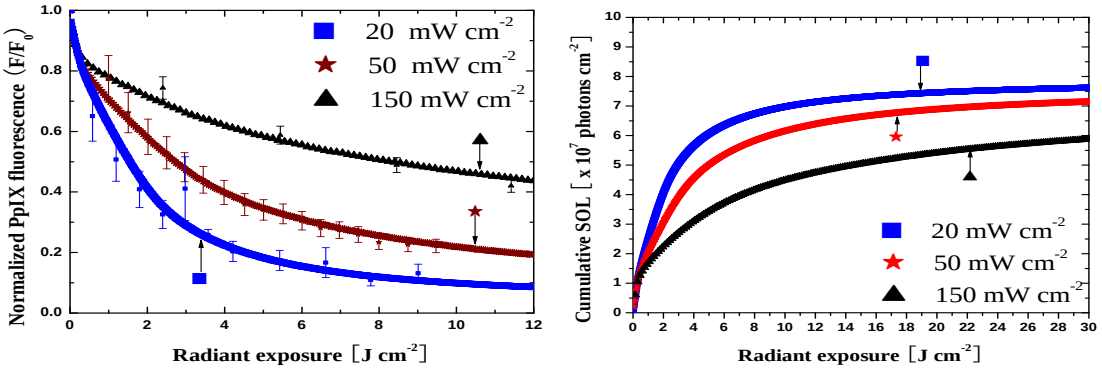

Figure 4.17: Normalized PpIX fluorescence (705 nm) and CSOL emission signals escaped from the skin surface.

Figure 4.17 shows the calculated normalized PpIX fluorescence and CSOL emission signals emitted at the skin surface as the functions of radiant exposure at irradiances of 20, 50 and 150 mW cm^{-2}. The total radiant exposure of 200 J cm^{-2} was delivered at 150 mW cm^{-2} and 50 J cm^{-2} at the other two irradiances. Figure 4.17(a) includes the clinical data (denoted as the points with standard deviations) measured from normal human skin under the same conditions by Cottrell *et al.* (2008). Figure 4.17(b) presents the CSOL emission. The signals increase rapidly during early PDT, but at all three irradiances this is followed by a plateau where the instantaneous SOL is much lower. The largest signal is produced at the lowest irradiance, and the earliest occurrence of the plateau is also observed (about 6 J cm^{-2}) because PpIX is bleached fastest at this irradiance. Similar trends and irradiance-dependent features were observed in experimental studies on normal mouse skin (Niedre *et al.* 2005).

The origin of fluorescence and SOL was examined in more detail. Figure 4.18 shows the PpIX fluorescence that reaches the skin surface from a 50 μm thick tissue layer at five depths for 20, 50 and 150 mW cm^{-2}. The plots are on a logarithmic scale. At the start of treatment at 20 mW cm^{-2}, the largest contribution comes from the surface, but this is rapidly bleached due to a constant supply of oxygen. At 0.2 and 0.5 mm, the initial rate of photobleaching is greatly reduced by the induction

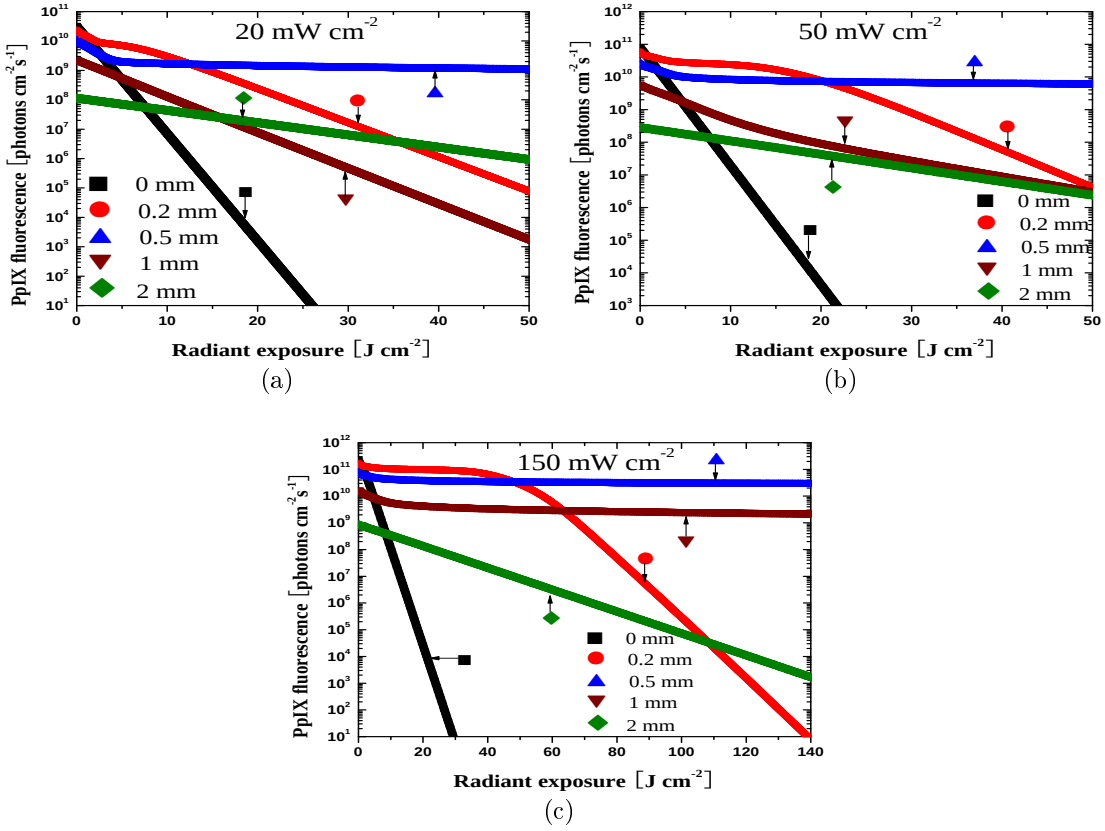

Figure 4.18: The escaped PpIX fluorescence emission from five depths: 0, 0.2, 0.5, 1 and 2 mm.

of hypoxia, but increases again at 0.2 mm as oxygen diffuses from the surface. At 1 and 2 mm, bleaching proceeds at a constant slower rate as the fluence rate is too low to cause hypoxia. At higher irradiance, similar features are observed although the fluence rate is high enough to induce hypoxia and slower bleaching at depths beyond 1 mm. In all cases, by the end of treatment, the largest contribution to fluorescence arises from intermediate depths around 0.5 mm. Additional plots showing oxygen and PpIX concentration versus depth were presented in Liu *et al.* (2010).

The same analysis was performed for the instantaneous SOL emission rate, and the results are shown in figure 4.19. In figures 4.19(a)-(c), it can be seen that the instantaneous SOL emission rates in the upper dermis are dramatically reduced during early light exposure (0-3 J cm^{-2}). The inset in figure 4.19(b) shows the logarithmic scale plot of the figure but for radiant exposure up to 50 J cm^{-2}. This plot illustrates that because the production of $^1O_2$ in the upper layers is limited due to oxygen depletion and bleaching of PpIX, most of the SOL emission at the later exposure

comes from 0.5 mm and deeper. The features are consistent with the fluorescence data in figure 4.18. Note the secondary increase in SOL at depth 0.2 mm at about 18 J cm^{-2} that results from oxygen diffusion from the skin surface. These secondary increases are found at different radiant exposures for all three irradiances as shown in figure 4.19(d). This oxygen diffusion from the surface has a significant influence on the production of $^1O_2$ in the deep layers after the complete loss of sensitizer in the overlying layers and the reduction of the vascular oxygen supply.

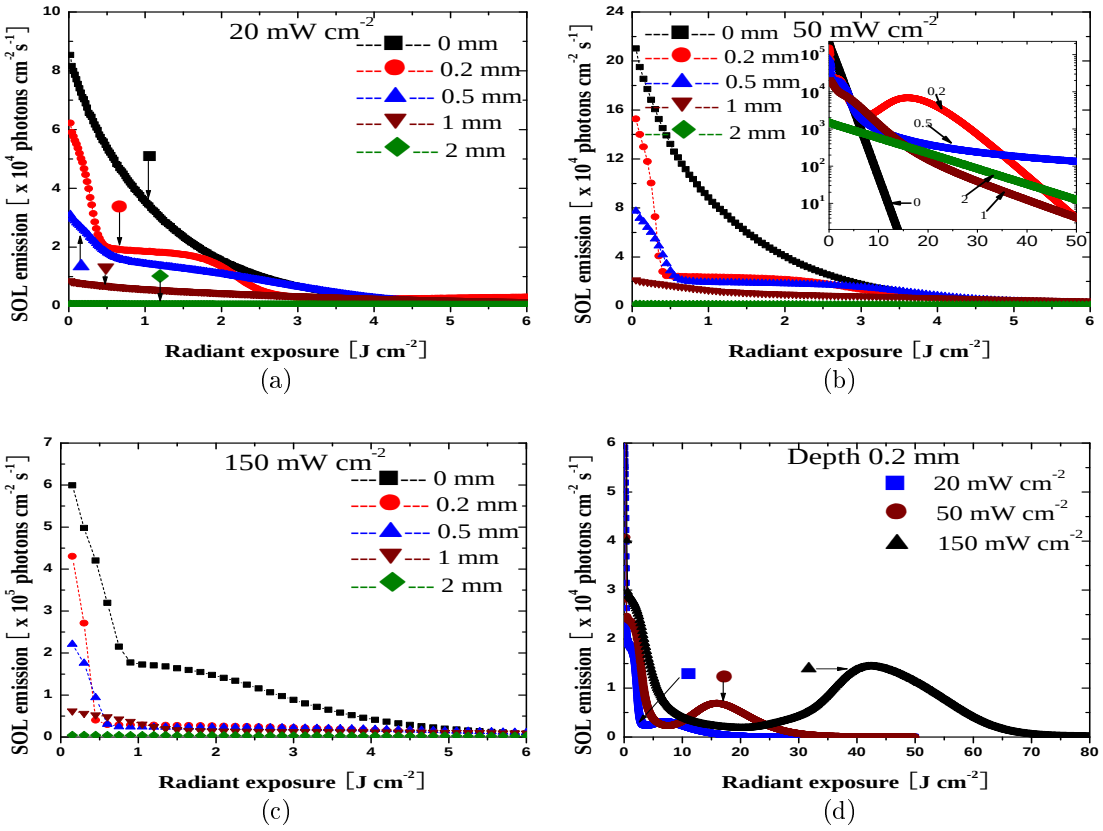

Figure 4.19: SOL that reaches the skin surface from a 50 μm thick layer located at five different depths. This is plotted versus radiant exposure for irradiance of (a) 20 mW cm^{-2}, (b) 50 mW cm^{-2} and (c) 150 mW cm^{-2}. The inset shows the data on a logarithmic scale over a wider range of radiant exposure. (d) The evolution of the SOL from a layer at depth 0.2 mm over the full course of PDT treatment.

4.3.2 Dosimetry comparison for varied treatment parameters

As described above, three metrics, i.e. AFBM, FFBM and CSOL, were compared to the average $^1O_2$ 'dose' in dermis. Simulations were performed for varied treatment irradiance, optical properties of the dermis, and initial PpIX concentration and distribution. The ideal dose metric would have a linear relation to singlet-oxygen dose that would be insensitive to variations in the treatment conditions.

Figure 4.20 shows the comparison for different irradiances. Because photosensitizer fluorescence is proportional to irradiance, the AFBM has been corrected for this effect. As seen in figure 4.20(a) and (b), the relationship between FFBM and AFBM metrics and the singlet-oxygen dose depends upon irradiance. The maximum spread in singlet-oxygen dose for a given value of either dose metric is about 20%. CSOL (figure 4.20(c)) is much close to the ideal linear correlation and the maximum spread in dose is only about 10%. Figure 4.20(d) shows the singlet-oxygen dose versus radiant exposure - the *de facto* dose metric in most clinical treatments. As expected, the correlation in figure 4.20(d) is poor and not robust with respect to irradiance.

Figure 4.21 shows a similar comparison of the dose metrics for a wide range of optical properties of the dermis at the treatment and fluorescence excitation wavelength. For simplicity only the properties of the dermis at 633 nm were changed - changes at longer wavelengths or in the epidermis would have a smaller effect on the observed signals. The range takes into account all the combinations of approximately doubled or halved absorption and reduced scattering coefficients of dermis compared to the benchmark simulation. For the AFBM, the dose can vary by up to a factor of 2 for the same AFBM. The FFBM is more robust but still inferior to CSOL. Skin color and type vary among patients, and this comparison indicates that CSOL has the potential to account for this. Note that the performance of the AFBM could probably be improved by a real-time correction for optical properties based on, e.g., diffuse reflectance.

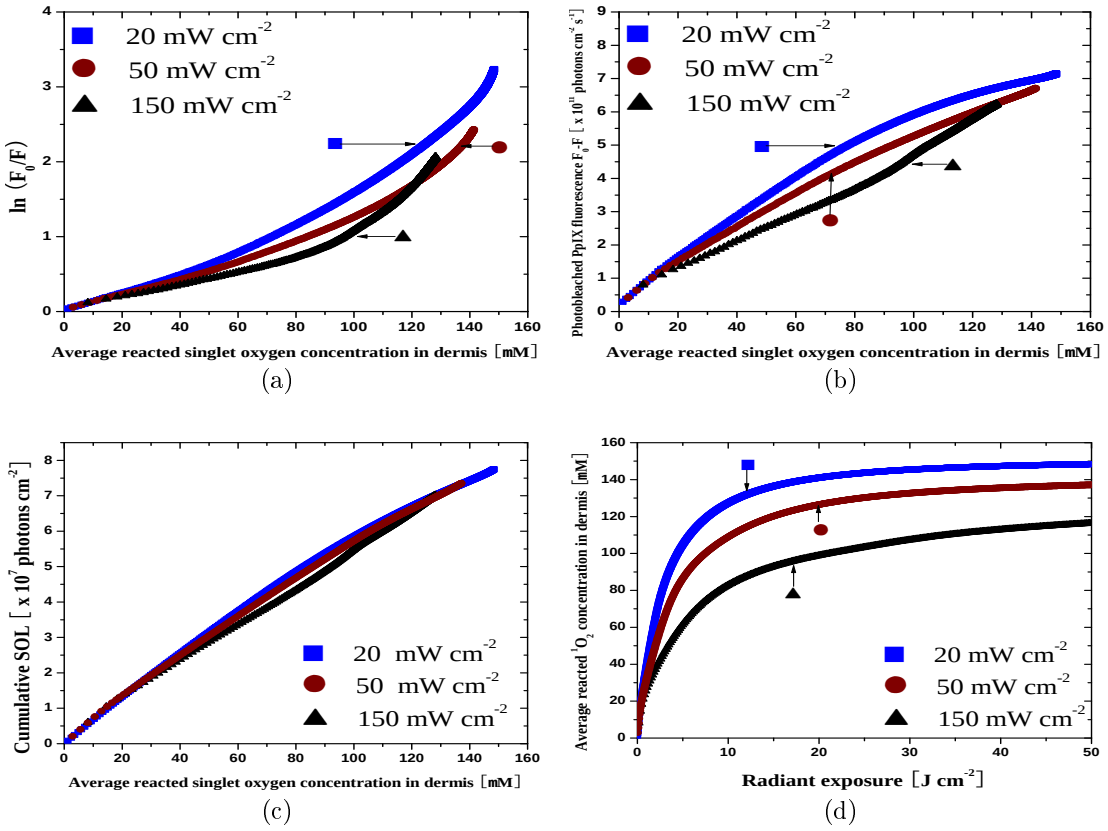

Figure 4.20: Comparison of the dose metrics for different irradiance: (a) FFBM, (b) AFBM, (c) CSOL and (d) average reacted $^1O_2$ concentration in dermis.

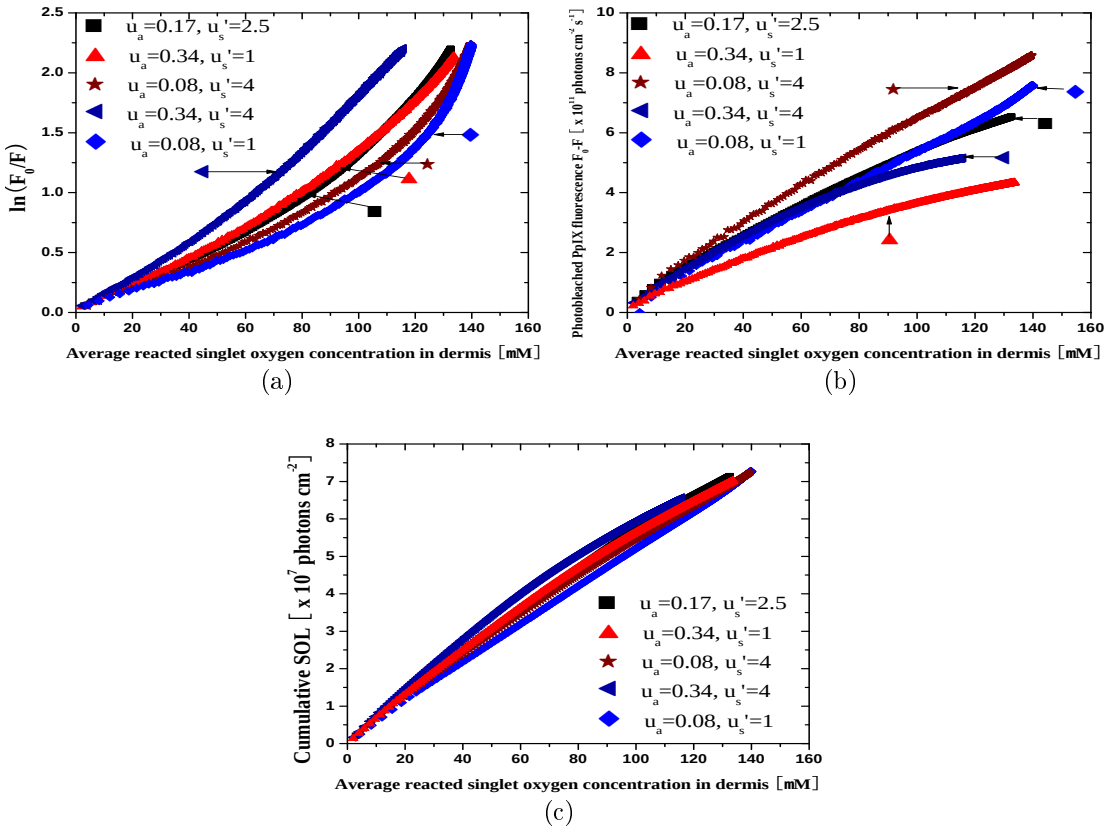

Figure 4.21: Comparison of the dose metrics for different optical properties of the dermis: (a) FFBM, (b) AFBM and (c) CSOL. Total radiant exposure: 30 J cm^{-2} at 50 mW cm^{-2}. Unit of optical properties: mm^{-1}.

Figure 4.22 shows the comparison for varied initial drug concentration and distribution. The initial distributions of PpIX used in the simulations are demonstrated in figure 4.22(d). As shown in figure 4.22(a), the $^1O_2$ 'dose' calculated using the fractional loss of fluorescence signal can be greatly affected by the photosensitizer concentration. The dependence can also be highly nonlinear. Dysart *et al.* (2002) conducted a similar *in vitro* experimental study using DP16 cells with mTHPC, where the correlation of cell survival fraction to the normalized fluorescence signal was examined. The study of Dysart *et al.* (2002) showed that the survival fraction was independent of irradiance, but dependent on the initial sensitizer concentration. Treatments with higher sensitizer concentration produced less fractional loss of fluorescence than those at the lower concentration for the same cell kill. This is consistent with the results in figure 4.22(a). The AFBM approach (figure 4.22(b)) is much more successful - the correlation is almost independent of the PpIX concentration, but does depend on the depth distribution. Overall, the CSOL dose metric is the most robust when the PpIX concentration and distribution are varied.

The slope of the best linear fit to all CSOL curves (figures 4.20(c), 4.21(c) and 4.22(c)) is $5.32\pm0.02\times10^5$ photons cm^{-2} μM^{-1} with the R value of 0.9988. With knowledge of a given SOL detector efficiency and the geometry of the treated area, this tight correlation suggests that it may be possible to estimate the average $^1O_2$ dose in dermis based on the detected SOL photon counts. The linear fit to all of the CSOL results accounts for all but 0.24% of the total variance. By comparison, a linear fit to all of the FFBM data (figures 4.20(a), 4.21(a), 4.22(a)) has a residual variance of 37.7%. The residual variance for a linear fit to all of the AFBM data (figures 4.20(b), 4.21(b), 4.22(b)) is 1.58%.

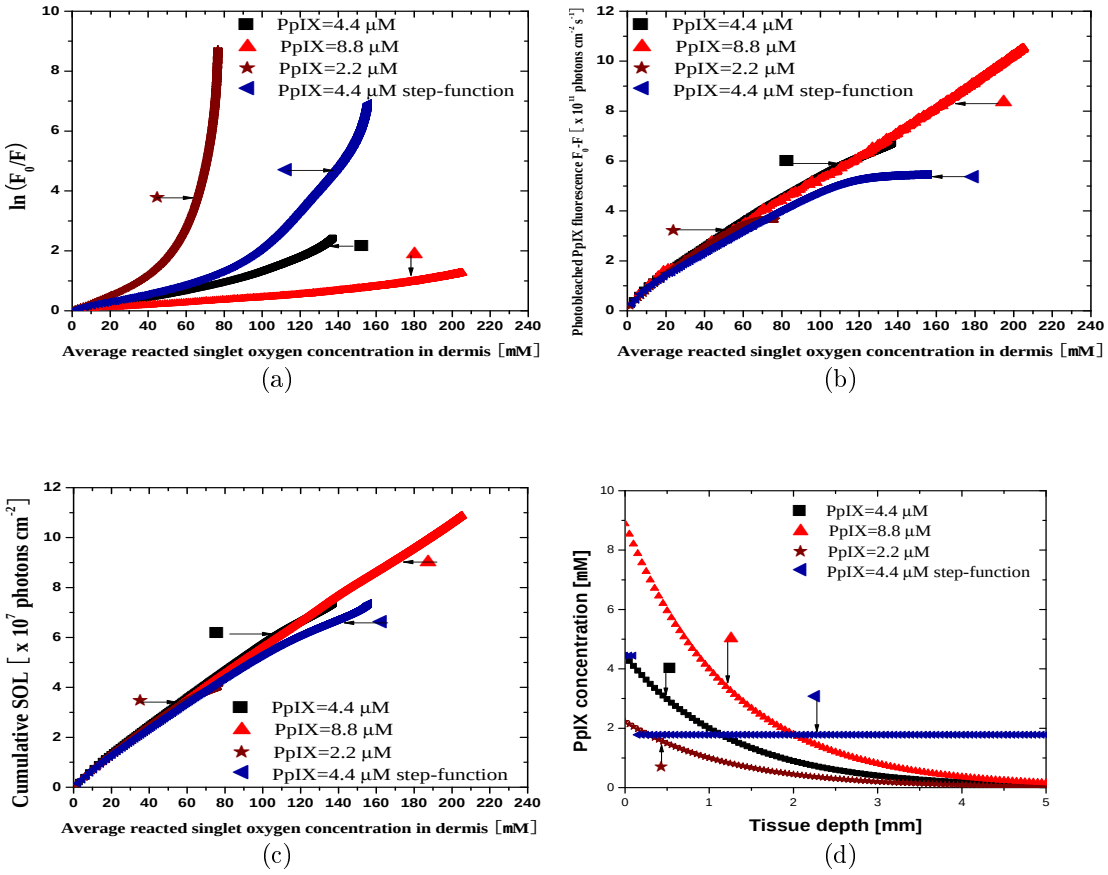

Figure 4.22: Comparison of the dose metrics for different drug concentration and distribution: (a) FFBM, (b) AFBM, (c) CSOL and (d) initial distributions of PpIX. The total radiant exposure: 50 J cm^{-2} at 50 mW cm^{-2}.

4.3.3 Correlation analysis at different depths

Given the better performance of AFBM and CSOL demonstrated above, the correlations of the signals to the reacted $^1O_2$ production at five specific depths (0, 0.2, 0.5, 1 and 2 mm) were examined for these two metrics. Ideally, the relationship should be linear at all depths so that the dose metric could be used to deliver a minimum singlet-oxygen dose to a critical depth, e.g. the base of a cancerous lesion. Figure 4.23 shows the comparisons at irradiance of 20, 50 and 150 mW cm^{-2}. In general, these depth-dependent correlations have similar features for the AFBM and CSOL metrics. The horizontal lines in figure 4.23 (b), (d) and (f) show the radiant exposures (J cm^{-2}) to indicate the progress of PDT treatment.

At all irradiances, the model indicates that singlet-oxygen dose at the skin surface reaches a maximum at about 5 J cm^{-2} even though both dose metrics continue to increase. This results from the complete photobleaching of PpIX at the surface. A representative feature due to oxygenation variation during PDT can be seen at depth 0.2 mm. With the assumptions used in our calculation, oxygen consumption by PDT is very quick in this upper layer, as is the reduction in the vascular supply, so that the main oxygen supply is diffusion from air on the surface. However, oxygen has to satisfy the PDT demands in the layers above 0.2 mm first - only the remaining oxygen will diffuse to the underlying tissue. Therefore, singlet-oxygen production at 0.2 mm depth increases at some time during PDT, once more oxygen diffuses from the air. This increase in the availability of oxygen eventually enables PpIX to be bleached away in that layer. As treatment continues, the same process will be repeated in the layer below. For this reason, our model shows that the correlation at 0.2 mm has a dramatic decrease in the slope as the production of $^1O_2$ increases, but then becomes vertical as all PpIX is consumed. At depths of 0.5 mm and greater, this complex behavior is less extreme and a reasonably good linear relationship exists between both dose metrics at the surface and the singlet-oxygen dose at depth.

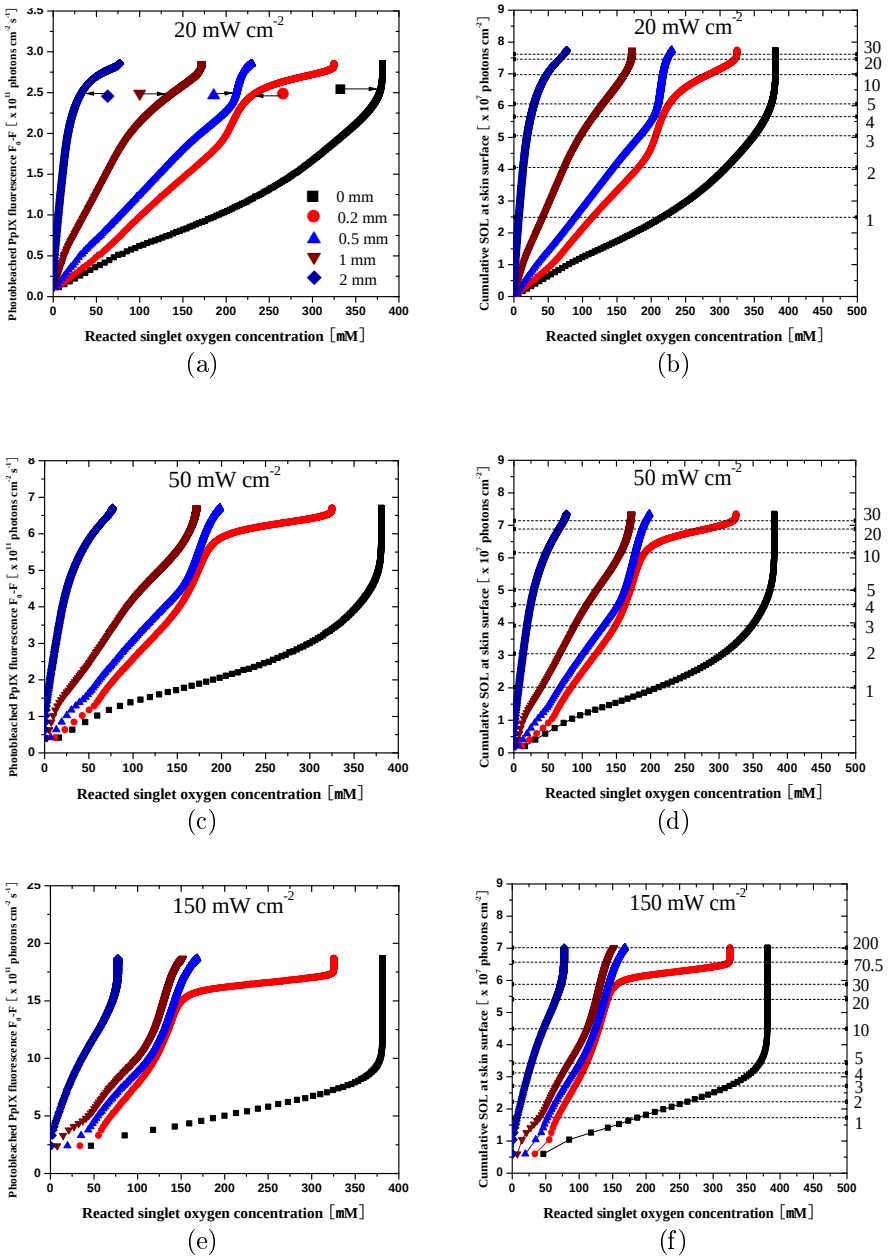

Figure 4.23: Correlation of (a), (c), (e) AFBM and (b), (d), (f) CSOL to the singlet-oxygen dose in a 50 μm layer at depths of 0, 0.2, 0.5, 1 and 2 mm for three different treatment irradiances. Labels on the right-hand coordinate of (b), (d) and (f) are radiant exposure in J cm^{-2}. Labels in (a) are also applied in the same order to the curves in (b) - (f).

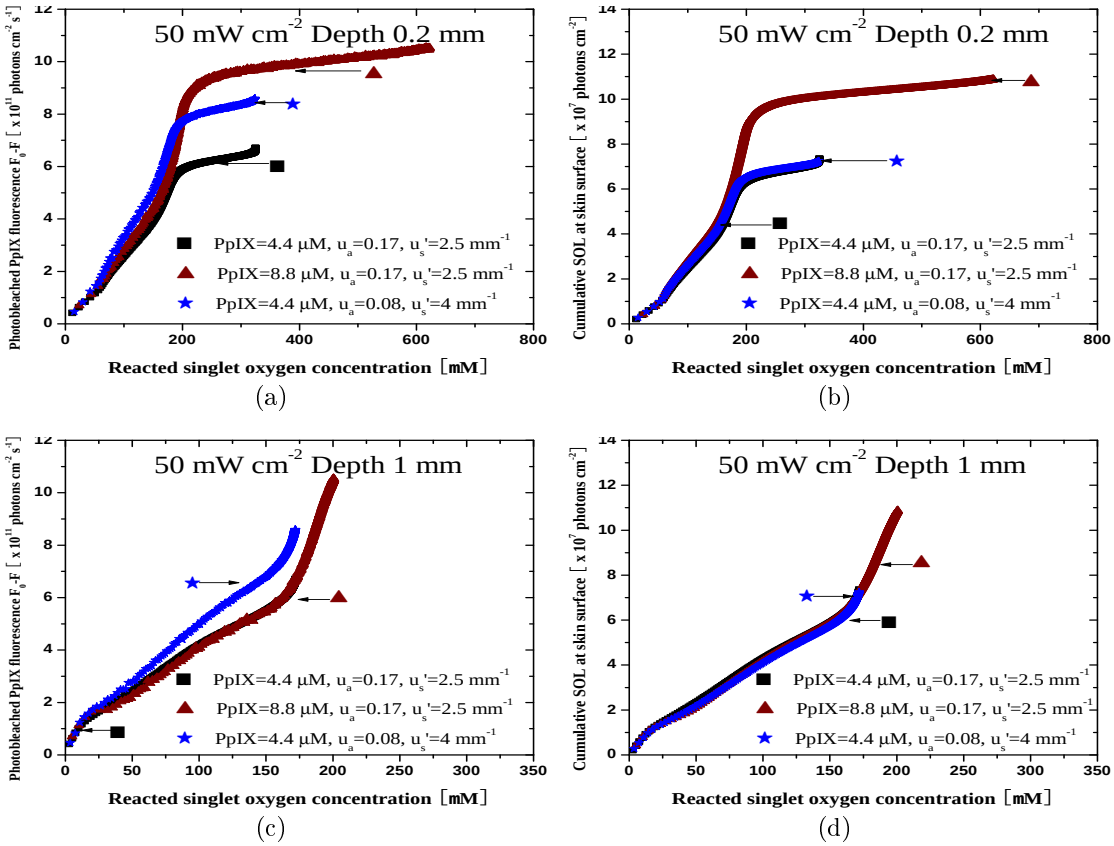

Figure 4.24: Correlation of AFBM and CSOL to the singlet-oxygen dose at depths of 0.2 and 1 mm with varied optical properties in the dermis and different PpIX initial concentration.

Finally, the features observed in figure 4.23 are also examined for different optical properties of the dermis and different initial PpIX concentrations at irradiance of 50 mW cm^{-2}. The results at two representative depths (0.2 and 1 mm) are shown in figures 4.24(a) and (c) for the AFBM and in figures 4.24(b) and (d) for CSOL. At depth 0.2 mm, where the great variation in oxygen concentration occurs, the CSOL metric is influenced only by the initial PpIX concentration and not by the optical properties. In contrast, the AFBM metric is affected by both parameters. At depth 1 mm, the CSOL metric demonstrates no dependence on the varied parameters, and is more robust than the AFBM. Overall, better linear correlations can be expected at greater depths such as 1 mm due to the more consistent availability of oxygen. The CSOL metric is much less dependent upon the varied treatment parameters, especially at greater depth.

4.4 Conclusion

Three PDT dose metrics (FFBM, AFBM and CSOL) were investigated and compared for varied treatment parameters including irradiance, optical properties and initial PpIX concentration and distribution. The correlation of the CSOL metric to the average singlet-oxygen 'dose' in dermis demonstrated the best near-to-linear relation. Compared with the two fluorescence photobleaching dose metrics (FFBM and AFBM), CSOL demonstrated the most robust performance when the treatment parameters were varied. Similar comparisons were performed between the AFBM and CSOL metrics for the singlet-oxygen dose at two representative depths. The CSOL metric shows much less overall dependence on the parameters. Our simulations indicate that the CSOL dose metric is the most robust approach and that it has the potential to be the 'gold standard' clinical tool. Future work is required to demonstrate that this potential can be realized and that CSOL or other methods can be predictive of clinical response.

Acknowledgements

This research has been supported by the Canadian Cancer Society Research Institute.

Bibliography

Boere, I. A., Robinson, D. J., de Bruijn, H. S., Kluin, J., Tilanus, H. W., Sterenborg, H. J. C. M., and de Bruin, R. W. F. (2006). Protoporphyrin IX fluorescence photobleaching and the response of rat Barrett's esophagus following 5-aminolevulinic acid photodynamic therapy. *Photochem. Photobiol.*, **82**, 1638–44.

Chabrier-Rosello, Y., Foster, T. H., Perez-Nazario, N., Mitra, S., and Haidaris, C. G. (2005). Sensitivity of *Candida albicans* germ tubes and biofilms to Photofrin-mediated phototoxicity. *Antimicrob. Agents Chemother.*, **49**, 4288–95.

Cottrell, W. J., Paquette, A. D., Keymel, K. R., Foster, T. H., and Oseroff, A. R. (2008). Irradiance-dependent photobleaching and pain in δ-aminolevulinic acid-photodynamic therapy of superficial basal cell carcinomas. *Clin. Cancer Res.*, **14**, 4475–4483.

Crilly, R. J., Cheong, W., Wilson, B., and Spears, J. R. (1997). Forward-adjoint fluorescence model: Monte Carlo integration and experimental validation. *Applied Optics*, **36**, 6513–19.

Dysart, J. S., Patterson, M. S., Farrell, T. J., and Singh, G. (2002). Relationship between mTHPC fluorescence photobleaching and cell viability during *in vitro* photodynamic treatment of DP16 cells. *Photochem. Photobiol.*, **75**, 289–295.

Dysart, J. S., Singh, G., and Patterson, M. S. (2005). Calculation of singlet oxygen dose from photosensitizer fluorescence and photobleaching during mTHPC photodynamic therapy of MLL cells. *Photochem. Photobiol.*, **81**, 196–205.

Farrell, T. J., Wilson, B. C., Patterson, M. S., and Olivo, M. C. (1998). Comparison of the *in vivo* photodynamic threshold dose for Photofrin, Mono- and Tetrasulfonated Aluminum Phthalocyanine using a rat liver model. *Photochem. Photobiol.*, **68**, 394–399.

Finlay, J. C., Mitra, S., Patterson, M. S., and Foster, T. H. (2004). Photobleaching kinetics of Photofrin *in vivo* and in multicell tumor spheroids indicate two simultaneous bleaching mechanisms. *Phys. Med. Biol.*, **49**, 4837–60.

Georgakoudi, I. and Foster, H. T. (1998). Singlet oxygen- versus nonsinglet oxygen-mediated mechanisms of sensitizer photobleaching and their effects on photodynamic dosimetry. *Photochem. Photobiol.*, **67**, 612–625.

Hudson, J. A. and Cater, D. B. (1964). An analysis of factors affecting tissue oxygen tension. In *Proc. R. Soc. London*, volume 161 of *B*, pages 247–74. The Royal Society.

Josefsen, L. B. and Boyle, R. W. (2008). Photodynamic therapy and the development of metal-based photosensitisers. *Met Based Drugs.*, **v.2008**.

Keene, J. P., Kessel, D., Land, E. J., Redmond, R. W., and Truscott, T. G. (1986). Direct detection of singlet oxygen sensitized by Haematoporphyrin and related compounds. *Photochem. and Photobiol.*, **43**, 117–20.

Laubach, H. J., Chang, S. K., Lee, S., Rizvi, I., Zurakowski, D., Davis, S. J., Taylor, C. R., and Hasana, T. (2008). *In-vivo* singlet oxygen dosimetry of clinical 5-aminolevulinic acid photodynamic therapy. *J. Biomed. Opt.*, **13**.

Liu, B., Farrell, T. J., Patterson, M. S., Jarvi, M. T., and Wilson, B. C. (2009). A Monte Carlo model of detected singlet oxygen luminescence and photosensitizer fluorescence during ALA-PDT of skin. In *Proc. of SPIE*, volume 7380, pages 73806W 1–11.

Liu, B., Farrell, T. J., and Patterson, M. S. (2010). A dynamic model for ALA-PDT of skin: simulation of temporal and spatial distributions of ground-state oxygen, photosensitizer and singlet oxygen. *Phys. Med. Biol.*, **55**, 5913–32.

Mitra, S. and Foster, F. H. (2005). Photophysical parameters, photosensitizer retention and tissue optical properties completely account for the higher photodynamic efficacy of meso-tetra-hydroxyphenyl-chlorin vs Photofrin. *Photochem. Photobiol.*, **81**, 849–59.

Niedre, M. J., Yu, C. S., Patterson, M. S., and Wilson, B. C. (2005). Singlet oxygen luminescence as an *in vivo* photodynamic therapy dose metric: validation in normal mouse skin with topical amino-levulinic acid. *Br. J. Cancer*, **92**, 298–304.

Robinson, D. J., de Bruijn, H. S., van der Veen, N., Stringer, M. R., Brown, S. B., and Star, W. M. (1998). Fluorescence photobleaching of ALA-induced protoporphyrin IX during photodynamic therapy of normal hairless mouse skin: the effect of light dose and irradiance and the resulting biological effect. *Photochem. Photobiol.*, **67**, 140–9.

Salomatina, E., Jiang, B., Novak, J., and Yaroslavsky, A. N. (2006). Optical properties of normal and cancerous human skin in the visible and near-infrared spectral range. *J. Biomed. Opt.*, **11**.

Stücker, M., Struk, A., Altmeyer, P., Herde, M., Baumgartl, H., and Lubbers, D. W. (2002). The cutaneous uptake of atmospheric oxygen contributes significantly to the oxygen supply of human dermis and epidermis. *J. Physiol.*, **538**, 985–94.

Tschen, E. H., Wong, D. S., Pariser, D. M., Dunlap, F. M., Houlihan, A., and Ferdon, M. B. (2006). Photodynamic therapy using aminolaevulinic acid for patients with nonhyperkeratotic actinic keratoses of the face and scalp: phase IV multicentre clinical trail with 12-month follow up. *Br. J. Dermatol.*, **155**, 1262–9.

Valentine, R. M., Brown, C. T. A., Moseley, H., Ibbotson, S., and Wood, K. (2011). Monte Carlo modeling of *in vivo* protoporphyrin IX fluorescence and singlet oxygen production during photodynamic therapy for patients presenting with superficial basal cell carcinomas. *J. Biomed. Opt.*, **16**, 048002.

Wang, K. K., Mitra, S., and Foster, T. H. (2007). A comprehensive mathematical model of microscopic dose deposition in photodynamic therapy. *Med. Phys.*, **34**, 282–93.

Wang, K. K., Finlay, J. C., Busch, T. M., Hahn, S. M., and Zhu, T. C. (2010). Explicit dosimetry for photodynamic therapy macroscopic singlet oxygen modeling. *J. Biophoton.*, **3**, 304–318.

Wang, L., Jacques, S. L., and Zheng, L. (1995). MCML - Monte Carlo modeling of light transport in multi-layered tissues. *Comput. Meth. Prog. Bio.*, **47**, 131–46.

Wang, L. V., Nordquist, R. E., and Chen, W. R. (1997). Optimal beam size for light delivery to absorption-enhanced tumors buried in biological tissues and effect of multiple-beam delivery: a Monte Carlo study. *Appl. Optics*, **36**, 8286–91.

Wang, W. (2005). Oxygen partial pressure in outer layers of skin: simulation using three-dimensional multilayered models. *Microcirculation*, **12**, 195–207.

Wilson, B. C. and Patterson, M. S. (2008). The physics, biophysics and technology of photodynamic therapy. *Phys. Med. Biol.*, **53**, R61–R109.

Wolf, E. P., Rieger, E., and Kerl, H. (1993). Topical photodynamic therapy with endogenous porphyrins after application of 5-aminolevulinic acid: An alternative treatment modality for solar keratoses, superficial squamous cell carcinoma, and basal cell carcinomas? *J. AM. Acad. Dermatol.*, **28**, 17–21.

Chapter 5

Paper IV - Comparison of photodynamic therapy with different excitation wavelengths using a dynamic model of ALA-PDT of human skin

Baochang Liu, Thomas J. Farrell and Michael S. Patterson

Department of Medical Physics and Applied Radiation Sciences, McMaster University, 1280 Main Street West, Hamilton, Ontario, Canada, L8S 4K1
and
Department of Medical Physics, Juravinski Cancer Centre, 699 Concession Street, Hamilton, Ontario, Canada, L8V 5C2

Accepted [June 21st, 2012] by Journal of Biomedical Optics

Introduction to paper IV

This chapter presents the study continued from chapters 2 and 3. The results in the previous two chapters are using a single excitation wavelength (633 nm). The study in this chapter expands to two commonly used treatment wavelengths (523 and 405 nm). Both the time-resolved depth-dependent distributions of the PDT components and comparison of different PDT dose metrics will be discussed for red, green and blue excitation light sources.

I performed all the simulations, analyzed the results, and wrote the manuscript. Dr. Patterson supervised my work, contributed to the results discussion, and edited my manuscript. Dr. Farrell gave me suggestions on fixing any error in the model.

Contents of Paper IV

Abstract

Different wavelength light sources are used in photodynamic therapy of the skin to treat different conditions. Clinical studies show inconsistent results for the effectiveness of ALA-PDT performed at different wavelengths. In order to understand the effect of treatment wavelength, a theoretical study was performed to calculate time-resolved depth-dependent distributions of PDT components including ground-state oxygen, sensitizer, and reacted singlet oxygen for different treatment wavelengths (405, 523 and 633 nm) using a numerical model of ALA-PDT of human skin. This model incorporates clinically relevant features of the PDT process including light attenuation, photobleaching, oxygen consumption and diffusion as well as tissue perfusion. The calculations show that the distributions of these quantities are almost independent of the treatment wavelength to a depth of about 1 mm. In this surface region, PDT-induced hypoxia is the dominant process. At greater depths, the production of singlet oxygen is governed by the penetration of the treatment light. Two noninvasive PDT dosimetry approaches: the cumulative singlet oxygen luminescence (CSOL) and the fractional fluorescence bleaching metric (FFBM), were investigated and compared for all three wavelengths. Although CSOL was more robust, both metrics provided correlations with singlet oxygen dose in the upper dermis that were almost independent of treatment wavelength. This relationship breaks down at greater depths because light penetration depends on wavelength.
Keywords: Photodynamic therapy, ALA, dosimetry, fluorescence, photobleaching, singlet oxygen luminescence

5.1 Introduction

Photodynamic therapy (PDT) has emerged as an important treatment method for various diseases. Topical ALA-induced protoporphyrin IX (PpIX) PDT is widely used to manage a variety of malignant and non-malignant skin conditions. During ALA-PDT, the light-activatable photosensitizer PpIX is endogenously synthesized after the administration of the prodrug 5-aminolevulinic acid (ALA). Light exposure then produces singlet oxygen ($^1O_2$) that causes clinical outcomes.

The efficiency of PDT can be determined by the availability of tissue oxygen, the penetration depth of excitation light into tissue and the absorption of the photosensitizer. During ALA-PDT treatment, excitation light sources at different wavelengths are often used for different treatment purposes and conditions. PpIX has absorption peaks at about 405 nm in the Soret Band, and at about 505, 540, 580 and 630 nm in

the Q-Band (Fritsch *et al.* 1997). A short wavelength excitation light can be used to maximize the absorption of PpIX, to limit penetration depth and to avoid exposing deeper healthy tissue. Narrow-band blue light (405 - 420 nm) was first approved by the US FDA (Food and Drug Administration) for acne vulgaris treatment, and newer generations of this blue light system have been produced (Gold 2007). Red light (633 nm) with its deeper penetration depth is usually used to treat superficial basal cell carcinoma (sBCC) (Cottrell *et al.* 2008).

Studies have been conducted to investigate ALA-PDT efficacy at different wavelengths ranging from 405 - 420 nm (blue light) and 635 nm (red light) (Gold and Goldman 2004). Green light was also evaluated to compare ALA-PDT efficacy. An early study found that green light (543 - 548 nm) was less painful than red light (630 nm), but equally effective, for the treatment of facial solar keratoses (Fritsch *et al.* 1997). On the other hand, another clinical ALA-PDT study found that green light (540±15 nm) is less effective than red light (630±15 nm) in the treatment of Bowen's disease (Morton *et al.* 2000). These results are inconsistent for different diseases, which may imply that treatment wavelength is not the only cause of different therapeutic outcomes of ALA-PDT.

Many of these studies were performed to evaluate the clinical response to determine the optimal wavelength for a specific type of PDT treatment. To our knowledge, no theoretical studies have been conducted using realistic clinical treatment parameters to investigate the fundamental differences in ALA-PDT of the skin at different excitation wavelengths. In a recent study, Nielsen *et al.* (2005) used a mathematical model to investigate the effects of oxygen depletion on the efficiency of ALA-PDT at different depths at different excitation wavelengths. These authors calculated the PDT efficacy as the product of the calculated relative fluence rate in skin and the measured excitation spectrum of PpIX, but did not take into account the effects of oxygen supply and consumption. An accurate simulation of the production and the distribution of singlet oxygen may be a better way to understand PDT effects.

The PDT process is complicated, but insight can be provided by a dynamic model for ALA-PDT of human skin recently introduced by Liu *et al.* (2010). The temporal and spatial distributions of the essential PDT parameters including tissue oxygen, photosensitizer and singlet oxygen were investigated for PDT using red excitation light. Different PDT dosimetry approaches were also compared at the same excitation wavelength (Liu *et al.* 2012). The objective of the present study is to use this model to examine and compare the distributions of the three PDT parameters and different dose metrics for PDT at different wavelengths. The studied wavelengths are 405, 523 and 633 nm. The 405 nm wavelength representing blue light is close to the maximum absorption of PpIX. The 633 nm light is commonly used in clinics. Green light at 523 nm rather than 540 nm was chosen as a theoretical guide to a pilot study of singlet oxygen luminescence (SOL) detection on normal human skin using a

laser source at this wavelength for its suitable characteristics for time-resolved SOL measurement (Jarvi *et al.* 2006). With these wavelengths, the overall influence of the greater absorption coefficient of PpIX and limited excitation light penetration depth at shorter wavelength on the depth-resolved distribution of the reacted singlet oxygen will be evaluated. This can be useful to understand the choice of excitation light source for different clinical treatment targets.

5.2 Theory and method

5.2.1 Description of the model

The dynamic one-dimensional ALA-PDT model used a semi-infinite three-layer tissue consisting of epidermis, dermis and subcutaneous fat layers to represent normal human skin. Each layer has uniform optical properties. The optical properties at the wavelengths of interest are shown in table 5.11. The excitation light fluence distribution in tissue is simulated using the standard Monte Carlo (MC) method. The adjoint MC method was used to calculate the PpIX fluorescence and singlet oxygen luminescence signals escaping from the skin surface.

Table 5.11: Optical properties of normal human skin. Data were extracted from Salomatina *et al.* (2006). The excitation wavelengths are 405, 523 and 633 nm, and the photosensitizer fluorescence and singlet-oxygen phosphorescence wavelengths are 705 and 1270 nm, respectively. μ_a is the absorption coefficient; μ_s' is the reduced scattering coefficient (units mm^{-1}). The refractive index is 1.4 for all three layers.

		405 (nm)		523 (nm)		633 (nm)		705 (nm)		1270 (nm)	
Tissue	Thickness (mm)	μ_a	μ_s'	μ_a	μ_s'	μ_a	μ_s'	μ_a	μ_s'	μ_a	μ_s'
Epidermis	0.1	1.27	10.4	0.5	6	0.25	5.0	0.25	4.0	0.05	2.5
Dermis	2.5	0.87	7.4	0.3	4	0.17	2.5	0.15	2.5	0.1	1.6
Sub-Q	25	1.61	4.95	0.45	3	0.12	2.5	0.12	2.3	0.1	1.5

The model incorporates vertical (i.e. perpendicular to the skin surface) ground-state oxygen diffusion due to its spatial concentration gradient. Tissue oxygen can be supplied by diffusion from air and by perfusion from local blood vessels. The perfusion rate was hypothesized to be dependent on reacted singlet-oxygen ($^1O_2$) dose so that perfusion was reduced commensurate with PDT-induced vascular damage.

In the model, oxygen consumption consists of both metabolic consumption (Γ_{met}) described by the Michaelis-Menten relation and PDT consumption (Γ_{PDT}). The PDT oxygen consumption and the ground-state photosensitizer concentration are found by solving a set of differential equations describing the possible photochemical reaction pathways during PDT.

The final two differential equations for updating the concentration of ground-state PpIX and oxygen partial pressure at each depth after delivering a light dose increment are shown in equations (5.86) and (5.87). In equation (5.87), oxygen concentration is expressed by the product of oxygen partial pressure (pO_2) P and solubility coefficient α using Henry's law because continuity in pO_2 and in the oxygen flux are boundary conditions at depth z. The first term on the right-hand side of equation (5.87) represents Γ_{PDT}. The second term is the metabolic oxygen consumption where $\Gamma_{\text{met}}^{\max}$ is the initial maximum metabolic consumption rate of human skin in the steady state, and k_{50} is the $^3O_2$ concentration at which Γ_{met} is half of $\Gamma_{\text{met}}^{\max}$. The third term represents the oxygen supply from blood vessels, where K_z is a sigmoidal irradiance-dependent reacted $^1O_2$ dose response and D_{50} is the $^1O_2$ dose that causes a 50% reduction in initial K value. The fourth term represents the tissue oxygen diffusion in the vertical direction, where D is the tissue oxygen diffusion coefficient, Δz is the depth grid increment and the subscripts '$-$' and '$+$' refer to the depths above and below z respectively. More detailed description of this model and the derivation of these equations can be found elsewhere (Liu *et al.* 2010).

$$\begin{aligned}
\frac{\mathrm{d}\left[\mathrm{S}_0\right]_z}{\mathrm{d}t} &= -\dot{F}_{\text{ex}}\left[\mathrm{S}_0\right]_z \frac{k_{\text{ta}}\left[\mathrm{A}\right]/k_{\text{ot}}}{k_{\text{p}}/k_{\text{ot}} + k_{\text{ta}}\left[\mathrm{A}\right]/k_{\text{ot}} + \alpha_z \mathrm{P}_z} \\
&\quad \times \left[\phi_{\text{t}}\frac{\sigma}{h\nu} + \frac{\frac{k_{\text{os}}}{k_{\text{oa}}[\mathrm{A}]}}{k_{\text{ta}}\left[\mathrm{A}\right]/k_{\text{ot}}}\beta'_{\text{PDT}}\left(\left[\mathrm{S}_0\right]_z + \delta\right)\alpha_z \mathrm{P}_z\right], \qquad (5.86) \\
\alpha_z\frac{\mathrm{dP}_z}{\mathrm{d}t} &= -\dot{F}_{\text{ex}}\left[\mathrm{S}_0\right]_z \beta'_{\text{PDT}}\left[1 + \frac{k_{\text{os}}}{k_{\text{oa}}\left[\mathrm{A}\right]}\left(\left[\mathrm{S}_0\right]_z + \delta\right)\right]\frac{\alpha_z \mathrm{P}_z}{k_{\text{p}}/k_{\text{ot}} + \frac{k_{\text{ta}}[\mathrm{A}]}{k_{\text{ot}}} + \alpha_z \mathrm{P}_z} \\
&\quad -\Gamma_{\text{met}}^{\max}\frac{\alpha_z \mathrm{P}_z}{k_{50} + \alpha_z \mathrm{P}_z} + K_z\left(\left[{}^3\mathrm{O}_2\right]_{\text{v}} - \alpha_z \mathrm{P}_z\right) \\
&\quad + \frac{D_-\alpha_-\left(\mathrm{P}_{z-\Delta z} - \mathrm{P}_z\right) - D_+\alpha_+\left(\mathrm{P}_z - \mathrm{P}_{z+\Delta z}\right)}{\left(\Delta z\right)^2}, \qquad (5.87)
\end{aligned}$$

where :

$$\beta'_{\text{PDT}} = S_\Delta \phi_{\text{t}}\frac{\sigma}{h\nu}\frac{1}{\frac{k_{\text{d}}}{k_{\text{oa}}[\mathrm{A}]} + 1}. \qquad (5.88)$$

In the model, the instantaneous production rate of $^1O_2$ at each depth is calculated via equation (5.89), where I_{a} is photon absorption rate as defined in Liu *et al.* (2010).

The emission signals on the skin surface are calculated using equations (5.90) and (5.91),

$$[^1\dot{\mathrm{O}}_2] = I_\mathrm{a}\Phi_\mathrm{D}\frac{[^3\mathrm{O}_2]}{k_\mathrm{p}/k_\mathrm{ot} + \frac{k_\mathrm{ta}[\mathrm{A}]}{k_\mathrm{ot}} + [^3\mathrm{O}_2]}\,, \tag{5.89}$$

$$\dot{\mathrm{E}}_\mathrm{m705} = \int_0^\infty \dot{F}_\mathrm{ex}(z)\mu_{a,\mathrm{d}}(z)\phi_\mathrm{f}F_{\mathrm{em}_{705}}(z)C_\mathrm{r}\mathrm{d}z\,, \tag{5.90}$$

$$\dot{\mathrm{E}}_\mathrm{m1270} = \int_0^\infty [^1\dot{\mathrm{O}}_2](z)\phi_\mathrm{d}F_{\mathrm{em}_{1270}}(z)C_\mathrm{r}\mathrm{d}z\,, \tag{5.91}$$

where $\dot{F}_\mathrm{ex}(z)$ and $F_\mathrm{em}(z)$ are the fluence rate and relative fluence at the excitation and corresponding emission wavelengths respectively; $\mu_{a,\mathrm{d}}(z)$ is the absorption coefficient of PpIX; ϕ_f, ϕ_d are the PpIX fluorescence and $^1\mathrm{O}_2$ luminescence quantum yields, and C_r is an empirical scaling factor derived from the adjoint Monte Carlo simulations (Liu *et al.* 2009).

5.2.2 Treatment simulations

The simulations were performed with optical properties shown in table 5.11 at excitation wavelengths: 405 nm (blue), 523 nm (green) and 633 nm (red). The treatment irradiance was 20 mW cm^{-2}. Total light exposure was 30 J cm^{-2}. The initial PpIX concentration was 4.4 μM on the skin surface and decreased exponentially with depth with decay constant 0.8 mm^{-1}. The other parameters used in the simulations are listed in table 5.12.

Table 5.12: Photophysical and physiological parameters. ϵ_{PpIX} and β'_{PDT} values correspond to wavelengths of 633, 523 and 405 nm. D=0.2×10^{-5} $\mathrm{cm^2 s^{-1}}$ was used only in the top 50 μm stratum corneum layer, and D=1.25 ×10^{-5} $\mathrm{cm^2 s^{-1}}$ was used for other layers.

Parameters	Values	Reference	Units
$(k_{\mathrm{os}}/k_{\mathrm{oa}}\,[\mathrm{A}])$	90	Georgakoudi and Foster (1998)	$\mathrm{M^{-1}}$
$(k_{\mathrm{p}}/k_{\mathrm{ot}})$	4	Liu *et al.* (2010)	μM
$(k_{\mathrm{ta}}\,[\mathrm{A}]\,/k_{\mathrm{ot}})$	0		μM
$(\Gamma_{\mathrm{met}}^{\mathrm{max}})$	1.5	Liu *et al.* (2010)	$\mu\mathrm{M\ s^{-1}}$
δ	128	Liu *et al.* (2010)	μM
k_{50}	0.5	Wang *et al.* (2007)	μM
K_0	0.0370		$\mathrm{s^{-1}}$
$\left[{}^3\mathrm{O}_2\right]_{\mathrm{v}}$	80		μM
a	0.08		$\mu\mathrm{M^{-1}}$
D_{50}	191	Liu *et al.* (2010)	μM
D	0.2/1.25 ×10^{-5}	Liu *et al.* (2010)	$\mathrm{cm^2 s^{-1}}$
α	1.25×10^{-6}		$\mathrm{M\ mmHg^{-1}}$
ϵ_{PpIX}	3000/10000/129000		$\mathrm{M^{-1}cm^{-1}}$
β'_{PDT}	0.021/0.058/0.5805		$\mathrm{mJ^{-1}cm^2}$
ϕ_{f}	0.05		
ϕ_{d}	10^{-8}		
ϕ_{t}	0.83	Josefsen and Boyle (2008)	
Φ_{D}	0.57	Keene *et al.* (1986)	

5.3 Results and Discussion

5.3.1 Temporal and spatial distributions of the PDT quantities

Figure 5.25 shows ground-state oxygen perfusion rate versus depth as radiant exposure increases at all three wavelengths. As discussed in more detail in Liu *et al.* (2010), a reduction in oxygen perfusion from local blood vessels during treatment was necessary to produce PpIX fluorescence photobleaching results in agreement with clinical measurements reported by Cottrell *et al.* (2008). Early in the treatment (such as 1.2 J cm^{-2}), the reduction in perfusion is the greatest for blue light due to the greatest absorption of PpIX at this wavelength as shown in table 5.12. However, at 30 J cm^{-2}, there is little difference in the PDT-induced vascular responses.

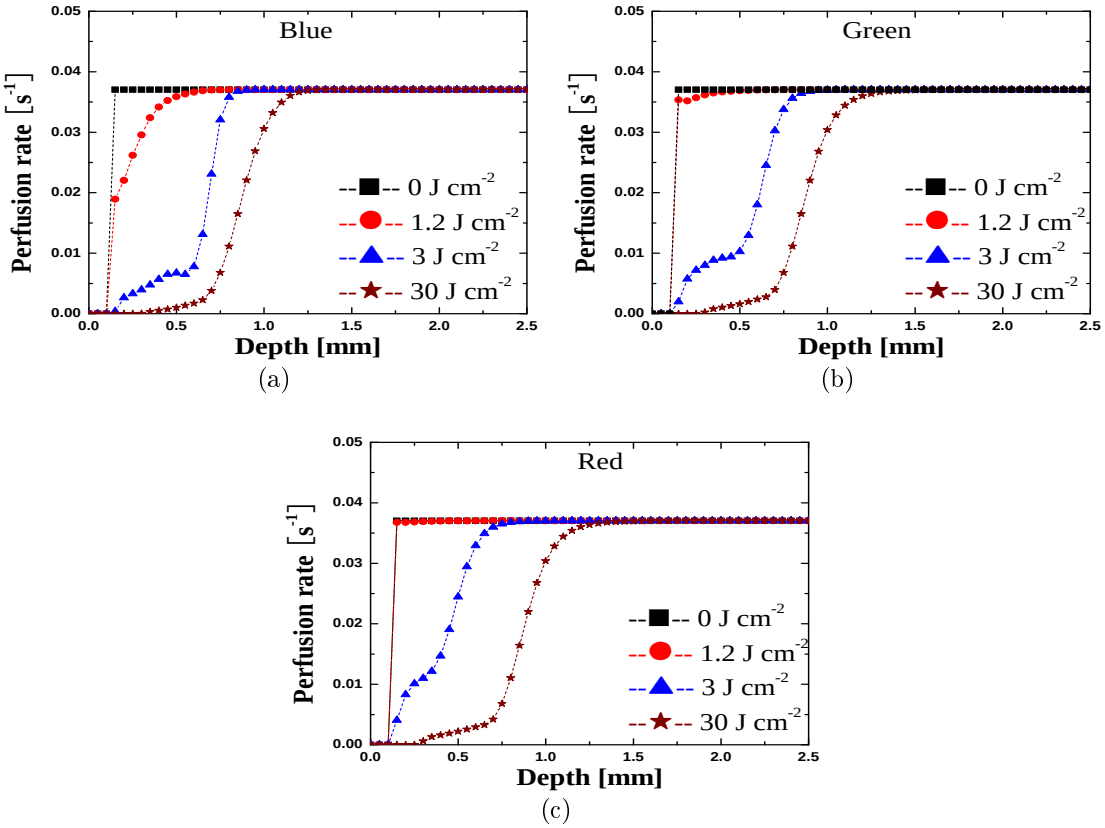

Figure 5.25: The depth-resolved distribution of oxygen perfusion supply.

Figures 5.26(a), 5.26(c) and 5.26(e) show the time-resolved depth distributions of ground-state oxygen at the three wavelengths, and figures 5.26(b), 5.26(d) and 5.26(f) present the corresponding distribution of PpIX. Oxygen in the upper dermis (above 0.5 mm) is rapidly consumed after the delivery of light. This consumption during early PDT is fastest with blue light because of the PpIX absorption coefficient (see table 5.12). The region of induced hypoxia gradually spreads to about 1 mm depth at all three wavelengths, and the distributions of tissue oxygen after 30 J cm^{-2} light exposure at the three wavelengths are almost the same.

As shown in figure 5.26, PpIX near the skin surface is bleached fastest at 405 nm. Due to the induction of hypoxia in the upper dermis, PpIX remains at the end of treatment. Up to 1 mm depth, more PpIX is preserved at longer wavelength. At depths beyond 1 mm, the amount of remaining PpIX is the greatest at 405 nm at 30 J cm^{-2}. As shown in figure 5.27, this reflects the limited penetration of treatment light at 405 nm.

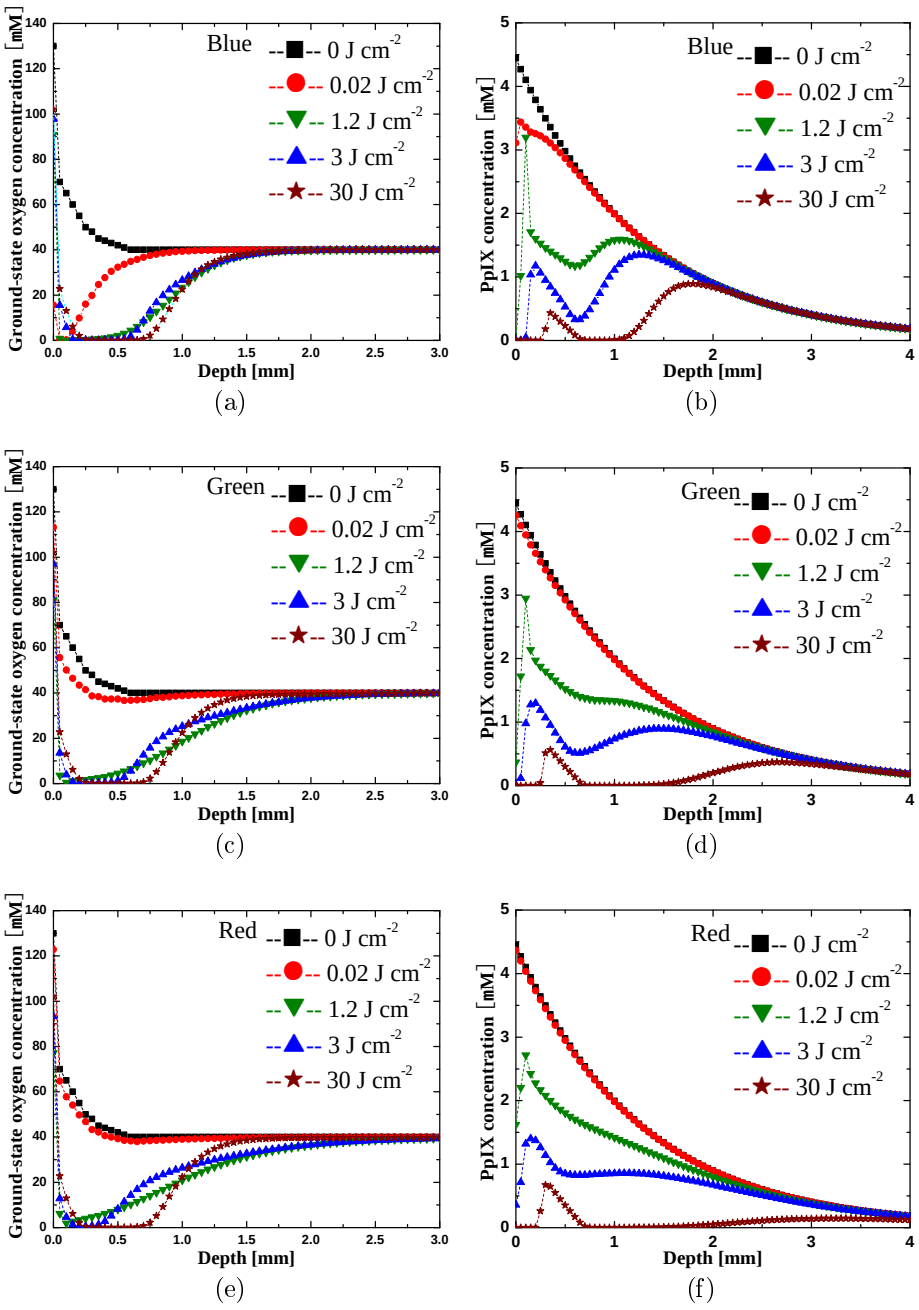

Figure 5.26: Depth-resolved distributions of ground state oxygen and PpIX.

Figure 5.27 shows the normalized excitation light fluence rate versus tissue depth for all three wavelengths. The horizontal line indicates a reduction to $1/e$ for comparison of the penetration depths at the three wavelengths. Fluence rate was averaged over the entire treatment at each wavelength. In the model, fluence rate was updated after each increment of delivered light exposure, and the bleaching of PpIX causes small changes in the light absorption coefficients. This change is small compared with the tissue absorption coefficient, so the light fluence rate within tissue did not vary significantly during the treatment. These results are not shown in this paper. The penetration depths with currently used optical properties are about 0.25, 0.65 and 1 mm for blue, green and red light respectively.

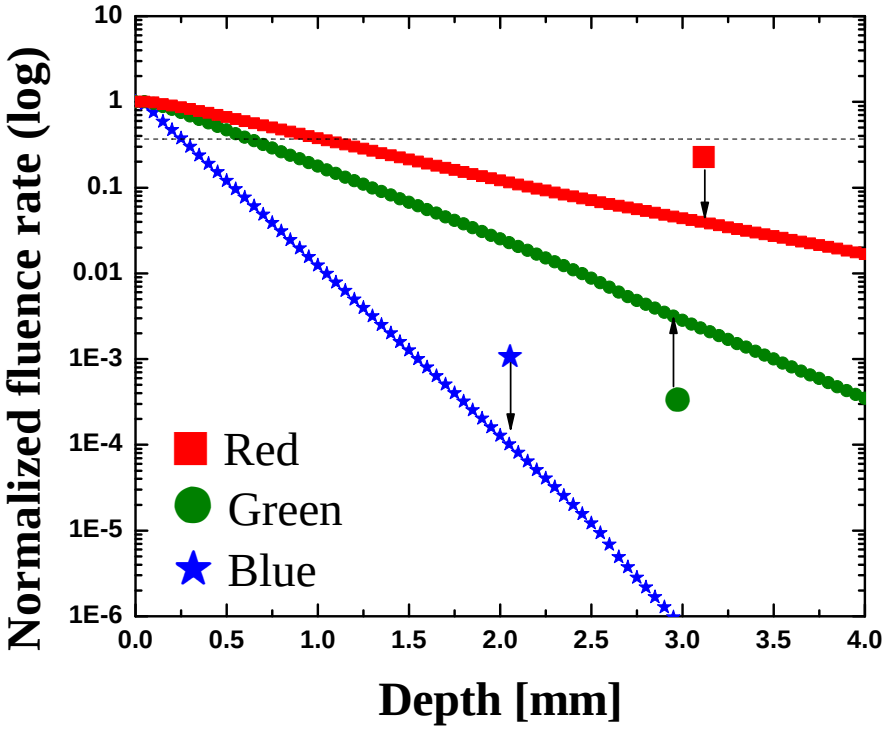

Figure 5.27: Comparison of normalized fluence rate at the three treatment wavelengths.

Figures 5.28(a), 5.28(b) and 5.28(c) show the evolution of the depth-distribution of reacted singlet oxygen during PDT at the three wavelengths. The biological effect of PDT is expected to be directly related to this quantity. The initial production rate of $^1O_2$ is the highest at 405 nm, but the total production of $^1O_2$ on the skin surface at the end of treatment is the same for all three wavelengths. The reduction in singlet oxygen production rate due to oxygen depletion and PpIX photobleaching in the epidermis and upper dermis can be observed at all wavelengths. Figure 5.28(d) compares the reacted $^1O_2$ concentrations at the beginning and the end of PDT for the three wavelengths. Up to a depth of about 1 mm, the amount of reacted singlet oxygen at the end of treatment is practically independent of wavelength. Although the light fluence rate over this depth range is very different at the three wavelengths, the production of singlet oxygen is limited by hypoxia and PpIX photobleaching. At greater depth, sufficient oxygen and PpIX remain, so the production rate of $^1O_2$ is proportional to the treatment light fluence rate.

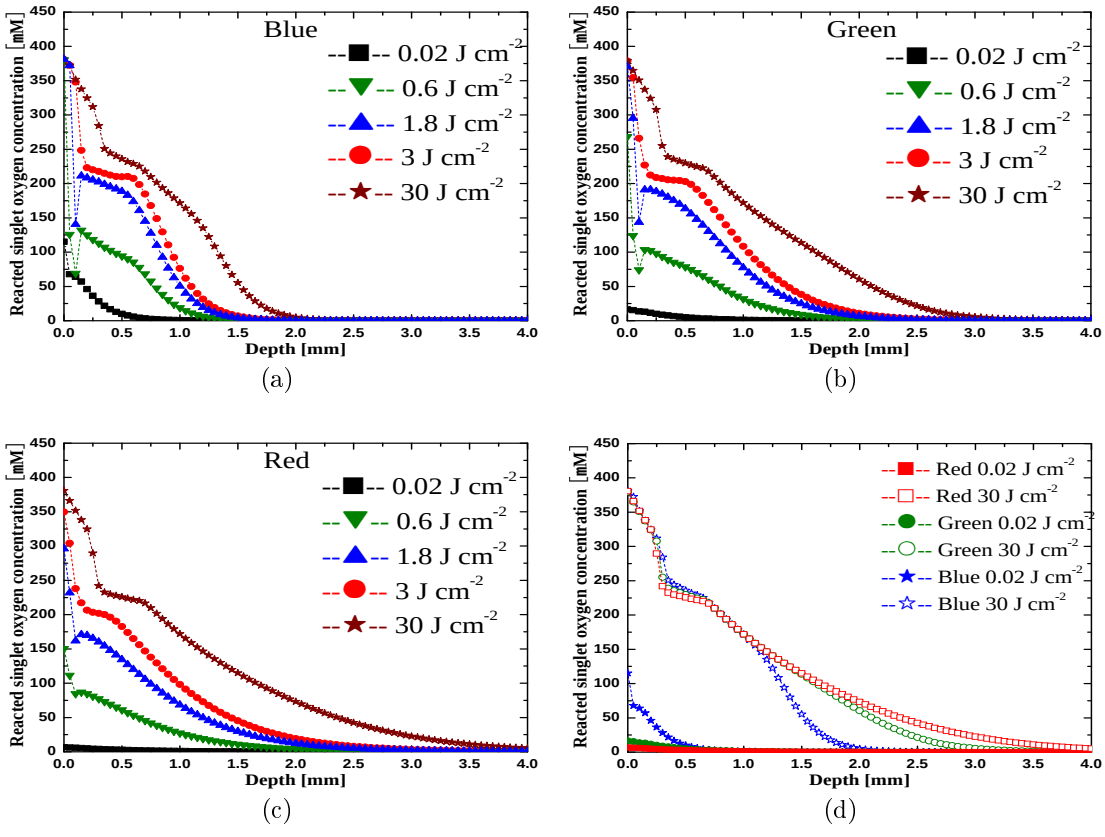

Figure 5.28: Depth-resolved distribution of reacted singlet oxygen.

The important of hypoxia and photobleaching are emphasized by additional calculations shown in figure 5.29. The hollow symbols are the results of the complete simulation (identical to figure 5.28(d)). The solid symbols are calculations of reacted singlet oxygen based on the initial photosensitizer concentration and the light fluence rate; photobleaching and hypoxia are not included. These calculations represent the predictions of an "explicit" dosimetry approach where the initial conditions are accurately determined and assumed to persist throughout the treatment. At sufficient depth, these nearly agree with those of the complete simulation, but closer to the surface, they can be in error by orders of magnitude. The third set of results in figure 5.29 represent simulations where photobleaching was "turned off" but where oxygen diffusion and consumption were included. Except for the most superficial layers, these simulations are in good agreement with the full simulations up to a depth of about 1 mm. This demonstrates that hypoxia is more important than photobleaching in determining the singlet oxygen dose in this region. At greater depths, where significant hypoxia is not induced, failure to include photobleaching results in an overestimate of the singlet oxygen dose. At even greater depths, where the fluence is insufficient to cause significant bleaching, all three calculations are in agreement.

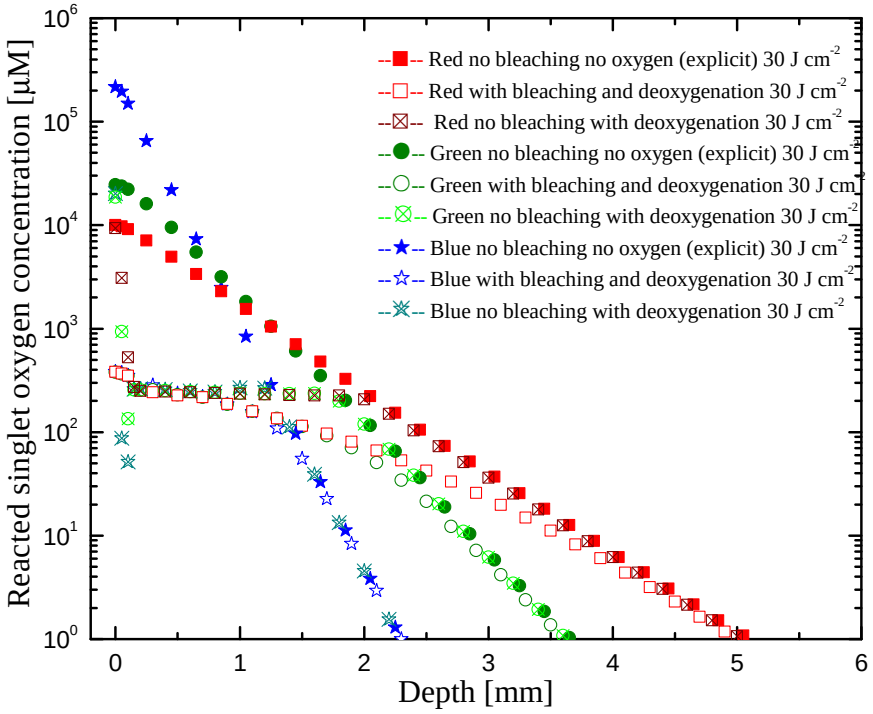

Figure 5.29: Comparison of reacted singlet oxygen concentration at three wavelengths for different cases. Note that, for clarity, the curves for the same case were plotted using the results at the same depths for all three wavelengths. The curves for different cases at the same wavelength were plotted using the results at different depths.

In order to match clinical photobleaching data from Cottrell *et al.* (2008), a PDT-induced reduction in blood perfusion was included. We recognize that there is no generally accepted independent evidence for this effect - measurements of blood flow during PDT have been inconclusive (Herman *et al.* 1999; Wang *et al.* 1997; Enejder *et al.* 2000; Becker *et al.* 2011; Tyrrell *et al.* 2011). Although this reduction in perfusion has a significant effect on observed fluorescence, the effect on singlet oxygen dose is relatively small as shown in figure 5.30 in which the results of figure 5.28(d) were replotted and compared to simulations where perfusion was unaltered.

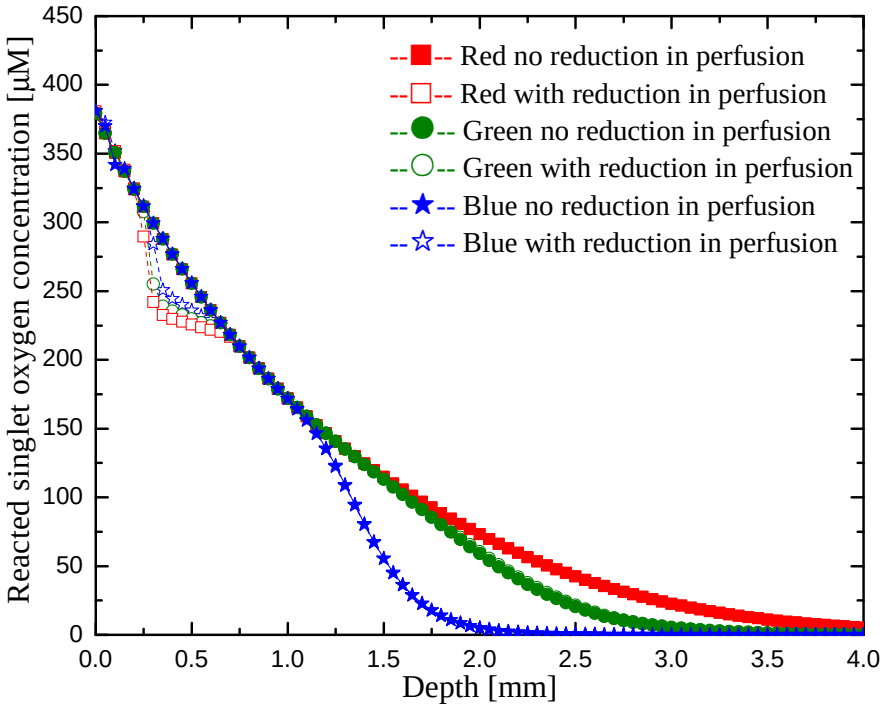

Figure 5.30: Comparison of reacted singlet oxygen concentration at three wavelengths for the cases with or without reduction in perfusion.

5.3.2 Dose metrics comparison

In an earlier paper, Liu *et al.* (2012) compared different PDT dose metrics and assessed their robustness under varied treatment conditions. Here we extend that analysis to incorporate treatment wavelength. In Liu *et al.* (2012), the compared metrics included CSOL (the total cumulative SOL metric), FFBM (the fractional fluorescence bleaching metric given by $\ln \frac{F_0}{F}$) and AFBM (the absolute fluorescence bleaching metric given by $F_0 - F$), where F is observed PpIX fluorescence and F_0 is its initial value. The comparison showed that the CSOL is the most robust, and that AFBM is more consistent than FFBM especially for varied PpIX concentration and distribution. However, because the absolute emission signals vary by at least one order of magnitude for different excitation wavelengths, only the FFBM is analyzed and compared with the CSOL in this study. The results are shown in figure 5.31 where the two dose metrics are plotted versus average reacted singlet oxygen dose in the dermis. As seen, the correlation between the CSOL and average reacted singlet oxygen dose in dermis is approximately linear, and is almost independent of the treatment wavelength. In contrast, the FFBM is less robust: the average singlet oxygen dose is about 50% higher for red light than blue light for the same observed reduction in PpIX fluorescence.

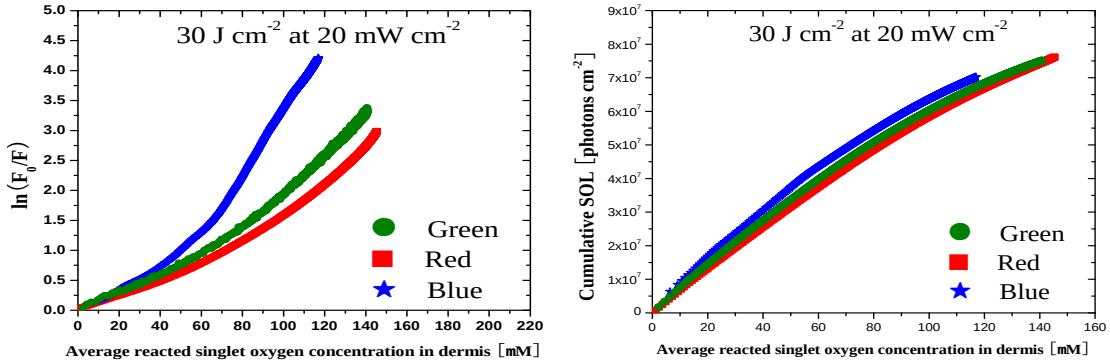

Figure 5.31: Comparison of the dose metrics for different wavelength. (a): FFBM and (b): CSOL.

Instead of the average singlet oxygen dose in the dermis, a more critical parameter might be the dose at a specific depth. In a more detailed analysis shown in figure 5.32, we examined the relationship between FFBM and CSOL and the dose at depths of 0, 0.2, 0.5, 1.0 and 2.0 mm. The horizontal lines in the figure indicate the radiant light exposure during progress of PDT treatment.

As noted in an earlier paper (Liu *et al.* 2012) the relationship of the dose metric to the actual $^1O_2$ dose can be complex, especially for depths less than 1 mm. To examine the effect of treatment wavelength on these relationships, the data for depths 0.2, 0.5 and 1 mm are replotted and shown in figure 5.33. Although hypoxia and photobleaching cause complicated features in these curves at depths 0.2 and 0.5 mm, the influence of treatment wavelength is surprisingly small. The results at 1 mm depth show that the curve for blue light diverges from those for red and green light due to the limited penetration at 405 nm. This is even more prominent at 2 mm depth.

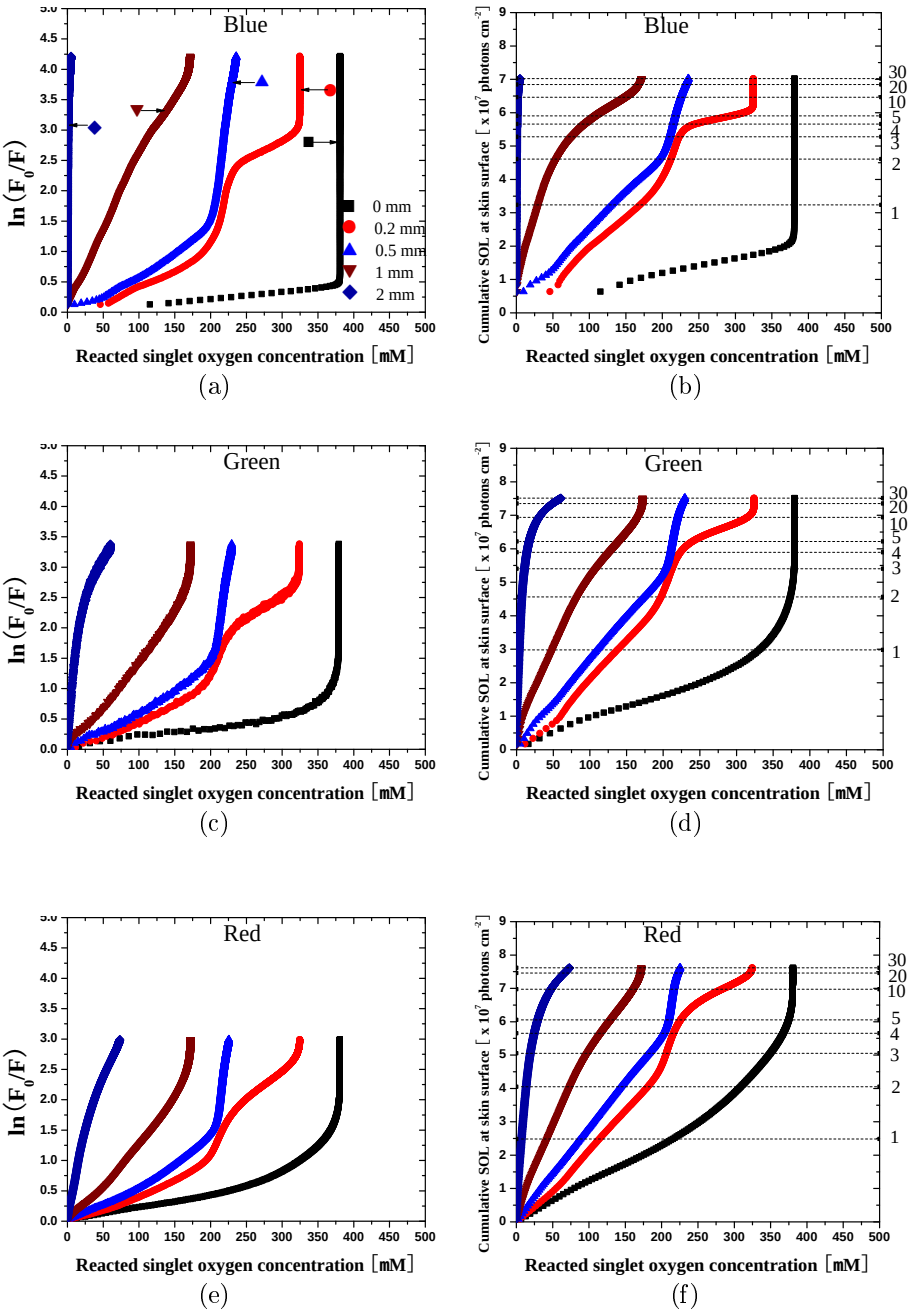

Figure 5.32: Correlation of FFBM (a, c, e) and CSOL (b, d, f) to the singlet oxygen dose in a 50 μm layer at depths of 0, 0.2, 0.5, 1 and 2 mm for different treatment wavelengths. Labels on the right hand coordinate of b, d, f are radiant exposure in J cm^{-2}. Labels in (a) are also applied in the same order to the curves in (b) - (f).

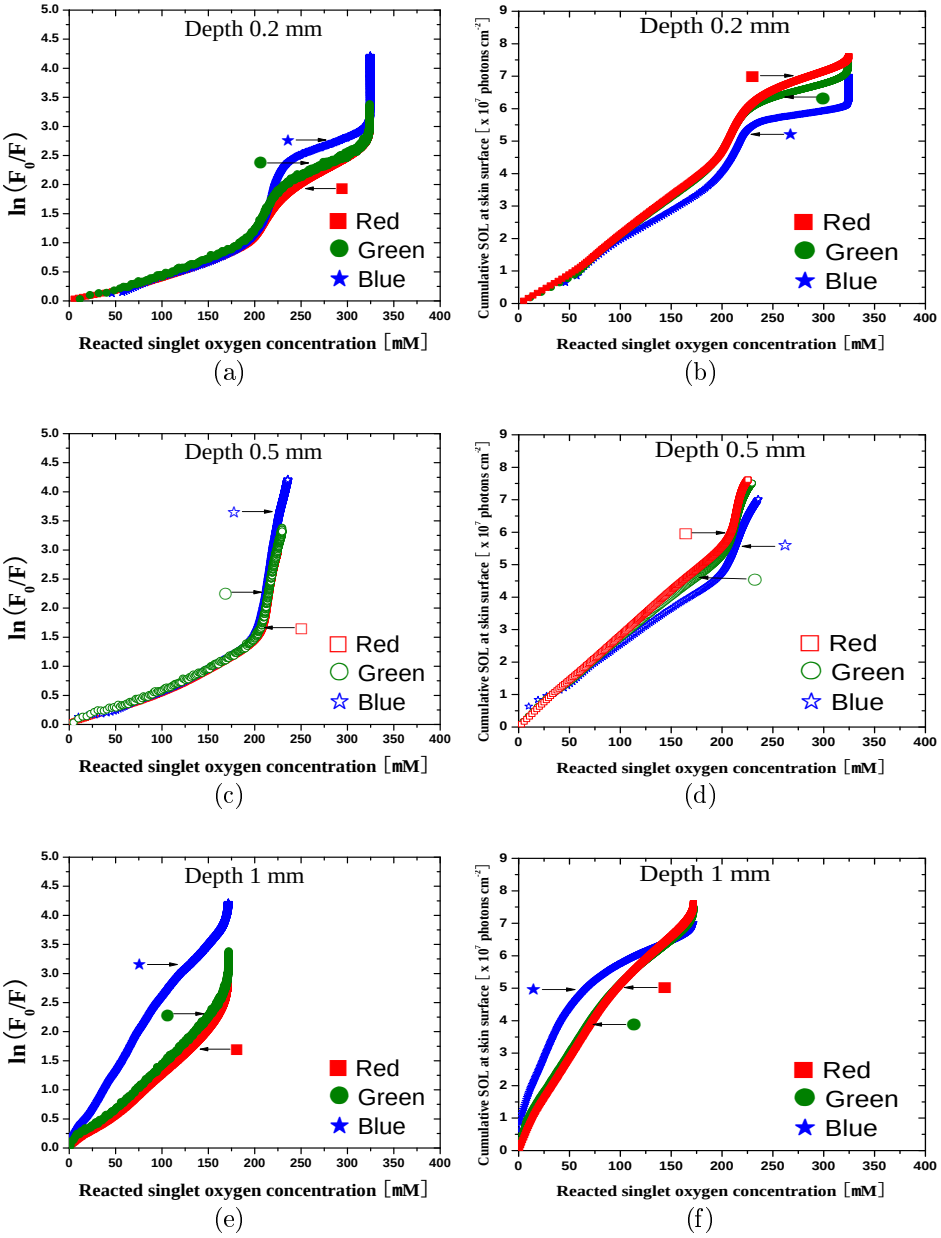

Figure 5.33: Correlation of FFBM and CSOL to the singlet oxygen dose at depths of 0.2, 0.5 and 1 mm for different wavelength.

5.4 Conclusion

The present work is part of a comprehensive investigation of PDT mechanisms and dosimetry using a dynamic model of ALA-PDT of normal human skin. The focus of this paper was on the influence of PDT treatment wavelength on the temporal and spatial distributions of PDT quantities and on different PDT dose metrics. In general, wavelength-dependent differences in time-resolved evolutions of PDT components in the epidermis and upper dermis can be observed only very early in the PDT treatment. After radiant exposure of about 3 J cm^{-2}, these distributions are almost independent of the treatment wavelength to a depth of about 1 mm.

Even though light penetration depth is about four times greater for red light than blue light, the influence of this variation on the distributions, especially for reacted singlet oxygen, was offset by sensitizer photobleaching and tissue oxygen depletion in the upper dermis. Different penetration depth led to different spatial distributions of the quantities only in the deeper tissue where no significant photobleaching and hypoxia occurred. Our simulations showed that tissue hypoxia plays a more important role than photobleaching for depth less than about 1 mm. Moreover, the distributions of reacted singlet oxygen are not very sensitive to the hypothesized reduction in oxygen perfusion, and these conclusions are probably valid under a wide range of conditions.

We also compared the wavelength sensitivity of two noninvasive PDT dose metrics: cumulative singlet oxygen luminescence (CSOL) and fractional fluorescence bleaching (FFBM). The relationship between CSOL and singlet oxygen dose (either average dose in the dermis or dose at specific depths) was less dependent on wavelength than that for FFBM. At depths above 1 mm, even for FFBM, the variation with wavelength was small enough to suggest that these methods could be applied across the full spectrum of ALA-PDT treatment wavelengths.

Acknowledgements

This research has been supported by the Canadian Cancer Society Research Institute.

Bibliography

Becker, T. L., Paquette, A. D., Keymel, K. R., Henderson, B. W., and Sunar, U. (2011). Monitoring blood flow responses during topical ALA-PDT. *Biomed. opt. Express*, **2**, 123–30.

Cottrell, W. J., Paquette, A. D., Keymel, K. R., Foster, T. H., and Oseroff, A. R. (2008). Irradiance-dependent photobleaching and pain in δ-aminolevulinic acid-photodynamic therapy of superficial basal cell carcinomas. *Clin. Cancer Res.*, **14**, 4475–4483.

Enejder, A. M. K., af Klinteberg, C., Wang, I., Andersson-Engels, S., Bendsoe, N., Svanberg, S., and Svanberg, K. (2000). Blood perfusion studies on basal cell carcinomas in conjunction with photodynamic therapy and cryotherapy employing laser-Doppler perfusion imaging. *Acta Derm. Venereol.*, **80**, 19–23.

Fritsch, C., Stege, H., Saalmann, G., Goerz, G., Ruzicka, T., and Krutmann, J. (1997). Green light is effective and less painful than red light in photodynamic therapy of facial solar keratoses. *Photodermatol. Photoimmuno. Photomed.*, **13**, 181–5.

Georgakoudi, I. and Foster, H. T. (1998). Singlet oxygen- versus nonsinglet oxygen-mediated mechanisms of sensitizer photobleaching and their effects on photodynamic dosimetry. *Photochem. Photobiol.*, **67**, 612–625.

Gold, M. H. (2007). Acne Vulgaris: lasers, light sources and photodynamic therapy - an update 2007. *Expert Rev. Anti Infect. Ther.*, **5**, 1059–69.

Gold, M. H. and Goldman, M. P. (2004). 5-Aminolevulinic acid photodynamic therapy: where we have been and where we are going. *Dermatol. Surg.*, **30**, 1077–84.

Herman, M. A., Fromm, D., and Kessel, D. (1999). Tumor blood-flow changes following protoporphyrin IX-based photodynamic therapy in mice and humans. *J. Photochem. Photobiol. B: Biol.*, **52**, 99–104.

Jarvi, M. T., Niedre, M. J., Patterson, M. S., and Wilson, B. C. (2006). Singlet oxygen luminescence dosimetry (SOLD) for photodynamic therapy: current status, challenges and future prospects. *Photochem. Photobiol.*, **82**, 1198–210.

Josefsen, L. B. and Boyle, R. W. (2008). Photodynamic therapy and the development of metal-based photosensitisers. *Met Based Drugs.*, **v.2008**.

Keene, J. P., Kessel, D., Land, E. J., Redmond, R. W., and Truscott, T. G. (1986). Direct detection of singlet oxygen sensitized by Haematoporphyrin and related compounds. *Photochem. and Photobiol.*, **43**, 117–20.

Liu, B., Farrell, T. J., Patterson, M. S., Jarvi, M. T., and Wilson, B. C. (2009). A Monte Carlo model of detected singlet oxygen luminescence and photosensitizer fluorescence during ALA-PDT of skin. In *Proc. of SPIE*, volume 7380, pages 73806W 1–11.

Liu, B., Farrell, T. J., and Patterson, M. S. (2010). A dynamic model for ALA-PDT of skin: simulation of temporal and spatial distributions of ground-state oxygen, photosensitizer and singlet oxygen. *Phys. Med. Biol.*, **55**, 5913–32.

Liu, B., Farrell, T. J., and Patterson, M. S. (2012). Comparison of noninvasive photodynamic therapy dosimetry methods using a dynamic model of ALA-PDT of human skin. *Phys. Med. Biol.*, **57**, 825–41.

Morton, C. A., Whitehurst, C., Moore, J. V., and Mackie, R. M. (2000). Comparison of red and green light in the treatment of bowen's disease by photodynamic therapy. *Br. J. Dermatol.*, **143**, 767–72.

Nielsen, K. P., Juzeniene, A., Juzenas, P., Stamnes, K., Stamnes, J. J., and Moan, J. (2005). Choice of optimal wavelength for PDT: the significance of oxygen depletion. *Photochem. Photobiol.*, **81**, 1190–4.

Salomatina, E., Jiang, B., Novak, J., and Yaroslavsky, A. N. (2006). Optical properties of normal and cancerous human skin in the visible and near-infrared spectral range. *J. Biomed. Opt.*, **11**.

Tyrrell, J., Thorn, C., Shore, A., Campbell, S., and Curnow, A. (2011). Oxygen saturation and perfusion changes during dermatological methylaminolaevulinate photodynamic therapy. *Br. J. Dermatol.*, **165**, 1323–31.

Wang, I., Andersson-Engels, S., Nilsson, G. E., Wårdell, K., and Svanberg, K. (1997). Superficial blood flow following photodynamic therapy of malignant non-melanoma skin tumours measured by laser doppler perfusion imaging. *Br. J. Dermatol.*, **136**, 184–9.

Wang, K. K., Mitra, S., and Foster, T. H. (2007). A comprehensive mathematical model of microscopic dose deposition in photodynamic therapy. *Med. Phys.*, **34**, 282–93.

Chapter 6

Paper V-Singlet oxygen luminescence detection using a novel SNSPD detector

6.1 Introduction

Direct monitoring of singlet oxygen via its very weak near-infrared luminescence at 1270 nm has been attempted for decades to develop a direct PDT dose metric - singlet oxygen luminescence dosimetry (SOLD). Although singlet oxygen luminescence (SOL) signals have been detected *in vitro* and *in vivo* using photomultiplier tubes (PMT), the progress of SOLD development has been limited by the challenges in developing a highly efficient, compact and affordable SOL detector. Recently, the feasibility of detecting SOL with a novel superconducting nanowire single photon detector (SNSPD) has been demonstrated. This chapter will give a short review of the current PMT-based SOL detection system, and will introduce this new more efficient SNSPD system and show some preliminary results of SOL detection using SNSPD. The author participated in the experiments on the evaluation of the SNSPD system and analyzed the results shown in this chapter. This work was done in the collaboration with Dr. Robert Hadfield at Heriot-Watt University and Dr. Brian Wilson at the University of Toronto.

6.1.1 Singlet oxygen luminescence detection

The history of singlet oxygen luminescence dosimetry (SOLD) has been briefly introduced in chapter 1. Time-resolved measurement of SOL emission at 1270 nm is commonly used to derive lifetimes of $^1O_2$ and triplet state sensitizer in different environments.

As described by Patterson *et al.* (1990) and Niedre *et al.* (2002), the kinetics of the reactions for singlet excited-state sensitizer (S_1), triplet excited-state sensitizer (T_1) and singlet oxygen ($^1O_2$), without photobleaching of ground-state sensitizer (S_0) and depletion of ground-state oxygen ($^3O_2$), can be described by three coupled differential equations, as shown in equations (6.92), (6.93) and (6.94), where ϕ is the local excitation fluence rate [photon cm^{-2} s^{-1}], σ is the S_0 molecular absorption cross section [cm^{-2}], Φ_D is the $^1O_2$ quantum yield, Φ_T is the T_1 quantum yield, τ_S, τ_T and τ_D are the lifetimes of S_1, T_1 and $^1O_2$ respectively.

$$\frac{d[S_1]}{dt} = \phi\sigma[S_0] - \frac{1}{\tau_S}[S_1] , \tag{6.92}$$

$$\frac{d[T_1]}{dt} = \frac{\Phi_T}{\tau_S}[S_1] - \frac{1}{\tau_T}[T_1] , \tag{6.93}$$

$$\frac{d[^1O_2]}{dt} = \frac{\Phi_D}{\Phi_T\tau_T}[T_1] - \frac{1}{\tau_D}[^1O_2] . \tag{6.94}$$

Consider an excitation pulse much shorter than τ_T and τ_D, $\phi = N\delta(t)$, where N (photon cm^{-2}) is the number of photons incident on the sample at time $t = 0$. Assuming the lifetime of S_1 is also much shorter than τ_T (i.e. all the T_1 are generated "instantaneously"), the $^1O_2$ concentration at time t after this light pulse can be calculated via equation (6.95). Then, the SOL emission can be approximated as equation (6.96), and the cumulative SOL after one pulse is given by equation (6.97), where τ_R is the $^1O_2$ radiative lifetime in the solvent. Note that equation (6.95) can be used to approximate and fit to the time-resolved SOL decay curve, and the cumulative SOL signal needs to be normalized by τ_D when comparing the amounts of $^1O_2$ generated in different environments.

$$[^1O_2](t) = N\sigma[S_0]\Phi_D\frac{\tau_D}{\tau_T - \tau_D}\left(e^{(-t/\tau_T)} - e^{(-t/\tau_D)}\right) , \tag{6.95}$$

$$L_{1270}(t) = \frac{[^1O_2](t)}{\tau_R} , \tag{6.96}$$

$$\int L_{1270}(t)dt = \frac{N\sigma[S_0]\Phi_D\tau_D}{\tau_R} . \tag{6.97}$$

6.1.2 A review of current SOL detection system-PMT detector

As seen in equation (6.97), the SOL signal decreases with the singlet oxygen lifetime (τ_D). τ_D decreases at least an order of magnitude from a simple aqueous solution sample to a biological environment, which makes *in vivo* SOL measurement very difficult. The emission probability of SOL is extremely low, approximately 10^{-8}. Also, ground-state oxygen depletion during *in vivo* PDT can limit the production of

singlet oxygen and further reduce the SOL signal. Therefore, the detection of the SOL in a biological environment requires a very sensitive detector. This detector should be highly efficient at 1270 nm with low dark count rate. The successful detection of SOL in biological systems was reported for the first time by Niedre *et al* and Hirano *et al* in 2002. Both groups used near-infrared photomultiplier tubes (PMT) (R5509-42, Hamamatsu Corp, NJ, USA) operating in time-resolved single photon-counting mode. The rise time of this PMT detector is about 3 ns (Jarvi *et al.* 2006). The quantum efficiency (η_{qe}) at 1270 nm of this generation PMT detector was about 0.9% and the dark count rate was about 2×10^4 counts per second. With SNR=1, the minimum detectable singal is 2.8×10^{-15} W with a 1 second integration on a continuous source (Jarvi *et al.* 2006).

Figure 6.34 shows the schematic of the SOL detection system (left figure) and a photograph of the system (right figure) in Dr. Wilson's group at the University of Toronto. The figures were adapted from Jarvi *et al.* (2006). The setup was slightly modified from the original system used by Niedre. Note that, in this system, a laser scanning imaging system is integrated including a pair of galvanometer-mounted scan mirrors, a CCD camera and the PMT detector (Jarvi *et al.* 2006). A newer generation of this PMT (H9170-45, Hamamatsu, Bridgewater, NJ) currently used in Dr. Wilson's lab is thermoelectrically-cooled and operated at -900 V (Jarvi *et al.* 2011). The minimum quantum efficiency is claimed at about 4.8% by the manufacturer, and the rise time is improved to 0.9 ns. The effective area of PMT is reduced from 3 ×8 mm to a diameter of 1.6 mm, hence the dark count rate per unit area is increased.

The laser source is another main component for SOL detection. In order to use equation (6.95) to approximate the time-resolved SOL curve the laser pulse must be much shorter than τ_T and τ_D. Normally, τ_T is greater than τ_D, and the lower limit of τ_D can be estimated to be about 30 ns (Niedre *et al.* 2002). Hence a laser pulse of few nanoseconds is required. An appropriate average output power of 10-200 mW with a pulse repetition rate about 10 kHz is ideal for PDT treatment and time-resolved SOL measurements. Among currently available laser sources, a Q-switched pulsed laser was chosen. Unfortunately, this type of laser source is not available in red wavelength and is not optimal for photosensitizers with maximum absorption in the red or near infrared.

6.1.3 A novel SOL detection system: SNSPD detector

Photon detection using a superconducting device was first demonstrated about a decade ago (Gol'tsman *et al.* 2001). Most of these detectors are made of niobium nitride (NbN) nanowire, so they are often known as superconducting nanowire single photon detector, (SNSPD). These detectors have wide spectral range from visible to midinfrared wavelengths with different quantum efficiency at different wavelength.

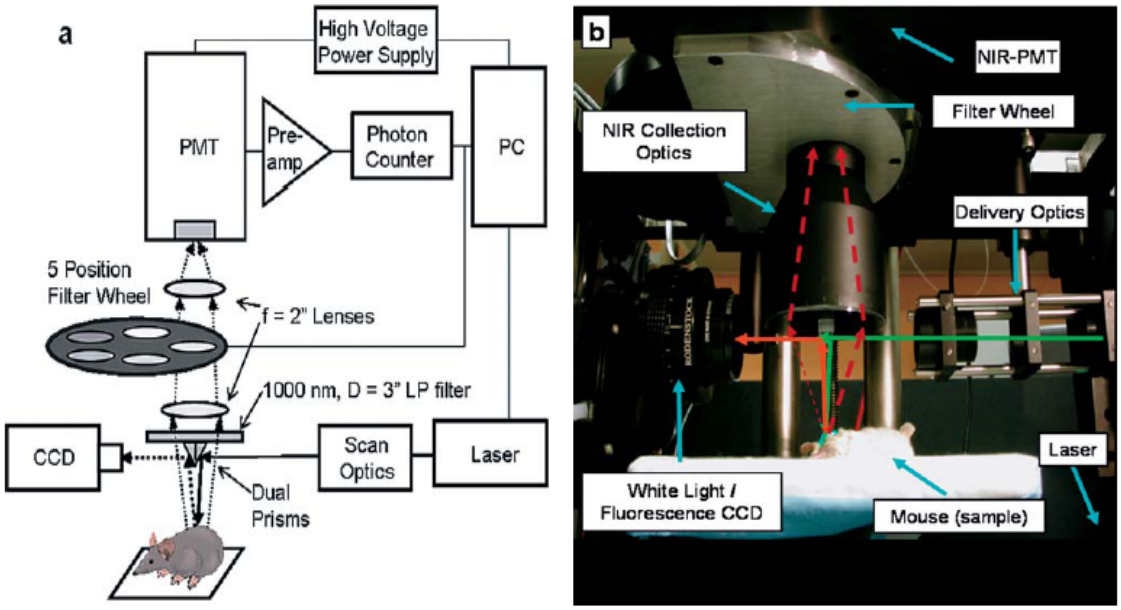

Figure 6.34: Schematic of the PMT system (left), and a photograph of the SOL detection system at University of Toronto (right). Adapted from Jarvi *et al.* (2006).

The typical dimensions of the nanowire are about 5 nm thick, 100 nm wide and hundreds of microns long. The SNSPD detector usually operates below the nanowire superconducting critical temperature which can be easily reached with current cooling technology based on liquid helium (Radebaugh 2004). The detailed description of the fundamental physical principles of the SNSPD detectors is beyond the scope of this thesis, and can be found in the literature (Natarajan *et al.* 2012). In brief, the NbN nanowire maintained below its superconducting critical temperature has biased direct current just below its critical current. Photons incident on the nanowire can break hundreds of Cooper pairs resulting in a localized non-superconducting region (or hotspot). This small resistive region will eventually form a resistive barrier across the nanowire and block the current flow, so that the bias current is shunted to the amplifier and detected. Finally, the hotspot cools and returns to the superconducting state again. The rise time of SNSPD is on the order of a couple hundred picoseconds (Stern and Farr 2007). The maximum count rates are in the range of 100 MHz to 1 GHz (Hadfield 2009). The SNSPD has been used in a variety of applications including quantum key distribution, time-of-flight ranging and high bit-rate ground-to-space communications (Takesue *et al.* 2007; Warburton *et al.* 2007; Robinson *et al.* 2006).

The system detection efficiency (η_{sde}) of the SNSPD system is determined by the

combination of the coupling efficiency (η_{coupling}), absorption efficiency ($\eta_{\text{absorption}}$) and registering probability ($\eta_{\text{registering}}$), as shown in equation (6.98). The detection efficiency (η_{de}) is given by equation (6.99). The coupling efficiency takes into account the loss of photons by absorption, scattering or reflection before entering the detector, and the absorption efficiency describes the probability of a photon being absorbed by the detector, which is determined by the detector material and geometry and wavelength of detected light. Not all photons absorbed by the detector will produce an output electrical signal, and this probability is described by the registering probability. With perfect optical coupling, the system detection efficiency is identical to the detector detection efficiency also referred to as quantum efficiency.

$$\eta_{\text{sde}} = \eta_{\text{coupling}} \times \eta_{\text{absorption}} \times \eta_{\text{registering}} , \tag{6.98}$$

$$\eta_{\text{de}} = \eta_{\text{absorption}} \times \eta_{\text{registering}} . \tag{6.99}$$

The SNSPD used in the present study consists of a single NbTiN nanowire covering a circular area with 10 μm diameter on a 225 nm SiO_2 layer that is on the top of a Si substrate. The sensitive wavelength range is from 830 to 1700 nm. The quantum efficiency of this detector was measured at 23.2% at 1310 nm wavelength with 1 kHz dark count rate (Tanner *et al.* 2010). This quantum efficiency is significantly higher than that of the current PMT (about 4%) and the dark count rate is 20 times lower.

6.2 Materials and methods

Figure 6.35 shows a schematic diagram of the optical excitation and SNSPD detection system at Heriot-Watt University. The light source was a diode-pumped, Q-switched, frequency-doubled Nd:YLF laser (QG-523-500; Crystalaser Inc., Reno, NV), emitting green light at 523 nm. The pulse width was about 10 ns, and the laser was operated at about 14 kHz. A narrow bandpass filter centered at 523 nm (10 nm bandpass, Thorlabs) was used in front of the laser to filter out any residual light at other wavelengths.

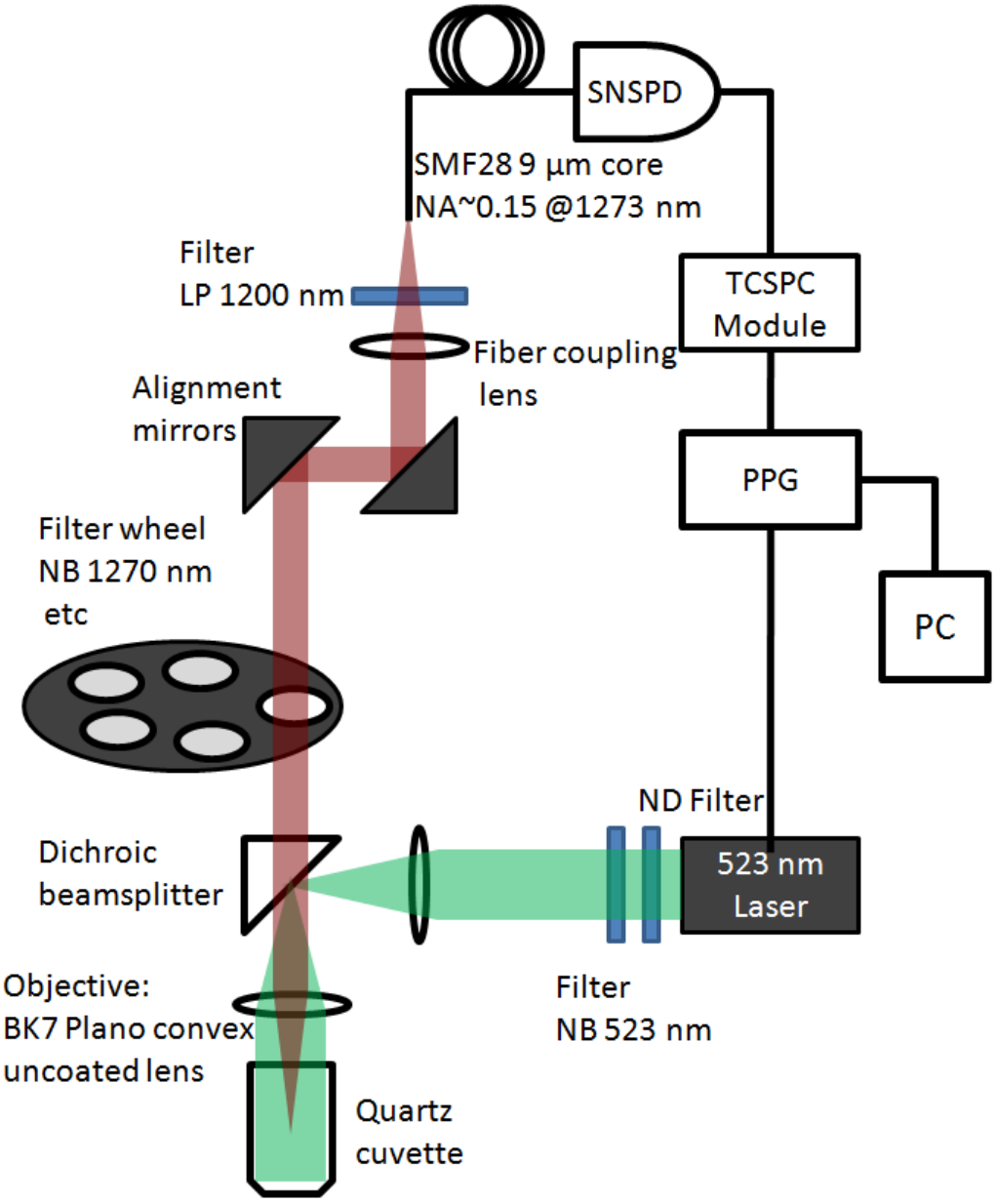

Figure 6.35: Schematic of the superconducting nanowire singlet photon detector system setup.

A couple of uncoated objective lenses combined with a Dichroic beamsplitter (532 nm laser BrightLine® single-edge laser-flat dichroic beamsplitter, Semrock Inc., Rochester, NY) were used to produce a 1 cm diameter beam with about 50 mW power on the sample surface. The emitted near-IR light was collected using a Plano-Convex uncoated lens. On the collection pathway, a set of five narrow-band filters centered at 1212 (20 nm FWHM, OD3 blocking; Omega), 1240 nm (20 nm FWHM, OD3 blocking; Omega), 1272 nm (19 nm FWHM, OD3 blocking; Omega), 1304 nm (20 nm FWHM, OD3 blocking; Omega), and 1332 nm (18 nm FWHM, OD3 blocking; Omega) were mounted on a five-position filter wheel manually rotated. This set of filters was used in the study by Niedre *et al.* (2005). These filters are referred to as the 1210, 1240, 1270, 1300 and 1330 nm filters for simplicity.

In front of the SMF 28 fiber connected to the SNSPD detector, there were one fiber coupling lens (effective focal length 18.4 mm, Numerical Aperture 0.15, C280TME-C, Thorlabs) to focus photons into the fiber and one 1200 nm longpass filter to filter all background light at lower wavelengths.

Photosensitizer Rose Bengal (RB) was prepared in aqueous solution at concentrations 25, 50, 100 and 250 μg/ml, and held in quart cuvettes with dimensions $1 \times 1 \times 4$ cm. During one rotation of the filter wheel, each sample was irradiated for 3 minutes for each narrow-band filter, and this was repeated for three rotations. There was one three-minute background collection between two rotations. To verify the SOL signal, the singlet oxygen quencher sodium azide (NaN_3) was added to the 250 μg/ml sample following the 1270 nm measurement, and then measurements were repeated for all wavelengths. Figure 6.36 is a photograph of the final setup of the SNSPD system.

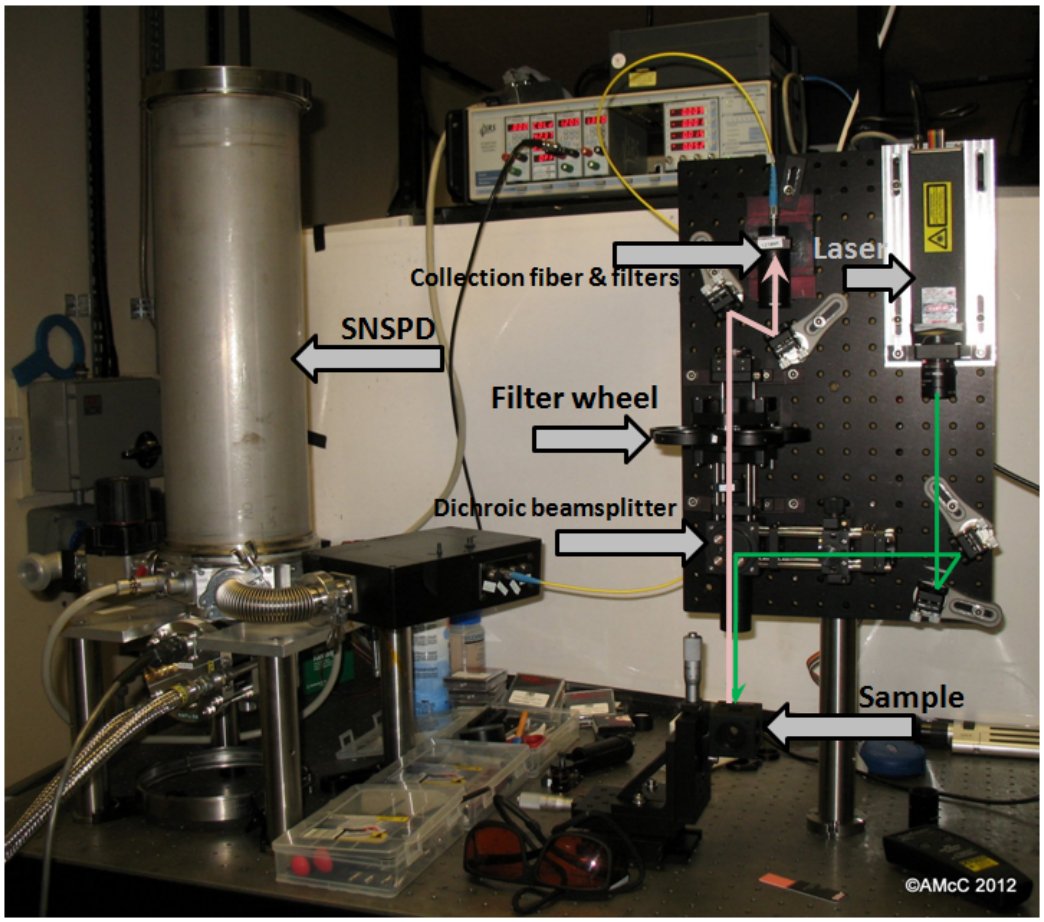

Figure 6.36: Photograph of the superconducting nanowire singlet photon detector system setup.

6.3 Results

In this section, some preliminary results are presented to demonstrate the detection of singlet oxygen luminescence emission at 1270 nm using this novel SNSPD detector. The original data were acquired with time bins of width 5.12×10^{-4} μs, and these have been grouped into bins 0.256 μs wide. The dark count histogram collected following each measurement was subtracted from the raw data. These steps were applied for all the following analyses.

Figure 6.37(a) shows the time-resolved signal detected from 250 μg/ml Rose Bengal (RB) in aqueous solution. The first sharp peak of the solid black line is the fluorescence tail of the RB. The second peak of this line rising from about 2 μs and spreading to about 14 μs is expected to be the SOL peak, and this is confirmed by the red dashed line under the black line. The red line is the result of repeated measurement using the same RB sample with the singlet oxygen quencher sodium azide (NaN_3) added. The disappearance of the second broad $^1O_2$ peak can be clearly seen. Figure 6.37(b) is the time integration of the time-resolved curves shown in 6.37(a) and the curves at the other four wavelengths. The curves were integrated from 2.3 μs where the fluorescence is negligible. These detected emission spectra show a clear peak at 1270 nm that is eliminated in the presence of NaN_3.

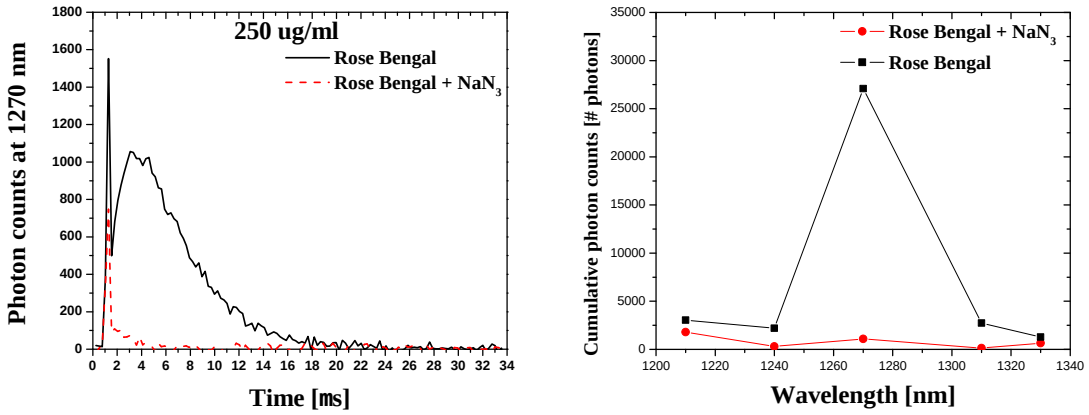

(a) (b)

Figure 6.37: Demonstration of the $^1O_2$ luminescence at 1270 nm for 250 μg/ml Rose Bengal in aqueous solution. (a): Time-resolved measurements with and without quencher NaN_3. (b): Time-integrated spectra (> 2.3 μs) with and without NaN_3.

Under well oxygenated conditions, the total SOL signal is expected to be proportional to sensitizer concentration. This relationship is examined for four different RB

solution samples with concentrations 25, 50, 100 and 250 μg/ml. Figure 6.38 shows detected cumulative SOL signals versus RB concentrations. An approximate linear relationship can be observed up to 100 μg/ml concentration, and the best linear fit to these three points can be made with an adjusted R^2 of 0.99. The signal then saturates at the highest concentration, which may be due to oxygen depletion and/or absorption of excitation light.

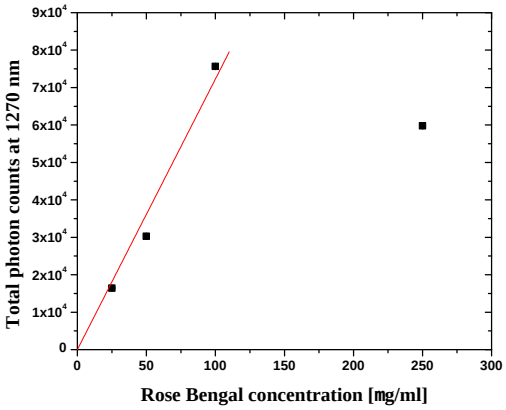

Figure 6.38: Time-integrated SOL signal at various RB concentrations. Adjusted R^2 of the best linear fit to the first three points was 0.99.

Figure 6.39 shows the measured time-resolved SOL data denoted as black solid squares with error bars for RB solutions of 25, 50, 100 and 250 μg/ml. Equation (6.95) was used to fit the time curves separately using the Levenberg-Marquardt algorithm in commercial software OriginPro 8 (OriginLab Corp., Northampton, MA). The fitted curves are red solid lines. Three free parameters in the fitting process were $A = N\sigma [S_0] \Phi_D$, τ_T and τ_D. The values for τ_T and τ_D obtained from the four best fits are listed in table 6.13. Note that τ_D and τ_T are denoted as the lifetimes of singlet oxygen and triplet state of sensitizer respectively but they cannot be distinguished from the fitting results alone due to the invariance of the fits when interchanging these two parameters in equation (6.95). The mean values of the derived τ_T and τ_D are 2.5±0.3 and 3.3±0.3 μs, respectively, which are in good agreement with the published values 2.4±0.3 and 3.0±0.3 μs (Niedre *et al.* 2002).

Table 6.13: Lifetimes derived from the best fits to the time-resolved SOL curves.

Concentration (μg/ml)	Lifetimes (μs)	
	τ_T	τ_D
25	2.5±0.6	3.2±0.7
50	2.2±0.2	3.8±0.3
100	2.5±0.3	3.4±0.3
250	2.9±0.8	2.7±0.8

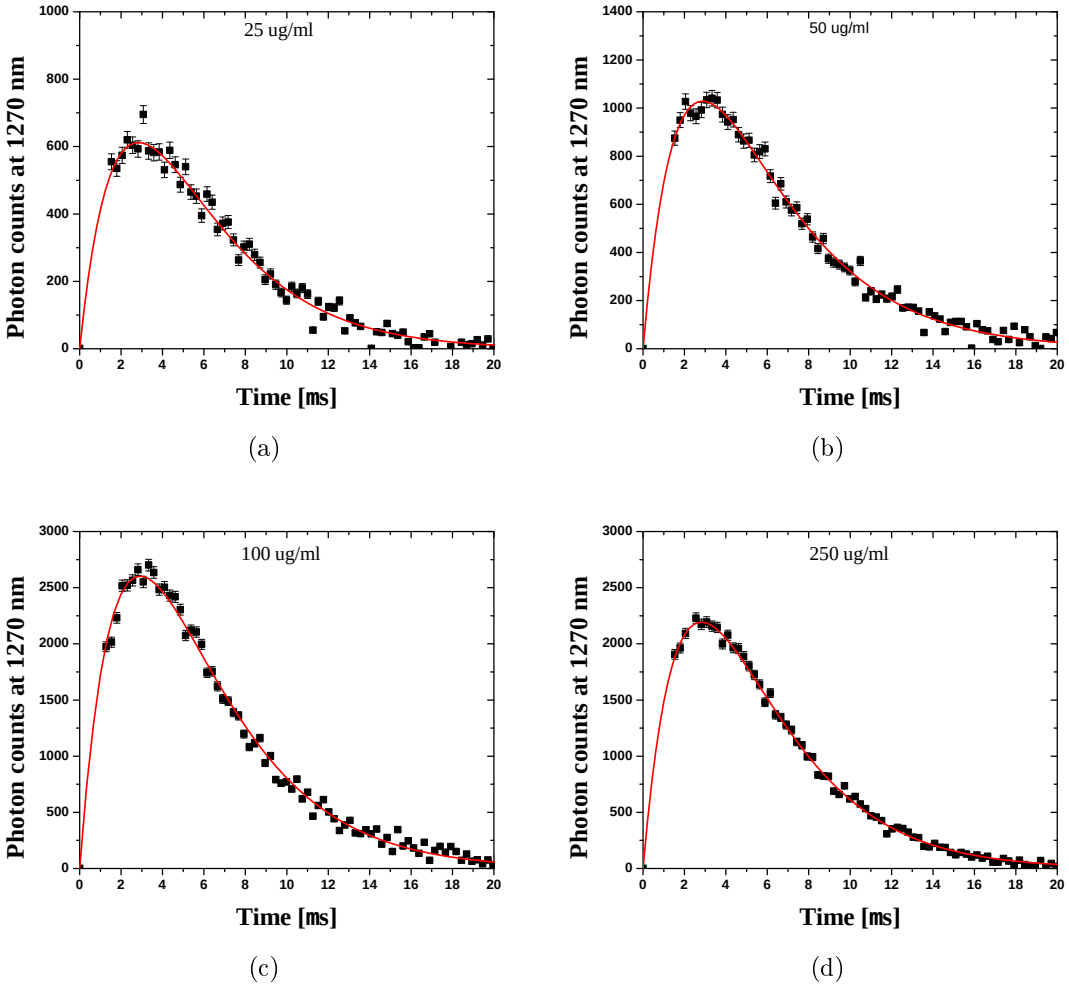

Figure 6.39: Time-resolved SOL curves with the best fits.

Photobleaching of sensitizer RB was verified by examining the reduction of SOL signals during three sets of measurements on the same 50 μg/ml sample. Figure 6.40(a) shows the three time-resolved SOL curves for all measurements, and figure 6.40(b) shows the time-integral of those three curves plotted versus overall irradiation time. Given that the SOL signal should be proportional to RB concentration in these solutions and there were about 15 minutes (3 minutes/filter $\times$ 5 filters) light exposure on the sample for one set of measurements with the five filters, it is reasonable to expect that RB can be bleached during one set of measurements, so the reduction of the SOL peak should be expected for the repeated three sets of measurements. This expectation is confirmed by the results shown in figure 6.40.

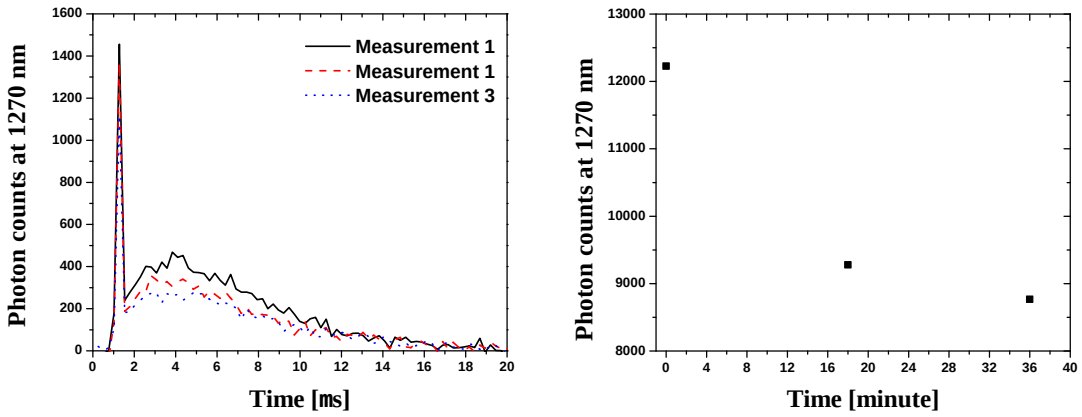

(a) (b)

Figure 6.40: Reduction of SOL due to photobleaching of RB.(a): time-resolved $^1O_2$ luminescence emission collected from 50 μg/ml RB in H_2O at three different time; (b): time-integrated (>2.3 μs) SOL in (a).

6.4 Conclusion and future work

A novel superconducting nanowire single photon detector was evaluated for singlet oxygen luminescence detection. This SNSPD with greater quantum efficiency than the current PMT detector is capable of detecting SOL from photosensitizer Rose Bengal in simple aqueous environment, and the detected signal is identified as the SOL signal using singlet oxygen quencher NaN_3. Even though these preliminary experiments were aimed to just demonstrate the feasibility of this detector, the best fits to the time-resolved SOL curves produced lifetime values of singlet oxygen and triplet-state

sensitizer comparable to the values in the literature. A series of more comprehensive experiments under more restricted conditions from *in vitro* environments to *in vivo* tissue will be conducted using this SNSPD detection system. Some preliminary results have recently been achieved with Rose Bengal in more biological-like environments such as solutions with protein Bovine serum albumin (BSA). The effective area of current generation of SNSPD is relatively small compared to other detectors such as PMT, which makes it challenging to focus detected photons accurately on to the active area. Although a detection fiber can be well coupled to the detector at room temperature, the coupling is very likely altered during the cooling process, which may lead to decreased detection efficiency. This can become a major concern for *in vivo* SOL detection from a big volume target or a fiber-based SNSPD system used in clinical PDT.

Bibliography

Gol'tsman, G. N., Okunev, O., Chulkova, G., Lipatov, A., Semenov, A., Smirnov, K., Voronov, B., Dzardanov, A., Williams, C., and Sobolewski, R. (2001). Picosecond superconducting single-photon optical detector. *Appl. Phys. Lett.*, **79**, 705–7.

Hadfield, R. H. (2009). Single-photon detectors for optical quantum information applications. *Nat. Photonics*, **3**, 696–705.

Jarvi, M. T., Niedre, M. J., Patterson, M. S., and Wilson, B. C. (2006). Singlet oxygen luminescence dosimetry (SOLD) for photodynamic therapy: current status, challenges and future prospects. *Photochem. Photobiol.*, **82**, 1198–210.

Jarvi, M. T., Niedre, M. J., Patterson, M. S., and Wilson, B. C. (2011). The influence of oxygen depletion and photosensitizer triplet-state dynamics during photodynamic therapy on accurate singlet oxygen luminescence monitoring and analysis of treatment dose response. *Photochem. Photobiol.*, **87**, 223–34.

Natarajan, C. M., Tanner, M. G., and Hadfield, R. H. (2012). Superconducting nanowire single-photon detectors: physics and applications. *Supercond. Sci. Tech.*, **25**, 063001.

Niedre, M., Patterson, M. S., and Wilson, B. C. (2002). Direct near-infrared luminescence detection of singlet oxygen generated by photodynamic therapyin cells *in vitro* and tissues *in vivo*. *Photochem. Photobiol*, **75**, 382–91.

Niedre, M. J., Yu, C. S., Patterson, M. S., and Wilson, B. C. (2005). Singlet oxygen luminescence as an *in vivo* photodynamic therapy dose metric: validation in normal mouse skin with topical amino-levulinic acid. *Br. J. Cancer*, **92**, 298–304.

Patterson, M. S., Madsen, S. J., and Wilson, B. C. (1990). Experimental tests of singlet oxygen luminescence monitoring *in vivo* during photodynamic therapy. *J. Photochem. Photobiol. B.*, **5**, 69–84.

Radebaugh, R. (2004). Refrigeration for superconductors. *P. IEEE.*, **92**, 1719–34.

Robinson, B. S., Kerman, A. J., Dauler, E. A., Barron, R. O., Caplan, D. O., Stevens, M. L., Carney, J. J., Hamilton, S. A., Yang, J. K. W., and Berggren, K. K. (2006). 781 mbit/s photon-counting optical communications using a superconducting nanowire detector. *Opt. Lett.*, **31**, 140–9.

Stern, J. A. and Farr, W. H. (2007). Fabrication and characterization of superconducting NbN nanowire single photon detectors. *IEEE Trans. Appl. Supercond.*, **17**, 306–9.

Takesue, H., Nam, S. W., Zhang, Q., Hadfield, R. H., Honjo, T., Tamaki, K., and Yamamoto, Y. (2007). Quantum key distribution over a 40-db channel loss using superconducting single-photon detectors. *Nat. Photonics*, **1**, 343–8.

Tanner, M. G., Natarajan, C. M., Pottapenjara, V. K., O'Connor, J. A., Warburton, R. J., Hadfield, R. H., Baek, B., Nam, S., Dorenbos, S. N., Ureña, E. B., Zijlstra, T., Klapwijk, T. M., and Zwiller, V. (2010). Enhanced telecom wavelength single-photon detection with nbtin superconducting nanowires on oxidized silicon. *Appl. Phys. Lett.*, **96**, 221109.

Warburton, R. E., McCarthy, A., Wallace, A. M., Hemandez-Marin, S., Hadfield, R. H., Nam, S. W., and Buller, G. S. (2007). Subcentimeter depth resolution using a single-photon counting time-of-flight laser ranging system at 1550 nm wavelength. *Opt. Lett.*, **32**, 2266–8.

Chapter 7

Conclusions and future work

7.1 Summary and conclusions

Photodynamic therapy (PDT) has inherent complicated reaction mechanisms, which makes the prediction of the PDT-induced therapeutic outcomes challenging. A one-dimensional model for ALA-PDT of normal human skin was developed incorporating the major photochemical reaction kinetics and spatial variations of fundamental PDT components such as light fluence rate and photosensitizer (PpIX) concentration. In addition, oxygen diffusion and perfusion from blood vessels are also taken into account. The PDT-induced vascular response was represented by the cumulative $^1O_2$-dependent reduction in oxygen perfusion rate in the model. The model and the choice of simulation parameters were evaluated using the simulated PpIX fluorescence compared with published clinical data for a wide range of irradiances. Time evolution of depth-dependent distributions of sensitizer, ground-state oxygen and singlet oxygen during PDT were obtained for three different treatment wavelengths (red, green and blue) and provided insights into the dynamic ALA-PDT process.

Furthermore, the relationships of three PDT dose metrics (FFBM, AFBM and CSOL) to the average reacted singlet oxygen 'dose' in dermis and to the 'dose' at specific depths were examined using the current model. The robustness of these metrics were compared for a wide range of variations in PDT treatment parameters such as treatment irradiance and wavelength, optical properties and initial PpIX concentration and distribution. The relationship of the CSOL metric to both average 'dose' and 'dose' at the chosen depths demonstrated the most robust performance among all the variations in treatment parameters when compared with the two fluorescence photobleaching metrics (implicit dosimetry). This indicates that the CSOL dose metric has great potential to be used as the 'gold standard' metric tool in clinical PDT.

From all the tests on the influence of photosensitizer photobleaching, oxygen diffusion and perfusion, and penetration depth of excitation light on the production of

reacted singlet oxygen, oxygen diffusion especially from air, and tissue hypoxia caused by both the consumption by PDT and the reduction in oxygen perfusion played more important roles than other factors.

The experimental assessment of SOL detection using a SNSPD system was successful. This more compact and efficient SNSPD system has great potential to accelerate research on SOL measurements *in vivo* and on direct PDT dosimetry.

7.2 Future work

The current dynamic model produced a set of comprehensive results for PDT under a variety of treatment conditions, and provided insights for researchers in the field for understanding PDT mechanism and PDT dosimetry. But there are still many improvements that can be made to advance the current model. For instance, this one-dimensional model with a simplified vasculature network can be potentially expanded to a three dimensional model with more complex and realistic blood vessel distributions. The index of refraction among layers can be set at different values, and optical properties of tissue can be allowed to vary to account for changing hemoglobin oxygen saturation during PDT. Reflectance can also be modeled to examine if it will be a useful tool to monitor oxygen saturation. Once more information about the physiological and photophysical parameters of *in-vivo* ALA-PDT is obtained from future experimental and clinical work, better quantitative calculations of the distributions of the PDT components could possibly be achieved.

Conclusive experimental results will be very useful to further evaluate and improve the model and verify the simulated relationships between PDT metrics and singlet oxygen 'dose'. Then, the potential of the CSOL or other metrics as a reliable tool to predict PDT-induced clinical response can possibly be realized. A pilot study of the singlet oxygen luminescence detection on 12 healthy human volunteers using the current photomultiplier tubes (PMT) detector system has been planned in Dr. Wilson's group at the University of Toronto. The author performed theoretical calculations for the prescribed radiant exposure for the experiments. The author designed and built a photosensitizer fluorescence detection system using a USB2000 spectrometer (Ocean Optics) and a photodiode to trigger the collection so that the fluorescence measurement can be synchronized with the SOL measurement. A labview control interface for the management of the fluorescence detection has been written, and tested by comparing the acquired spectra using this program with the commercial software OOIBase (Ocean Optics). Approval of the protocol by the institutional Research Ethics Boards (REB) is currently pending.

The hypothesis of PDT-induced reduction of oxygen perfusion or blood flow in the model needs to be supported by some conclusive experimental work on monitoring oxygen saturation or blood flow during *in vivo* PDT of human skin. The possible

means for this kind of measurement include laser Doppler imaging (Chen *et al.* 2003), Doppler optical coherence tomography (Gordon *et al.* 2004) or diffuse correlation spectroscopy (Yu *et al.* 2005; Becker *et al.* 2011).

The experiments conducted with the novel superconducting nanowire single photon detector (SNSPD) are currently at the preliminary stage. The results shown in chapter 6 demonstrate only the capability of this detector for SOL detection. More recently, some new progress has been made including detecting SOL from Rose Bengal solutions mixed with protein Bovine serum albumin (BSA), which is one more step toward SOL detection from *in vivo* tissue.

Additionally, another success recently achieved was the experimental validation of the feasibility of the SOL detection using a fiber-optics based SNSPD system. Figure 7.41 shows a schematic diagram of the first generation of the setups.

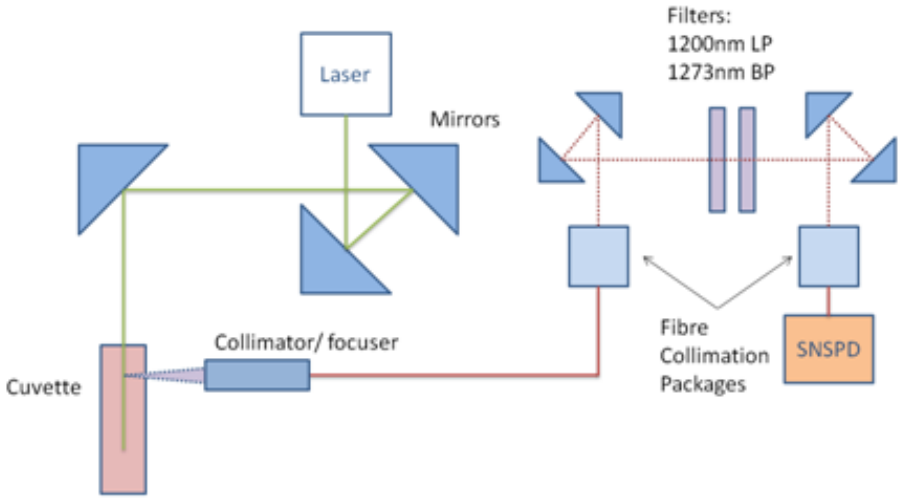

Figure 7.41: Fiber-based superconducting nanowire singlet photon detector system schematic diagram. Draw by Nathan Gemmell.

The feasibility of the SOL detection with this system has been successfully demonstrated in our recent experiments. Although the data collection time with the present configuration may be too long (1 hour) for practical clinical use, the concept has been demonstrated. Many improvements can be made in the future to reduce the collection time and increase the detection efficiency. These improvements may include more efficient collection of emission photons using multi-mode fibers or fiber bundles, more efficient fiber collimation, and larger detecting area of the nanowire sensor inside of the detector. There is reason to be optimistic that the much higher quantum efficiency with low dark count rate of this detector and the fiber-optics based system will lead to a practical clinical PDT dose metric tool.

Bibliography

Becker, T. L., Paquette, A. D., Keymel, K. R., Henderson, B. W., and Sunar, U. (2011). Monitoring blood flow responses during topical ALA-PDT. *Biomed. opt. Express*, **2**, 123–30.

Chen, B., Pogue, B. W., Goodwin, I. A., O'Hara, J. A., Wilmot, C. M., Hutchins, J. E., Hoopes, P. J., and Hasan, T. (2003). Blood flow dynamics after photodynamic therapy with verteporfin in the RIF-1 tumor. *Radiat. Res.*, **160**, 452–9.

Gordon, M., Yang, V., Yue, E., Lo, S., Wilson, B. C., and Vitkin, I. (2004). Doppler optical coherence tomography for monitoring the vascular effects of photodynamic therapy. In *Proc. of SPIE*, volume 5316, pages 147–54.

Yu, G., Durduran, T., Zhou, C., Wang, H. W., Putt, M. E., Saunders, H. M., Sehgal, C. M., Glatstein, E., Yodh, A. G., and Busch, T. M. (2005). Blood flow during and after photodynamic therapy provides early assessment of therapeutic efficacy. *Clin. Cancer Res.*, **11**, 3543–52.

Glossary

absorption efficiency
: the coupling efficiency due to absorption and it is normally determined by the detector material and geometry; 127

cooper pairs
: two bound electrons in a certain manner at low temperatures; 126

coupling efficiency
: the loss photons before reaching the detector due to absorption, scattering or reflection; 127

quantum efficiency
: intrinsic device detection efficiency defined as $\eta_{\text{de}} = \eta_{\text{absorption}} \times \eta_{\text{registering}}$; 127

registering probability
: the non-unity probability that the detector generates an output electrical signal after photon absorption; 127

system detection efficiency
: all contributions from coupling efficiency, absorption efficiency and registering probability.; 127